Title

A study of spin-orbit torques and deterministic field-free switching of perpendicular magnetization

Permalink

https://escholarship.org/uc/item/5c852366

Author

Razavi, Seyed Armin

Publication Date

2020

Peer reviewed|Thesis/dissertation

UNIVERSITY OF CALIFORNIA

Los Angeles

A study of spin-orbit torques and deterministic field-free switching of perpendicular
magnetization

A dissertation submitted in partial satisfaction

of the requirements for the degree of Doctor of Philosophy

in Electrical and Computer Engineering

by

Seyed Armin Razavi

2020

ABSTRACT OF THE DISSERTATION

A study of spin-orbit torques and deterministic field-free switching of perpendicular
magnetization

by

Seyed Armin Razavi

Doctor of Philosophy in Electrical and Computer Engineering

University of California, Los Angeles, 2020

Professor Kang Lung Wang, Chair

Spintronic devices provide an energy-efficient platform for implementing non-volatile memory and logic. In spintronic memory devices, the information is stored in the magnetization state of the free magnetic layer, and current, voltage or strain-induced mechanisms are used for switching the magnetization. Among the operation methods, current-induced spin-orbit torque (SOT) is a promising mechanism for magnetization switching with faster dynamics, higher endurance, and potentially higher energy efficiency compared to the conventional spin-transfer torque. For magnetic memory applications, perpendicular magnetic anisotropy is desirable since it enables high memory densities. However, for deterministic SOT switching of a perpendicular magnet, an external magnetic field collinear with the current is required, which hampers the applicability of SOT switching. Although there have been several prior effects aimed at solving this problem, but most involve structural asymmetries or additional layers that are not practical

for large wafer scale applications. Consequently, a practical realization of deterministic field-free SOT switching of perpendicular magnetization remains a challenge.

In this dissertation, we present two main methods for realizing deterministic field-free SOT switching for practical uses. First, we show that the external in-plane field can be replaced by a built-in exchange bias field using antiferromagnetic materials. We also show that certain antiferromagnets can create the SOTs themselves, serving as the layer providing both the exchange bias and SOTs. As the second approach, we use the concept of structural asymmetry reported previously, and modify the conventional SOT heterostructure by inserting a slightly asymmetric light-metal at the heavy-metal/ferromagnet interface. The broken structural symmetry enables the creation of current-induced out-of-plane effective magnetic fields, which break the symmetry between the up and down states for each current polarity and allow for deterministic SOT switching at zero external magnetic field. We also apply the asymmetry concept to a second material system with a minimal structural asymmetry, resulting in an enhanced magnetic uniformity across large wafer areas. We show that the latter approach for field-free SOT switching has almost all the characteristics of a practical solution that could be used in applications. We also present a better understanding of the deterministic switching process enabled by the structural asymmetry by examining its microscopic origins.

In the last part of this dissertation, we discuss several other interesting aspects of the antiferromagnet-based material system (IrMn/CoFeB/MgO) that we primarily developed for the field-free SOT switching. We show that this material system has several unique properties, including the simultaneous presence of Dzyaloshinskii-Moriya interaction, voltage-control of

magnetic anisotropy (VCMA), exchange bias field, and spin-orbit torques. We use this material system as a platform for studying magnetic skyrmions, where we can create/annihilate skyrmions using single voltage pulses without any external magnetic fields via the VCMA effect. Furthermore, we use spin-orbit torques to move the skyrmions in the same structure, providing a promising platform for skyrmion-based device applications.

The dissertation of Seyed Armin Razavi is approved.

Yaroslav Tserkovnyak

Yuanxun Ethan Wang

Chee Wei Wong

Kang Lung Wang, Committee Chair

University of California, Los Angeles

2020

To my parents, Sussan and Mehran.

Table of Contents

List of Figures

xiii

xx

Acknowledgements

I would like to first thank Prof. Kang Wang for his support and guidance throughout my graduate studies. He has established a great and diverse research environment at the Device Research Laboratory (DRL), where many interesting projects are pursued. I have learned a lot from him, not only about the technical details of my research, but also about the management of a research project. Prof. Wang has been at the very top for several decades, which speaks to the level of his dedication to research.

I also learned a lot from several amazing mentors at DRL. In the first two years I used to work closely with Mohammad Montazeri and Pedram Khalili, and I learned many basic concepts from them. Later, I started working with Guoqiang Yu on the antiferromagnet project (presented in Chapter 3). I also learned the basics of magnetotransport measurements from Di Wu. I benefitted from numerous fruitful discussions with Hao Wu and Qiming Shao on different projects (including the ones presented in Chapter 4). And in the last two years, Bingqian Dai helped me a lot with measurements on the projects presented in Chapter 5. Throughout these years Kin Wong has always supported us by fabricating the devices and I really appreciate it. I would also like to thank Aryan Navabi who has been a great friend. I asked a lot of questions from Aryan, on research, different exams, applying for jobs, and many other things! I am also grateful to all other DRLers, it has been a pleasure working with them all.

Vita

Seyed Armin Razavi

Education

2017-present   PhD Candidate, Electrical and Computer Engineering

University of California, Los Angeles, USA

2014-2017   Master's in Electrical Engineering

University of California, Los Angeles, USA

2009-2014   Bachelor's in Electrical Engineering

Sharif University of Technology, Tehran, Iran

Academic Employment

Graduate Student Researcher, Device Research Laboratory. Academic Advisor: Prof. Kang L.

Wang, Fall 2014 – present

Selected Publications

- **A. Razavi**, H. Wu, Q. Shao, C. Fang, B. Dai, K. Wong, X. Han, G. Yu, K. L. Wang, Deterministic Spin–Orbit Torque Switching by a Light-Metal Insertion. Nano Letters 20, 3703-3709 (2020).

- **A. Razavi**, H. Wu, B. Dai, H. He, D. Wu, K. Wong, Gu. Yu, K. L. Wang, Spin-orbit torques in structures with asymmetric dusting layers. Applied Physics Letters 117, 182403 (2020).

- **S. A. Razavi**, D. Wu, G. Yu, Y.-C. Lau, K. L. Wong, W. Zhu, C. He, Z. Zhang, J. M. D. Coey, P. Stamenov, P. Khalili Amiri, K. L. Wang, Joule Heating Effect on Field-Free Magnetization Switching by Spin-Orbit Torque in Exchange-Biased Systems. Physical Review Applied 7, 024023 (2017).

- D. Bhattacharya, **S. A. Razavi**, H. Wu, B. Dai, K. L. Wang, J. Atulasimha, Creation and annihilation of non-volatile fixed magnetic skyrmions using voltage control of magnetic anisotropy. Nature Electronics, (2020).

- H. Wu, J. Nance, **S. A. Razavi**, D. Lujan, B. Dai, Y. Liu, H. He, B. Cui, D. Wu, K. Wong, Chiral symmetry breaking for deterministic switching of perpendicular magnetization by spin-orbit torque. arXiv preprint arXiv:2004.13872 (2020).

1 INTRODUCTION

1.1 FROM CHARGE-BASED TRANSISTORS TO SPINTRONICS

Electronic devices and systems have changed the way we live in the past few decades, with applications ranging from communication systems to smarts phones, personal computers, servers, and data centers, to name a few categories. Electronics has also been the driving force behind the artificial intelligence systems, which is revolutionizing numerous aspects of our everyday life. At the heart of all these advances lie an electronic device called transistor, which was invented in December 1947 at Bell Labs (*1*), and on a yet more fundamental level, electrons lie at the heart of transistors. One of the distinctive features of electrons is that they are charged particles, and over centuries, we have learned how to control electron movement inside solid materials using electric and magnetic fields, which has made these particles very convenient for device applications (Figure 1.1). On the other hand, transistor technology has enjoyed an extraordinary exponential scaling over several decades, the so-called Moore's law, which has allowed for large-scale systems (*2, 3*). However, this exponential growth cannot continue forever because of physical limits, and today we are at a point where further transistor scaling is becoming extremely expensive and hard (*4*). The imminent slowdown of the Moore's law and the emergence of new computing paradigms has created a fantastic challenge for researchers and industry to come up with radically innovative ideas for keeping up the improvement of electronic/computing systems. Consequently, there have been a plethora of new device concepts recently, ranging from devices based on 2-dimensional materials to quantum computers. Among

these new concepts, *spintronics* holds a special place as one of the leading contenders for the development of novel logic/memory devices and systems.
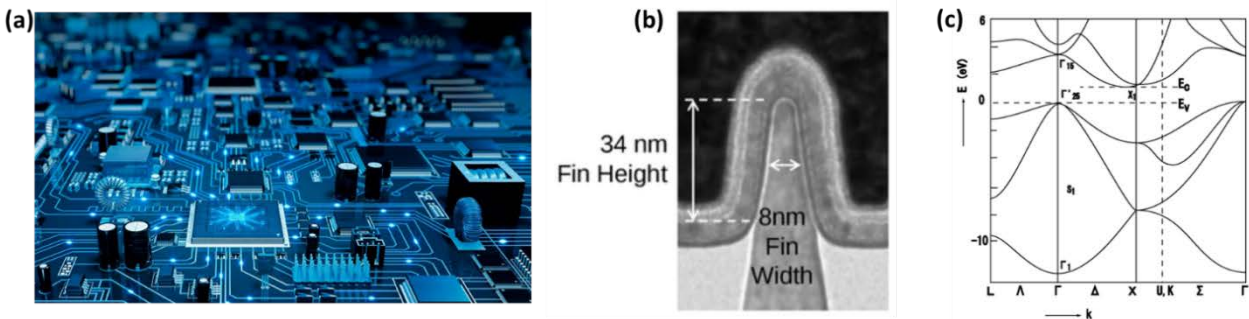
Figure 1.1. Breakdown of current electronic systems and devices. (a) An electronic chip consisting of various components (from GE Research website). (b) Intel's 22 nm node FinFET transistor. Transistors lie at the heart of current conventional electronics (taken from WikiChip's website, 22 nm lithography process). (c) Si band structure. Understanding the electron movement in semiconductors has been the most important fundamental driving force of the current electronic devices.

The main problem with today's transistors technology is that they have a high static power consumption (i.e., high power loss when they are not operating). The main reason for the static loss is the charge leakage which originates from the fact that transistors are charge-based devices. This problem is exacerbated as transistors are scaled to smaller dimensions because of an increased leakage. In MOSFET transistors, the electron flow between *source* and *drain* ports is controlled by a voltage applied to the *gate* port. Using the gate voltage, one can turn the source-drain current on/off. However, as transistors are scaled to few nm feature sizes, there is a significant deviation from this ideal picture (*4*). In specific, at scaled dimensions, there is an increased leakage through the thinner gate oxide and between source and drain, resulting in a large static power loss. The static charge leakage is especially a serious challenge for high-performance charge-based memory devices (static random access memory SRAM, and dynamic random access memory DRAM), making them volatile and in need of periodic refreshing (*5*). On

2

the other hand, and as a result of the advent of memory-centric computing paradigms, there is an ever-increasing demand for high-performance **non-volatile** embedded memories. Magnet-based memories, which use the spin-state of electrons to store information, are non-volatile and a natural candidate for an embedded high-performance memory. It should be noted that although magnetic hard disk drives have been used for several decades, but they are not random-access memories and have a slow operation speed. However, using the electron's spin degree of freedom, one can realize a high-performance magnetic memory.

In conventional electronics, we take advantage of the electrons charge degree of freedom. However, electrons are much richer particles, and charge is not their only intrinsic property. An electron also has an intrinsic *spin*, which has been historically studied much less compared to its charge, since it could only be understood after the development of quantum mechanics (*6*). By neglecting the role of electron spins in electronic devices, we have been missing on many potentially useful functionalities. This is where the concept of spintronics appear; it basically tries to acknowledge and use both the spin and the charge of electrons for new device applications and functionalities (*7*). One immediate application of spintronics is in the development of magnetic memories, where the information is encoded in the magnetic order, and the effective magnetic field from the electrons spins is used to switch the magnetization. It should be noted that this configuration is different from hard disk drives which rely on the magnetic field from wire loops inside the writing head and thus require moveable parts. In a typical spintronics memory, magnets with uniaxial anisotropy are used, meaning that the bistable magnetization directions will be along an axis and pointing in opposite directions (see Figure 1.2). It is easy to design an energy barrier of around ~ 40 k_BT between the bistable states in these devices, where

k$_B$ and T are the Boltzmann's constant and temperature. This in turn corresponds to an escape rate of around ten years at room temperature, which means that these magnetic memories can be virtually non-volatile. Another important advantage is that in these spintronic memories, there is no leakage and the standby power is zero.
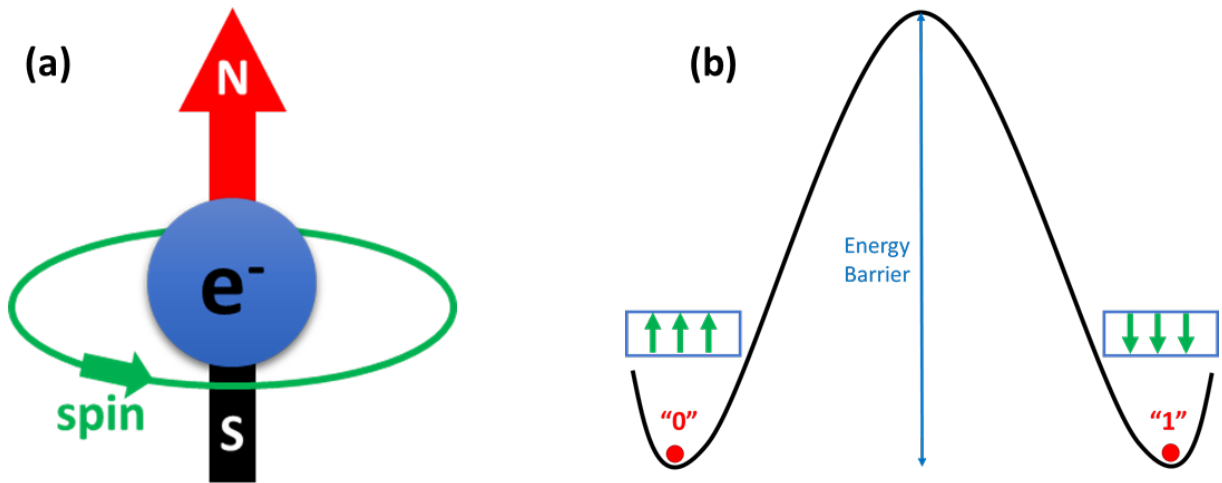
Figure 1.2. Adding spin to electronics. (a) An electron has a spin degree of freedom in addition to its charge. This simplistic cartoon captures the intrinsic built-in magnetic properties of an electron. Electron spins can be used for manipulating the magnetic order of magnets. (b) Magnetic memories encode information (bits "0" and "1") in their magnetic order. In typical magnetic memories, bistability exists along an axis, with magnetization pointing in opposite directions. There is an energy barrier between the bistable states; if the energy barrier is large enough, we can have non-volatile memories.

1.2   MAGNETIZATION DYNAMICS AND SPIN TORQUES

In the random-access magnetic memories (MRAM) that we pursue, information is encoded in the magnetic order of the magnet, and the spin of conduction electrons is used to manipulate the magnetic order. In a magnetic material (ferro-, ferri-, or antiferro-magnet), neighboring localized electron spins are exchange-coupled together and form a magnetic order below a critical temperature. Consequently, the physics of magnetism is in principle the physics of angular momentum. In order to switch the magnetic order below the critical phase transition

temperature, we would need to exchange angular momentum with the magnetization by applying torque on it, provided by an effective magnetic field. Assuming that the magnitude of magnetization is conserved at all times, we can follow the phenomenological Landau-Lifshitz-Gilbert (LLG) formalism for magnetization dynamics (8, 9):

$$\frac{\partial \boldsymbol{m}}{\partial t} = -\gamma \boldsymbol{m} \times \boldsymbol{H}_{eff} + \alpha \boldsymbol{m} \times \frac{\partial \boldsymbol{m}}{\partial t}. \tag{1.1}$$

Here, $\boldsymbol{m}$, $\boldsymbol{H}_{eff}$, γ, α are the unit vector of magnetization, effective magnetic field, gyromagnetic ratio, and Gilbert damping parameter, respectively. The first term on the right-hand side shows the magnetization precession around the effective magnetic field, and the second term shows the damping. The effective magnetic field includes the electrically controlled terms allowed by spin-orbit interaction, external magnetic field, exchange field, dipolar field, and crystalline anisotropy effective fields. Effective magnetic field could be derived from a free energy density F as: $\boldsymbol{H}_{eff} = -\delta_{\boldsymbol{M}} F$. Anisotropy fields arise because of the spin-orbit interaction and set a preferred axis for the magnetization along which the free energy of the system is minimized. This kind of axis is known as the easy axis, and if only one such axis exists in the material system then the magnet has a uniaxial anisotropy and the data stored in the magnetization becomes binary. This is schematically pictured in Figure 1.2 (b).

One of the main themes of spintronics is providing the effective magnetic field via conducting electrons spins, since with this approach, devices can be integrated on electronic chips and be compatible with transistor technology, giving rise to an integrated MRAM. Hence, in the first step, we need to create a net spin polarization in the electron current. In normal metals, such as copper, electrons are not spin-polarized, and each electron has a spin in a random direction.

Consequently, when all the spins are added they cancel out and no net spin polarization exists. However, there have been various efforts to create a net spin polarization in an electron current, such as spin-transfer-torque and spin-orbit torque effects, which are described in the following.

Spin transfer torque (STT): One way of creating a net spin polarization in an electron current is by passing it through a magnet. In this way, the angular momentum can be transferred from the magnetization to conducting electrons, resulting in a net spin polarization of current (see Figure 1.3 (a)). This approach was first theoretically proposed by Slonczewski and Berger (*10, 11*), and was experimentally realized in subsequent years (*12, 13*). In this kind of structures, two magnetic layers separated by a non-magnetic spacer are used, one with a fixed magnetization and the other one with a free magnetization. Such structures are called spin-valves when conductive spacers are used. As electron current goes through the fixed layer it gets spin-polarized through the exchange of angular momentum with the magnetization. Then this spin-polarized current goes through the free layer and exchanges angular momentum by applying torque on the magnetization. In this way, spin angular momentum is transferred from the fixed to the free layer, hence, it is called spin transfer torque.
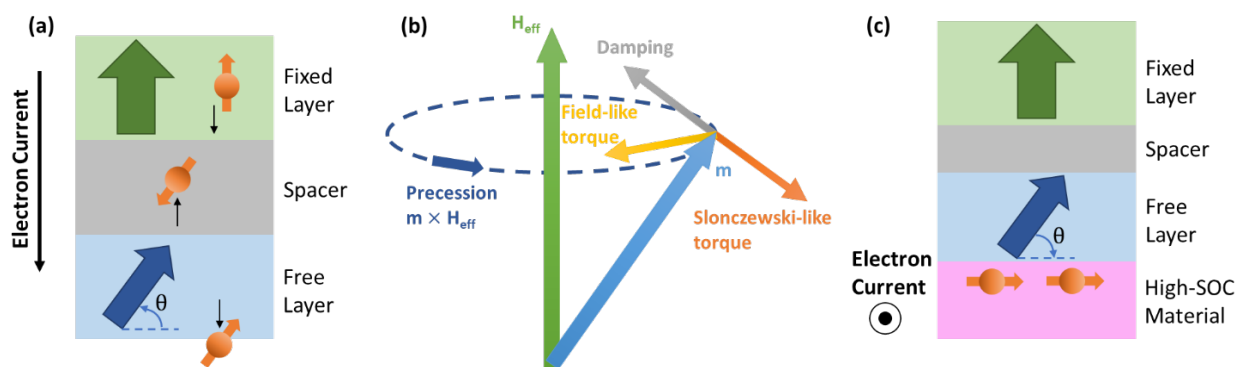
Figure 1.3. Spin torques. (a) Spin transfer torque in a spin-valve structure. A current of spin-polarized electrons flows from the fixed layer to the free layer and exerts torques on the magnetization. Anti-parallel

spin-polarization (with respect to magnetization) is reflected from the free layer's interface, and parallel polarization passes through. (b) LLG dynamics illustration, including the spin torques. $\mathbf{H}_{eff}$ and $\mathbf{m}$ represent the effective magnetic field and a unit vector of magnetization. (c) Spin-orbit torque in a magnetic tunnel junction structure. Applying electron current to a material with high spin-orbit coupling results in a net spin-polarization at its interfaces (in a structure with broken inversion symmetry). This spin-polarization exerts torques on magnetization. Here, the spacer and fixed layers do not play an active role for switching, they are only used for electrical readout of the magnetization state.

In a simple picture, when a spin-polarized current passing through a ferromagnetic layer has its spin polarized at some angle θ with respect to the magnetization, only the spin-polarization component parallel to the magnetization can pass through unchanged (transmission/reflection proportional to $\cos\theta$, where positive/negative signs imply transmission/reflection). Consequently, the component perpendicular to the magnetization is absorbed by the ferromagnet, causing the magnetization to rotate. We can modify the LLG equation by including the spin-transfer torques (*14*):

$$\frac{\partial \boldsymbol{m}}{\partial t} = -\gamma \boldsymbol{m} \times \boldsymbol{H}_{eff} + \alpha \boldsymbol{m} \times \frac{\partial \boldsymbol{m}}{\partial t} + \boldsymbol{\tau}, \tag{1.2}$$

where $\boldsymbol{\tau}$ denotes the spin-torques. There are two kinds of spin-torques, similar to the damping-like and precession-like components of the LLG equation, as shown in Figure 1.3 (b). There is a detailed discussion on the symmetries of these torques in Chapter 2, but here we just briefly mention their forms. The first kind is called the Slonczewski (or damping-like) torque:

$$\boldsymbol{\tau}_D \propto \boldsymbol{m} \times (\boldsymbol{m} \times \boldsymbol{J}_s), \tag{1.3}$$

where $\boldsymbol{J}_s$ is the spin current. For the Slonczewski-like torque, the angular momentum of the injected spin current is absorbed by the ferromagnet in the form of a torque (hence, damping-like torque). The other term is called the field-like torque:

$$\boldsymbol{\tau}_F \propto \boldsymbol{m} \times \boldsymbol{J}_s. \tag{1.4}$$

7

For this torque, a net spin accumulation at the interface acts like an effective magnetic field and applies a torque on the magnetization (hence, field-like torque). The efficacy of STT for transferring angular momentum depends on the applied current density and the polarization of the current, which can be 100% at the best case, setting an upper limit for the switching efficiency. STT also has several other disadvantages. For the readout of such memory devices, the state-of-the-art method relies on tunneling magnetoresistance (TMR) effect (*15-17*). In TMR structures, two magnetic layers are separated by an insulating tunneling barrier (spacer), where the resistance of the stack will be high (low) if the two magnetizations are anti-parallel (parallel) to one another. In STT, we need to apply large current densities through the spacer layer (~ 10^7 A/cm^2), however, applying such large current densities through an insulating layer will damage it over time and will result in low endurance (because of electromigration). Furthermore, in a practical device, the relative stable magnetization states of the free/fixed layer are either parallel ($0°$ angle) or anti-parallel ($180°$ angle). In both of these cases, no spin angular momentum can be transferred between the two, as the strength of transfer comes from a torque and has an angular dependence of the form $|\sin\theta|$, where θ is the relative angle between the two magnetizations. Consequently, the STT relies on thermal fluctuations of the two magnetizations, hence, it has an incubation time and a slow switching speed. The state of the art switching speed with STT is on the order of 5-10 ns (*18*). These fundamental limits of STT have been the motivation for finding other methods of transferring angular momentum, such as spin-orbit torques.

Spin-orbit torque (SOT): Another method of creating a net spin-polarization in a current can be based on spin-orbit interaction. The general idea is that in materials with high spin-orbit coupling (SOC), by applying electric fields one can manipulate the orbital degree of freedom, and then

through the SOC, the spin degree of freedom and the magnetic order can also be manipulated indirectly.

Fundamentally, spin-orbit interaction is a relativistic effect which can be derived from Dirac's equation resulting in the following Hamiltonian (*19*):

$$H_{SO} = -\frac{\hbar}{4m_0^2 c^2} \boldsymbol{\sigma} . (\boldsymbol{p} \times \boldsymbol{\nabla} V_0), \tag{1.5}$$

where $\hbar$, m_0, $\boldsymbol{\sigma}$, $\boldsymbol{p}$, V_0 are reduced Planck constant, electron's mass, Pauli spin matrix vector, momentum, and the atomic potential, respectively. This relativistic effect becomes important for elements with high atomic numbers, such as 5d heavy metals W, Pt, Ta, Hf, Ir, etc.

Typical ferromagnets that have a strong magnetization at room temperature have a relatively small SOC (3d metals such as Co, Fe, Ni). However, if such ferromagnets are interfaced with heavy metals, one can have both a strong magnetization and a strong SOC in the heterostructure (see Figure 1.3 (c)). It should be noted that for the SOT effect to show up, both the large SOC and a breaking of inversion symmetry are required. But in a heterostructure of heavy metal / ferromagnet, inversion symmetry is naturally broken along the growth (z) direction.
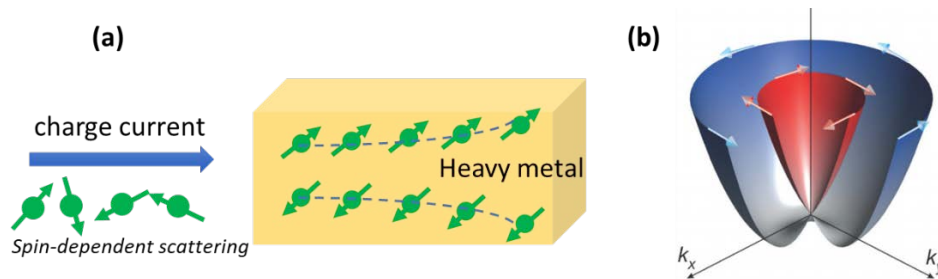
Figure 1.4. Microscopic origins of spin-orbit torques. (a) Spin Hall effect. Spin-dependent scattering mechanisms give rise to a net spin-polarization at the heavy metals edges. Charge current, spin polarization, and deflection directions (spin current direction) are all perpendicular to one another. (b)

There are several SOC-based microscopic effects that give rise to a net spin polarization when inversion symmetry is broken (*21*). In one scenario, SOC generates a spin current in a nonmagnetic metal layer due to the spin Hall effect (see Figure 1.4 (a) right) (*22-24*). The spin current propagates towards the heavy metal interface, where it can be absorbed by an adjacent ferromagnetic layer in the form of magnetization torques (in specific, damping-like torque). Spin Hall effect originates from asymmetric spin scatterings in the bulk of the heavy metal, and it results from three main mechanisms: intrinsic effects, skew scattering, and side-jump mechanism (*25*). All of these effects rely on SOC and generally obey the form and symmetries of Equation 1.5. The magnitudes of charge and spin current in the spin Hall effect are related via the spin Hall angle, defined as (*26*):

$$\theta_{SH} = \frac{2e}{\hbar} \frac{J_s}{J_c}, \qquad (1.6)$$

where e, $\hbar$, J_s, and J_c are the electron charge, the reduced Planck constant, spin current density, and charge current density, respectively. In heavy metals such as W, Ta or Pt, the spin Hall angle is roughly on the order of 0.1 (*27*).

In another scenario, a charge current flowing parallel to an interface with broken inversion symmetry obtains a net spin polarization due to SOC, which can in turn exert torque on an adjacent ferromagnet via exchange coupling. Different names have been attributed to this mechanism in literature, such as the Rashba-Edelstein (*28, 29*), or inverse spin galvanic effect. This effect is a result of the band structure obtaining a spin texture that is odd in momentum (see Figure 1.4 (b)). Following the SOC Hamiltonian in Equation 1.5, there can be an effective electric

field at the heterostructure interfaces where the inversion symmetry is broken along the growth direction (denoted as $\hat{z}$). In such cases, we can write the Rashba Hamiltonian as:

$$H_R = \alpha_R \boldsymbol{\sigma}.(\boldsymbol{p} \times \hat{z}), \qquad (1.7)$$

where $\boldsymbol{\sigma}$ and $\boldsymbol{p}$ are the Pauli matrices and electron momentum, and α_R is the material-dependent Rashba constant. Thus, as a result of the Rashba effect, a net spin polarization along the $\boldsymbol{p} \times \hat{z}$ direction will be created at the heavy metal/ferromagnet interface. This net spin polarization can in principle apply field-like torque on the magnetization, and upon diffusion into the ferromagnet, it can also apply a damping-like torque.

It should be noted that microscopic origins of SOTs are not limited to spin Hall or Rashba-Edelstein effects (*30, 31*), however, these two are dominant in conventional heavy metal/ferromagnetic systems. But in general, other effects, such as quantum spin Hall effect in topological insulators, can also give rise to SOTs (*32-35*).

1.3   SPIN-ORBIT TORQUE SWITCHING OF MAGNETIZATION

From an applications point of view, we are more interested in switching magnets with perpendicular anisotropy, meaning that the two stable magnetization states are along the heterostructures interfaces normal (referred to as up/down states). The reason is that magnets with perpendicular anisotropy have better scaling properties compared to the ones with in-plane anisotropy (*36*); for in-plane anisotropy one needs to use the shape anisotropy to break the in-plane symmetry for obtaining well-defined "up/down" states, but keeping the aspect ratio of shape anisotropy is not practical at scaled feature sizes of around 20 nm. Consequently,

perpendicular anisotropy in circular-shaped devices is a better practical choice for high device densities.

With all the considerations discussed so far, the heterostructure of interest consists of the following layers: a heavy metal to provide the SOC, a ferromagnet to store the magnetic states, and an oxide that can be used as the tunneling barrier for TMR readout in magnetic tunnel junctions (MTJ) (see Figure 1.3 (b) and Figure 1.5 (a)). However, we can immediately see that a major problem for SOT switching in this scenario shows up: if we have an in-plane rotation invariance in our films, then the resulting spin-polarization is always in the in-plane direction (this will be discussed in more detail in Chapter 2). In other words, J_s mentioned in Equations 1.3 and 1.4 lies in the in-plane direction (and is perpendicular to the current direction). However, with the magnetization having stable states in the out-of-plane direction, we can see that there is a complete symmetry between the up/down states from the point of view of spin polarization. In other words, if the SOTs can induce a switching from up to down, they should also be able to induce switching from down to up, and as a result, no switching can happen in the system (see Figure 1.5 (a)) (*37*). The reason for this symmetry is that the stable magnetization states and the SOT effective fields are always perpendicular to one another. The damping-like effective field ($\boldsymbol{H}^{DL}$) has the form of

$$\boldsymbol{H}^{DL} \propto \boldsymbol{m} \times \boldsymbol{J_s},\tag{1.8}$$

and the field-like effective field ($\boldsymbol{H}^{FL}$) has the form of

$$\boldsymbol{H}^{FL} \propto \boldsymbol{J_s},\tag{1.9}$$

which follows from Equations 1.3 and 1.4 (noting that torque τ and effective magnetic fields H are related as $\tau \propto m \times H$). With perpendicular stable magnetization states and in-plane spin current, we can see that both effective SOT fields are pointing in the in-plane direction.
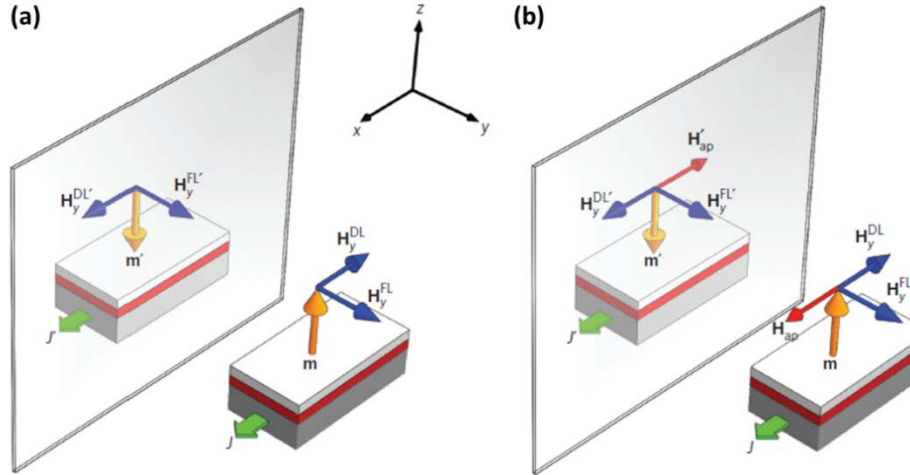
Figure 1.5. Symmetries of spin-orbit torque switching, taken from Ref. (*37*). (a) Symmetry between up/down magnetization states from the point of view of SOTs, shown in a structure with perpendicular magnetic anisotropy. Here, the current is applied along the x axis, and the structure is assumed to have rotation invariance around the growth direction (z axis). (b) Deterministic SOT switching by applying an external magnetic field (H_{ap}), collinear with the current. By fixing the direction of H_{ap}, a unique perpendicular magnetization direction can be chosen for each current polarity ($\pm \hat{x}$).

In this scenario, applying the SOTs does not result in a **deterministic switching** of perpendicular magnetization. In order to realize the deterministic switching, one must break the symmetry between the up/down states. In the earlier works on SOTs, this symmetry was broken by applying a fixed external magnetic field, collinear with the current ($\boldsymbol{H}_{ap}$) (*38-40*), so both a current and an external magnetic field were required (see Figure 1.5 (b)). The deterministic switching in this case can be qualitatively understood by considering the combined action of the damping-like SOT effective field ($\boldsymbol{H}^{DL}$) and the external magnetic field (*21*); if $\boldsymbol{H}^{DL}$ and $\boldsymbol{H}_{ap}$ are initially parallel, the

13

magnetization can start the rotation and will be switched. However, if H^{DL} and H_{ap} are initially anti-parallel, the switching cannot happen. In other words, the presence of a fixed H_{ap} breaks the magnetization reversal symmetry for the up/down states; parallel H^{DL} and H_{ap} is energetically different from anti-parallel H^{DL} and H_{ap}, hence, we can have deterministic magnetization switching.

Although this strategy of using an external magnetic field for breaking the symmetry has been successful for research purposes, however, using an external field is not practical in device applications. This is a persistent challenging issue for the SOT technology, and there is a critical need for a practical solution to the **field-free deterministic switching** problem (i.e., realizing deterministic switching without using any external magnetic fields). This is the main problem that the research presented in this PhD dissertation is trying to address: how can we deterministically switch the perpendicular magnetization with SOTs, and without any external magnetic fields? We present practical solutions to this problem that could be employed on the industrial scales with the hope of paving the way for the implementation of SOT technology for switching of perpendicular magnetization in integrated non-volatile random-access memories.

In Chapter 2 we discuss the symmetries of spin-orbit torques in detail, and we show how they are related to the structural symmetries of the devices. In Chapter 3 we show that deterministic field-free SOT switching could be realized using an in-plane exchange bias field, in two different material systems of Pt-CoFe-IrMn and IrMn-CoFeB-MgO. In Chapter 4 we show that by breaking the structure's in-plane symmetry during the sputtering process, we can create current-induced out-of-plane effective magnetic fields that can break the symmetry between up/down states for

each current polarity and realize deterministic SOT switching. We also show that the latter approach can be very suitable for practical devices and can potentially solve the problem of deterministic field-free SOT switching for industrial applications. In Chapter 5 we discuss other related effects that arise because of the Dzyaloshinskii-Moriya interaction (DMI, which is the anti-symmetric exchange interaction). These works are enabled and motivated by the IrMn-CoFeB-MgO material system that we initially developed for SOT switching. Specifically, by discussing several works, we show that we can create/annihilate non-volatile magnetic skyrmions by a single gate voltage pulse in the IrMn-CoFeB-MgO system, without the requirement of any additional external magnetic fields.

2 SPIN-ORBIT TORQUES SYMMETRIES

In this chapter we take a closer look at the symmetries of spin-orbit torques. In principle, the presence of spin-orbit interaction by itself is not enough to induce net spin-orbit torques. In addition, some structural symmetries should be broken (*37, 41, 42*). First, we consider the conventional SOT heterostructures which consist of sputtered layers that are uniform in the in-plane direction, the kind of which is shown in Figure 2.1 (a). In these cases, the structure lacks inversion symmetry in the growth direction (normal to layers interfaces), which we denote as the z axis, i.e., the structure lacks mirror symmetry with respect to the x-y plane. On the other hand, mirror symmetries with respect to all the planes that are perpendicular to the x-y plane exists in the sample. Furthermore, there is a continuous rotational symmetry about the z axis, which is a result of the polycrystalline nature of the sputtered films. In the following we drive the forms of allowed SOTs based on the symmetry arguments. We follow the discussion provided in Ref. (*41*) closely.

We consider an in-plane applied current that results in a spin accumulation $\delta\boldsymbol{m}$, through either the spin Hall or Rashba-Edelstein effects, as explained in Chapter 1. The spin accumulation $\delta\boldsymbol{m}$ acts as an effective magnetic field on the magnetization and applies torques on it, with the form of $\boldsymbol{\tau} = \boldsymbol{m} \times \boldsymbol{B^I}$, where $\boldsymbol{\tau}, \boldsymbol{m}$, and $\boldsymbol{B^I}$ are the torque, magnetization, and the effective magnetic field created by $\delta\boldsymbol{m}$ (i.e., $\boldsymbol{B^I} \propto \frac{\delta m}{m}$), respectively (*41*). In other words, $\boldsymbol{\tau}$ denotes the spin-orbit torques, and effective SOT fields are proportional to $\delta\boldsymbol{m}$. The torque only depends on the components of $\boldsymbol{B^I}$ that are perpendicular to $\boldsymbol{m}$, hence we will only consider such components.
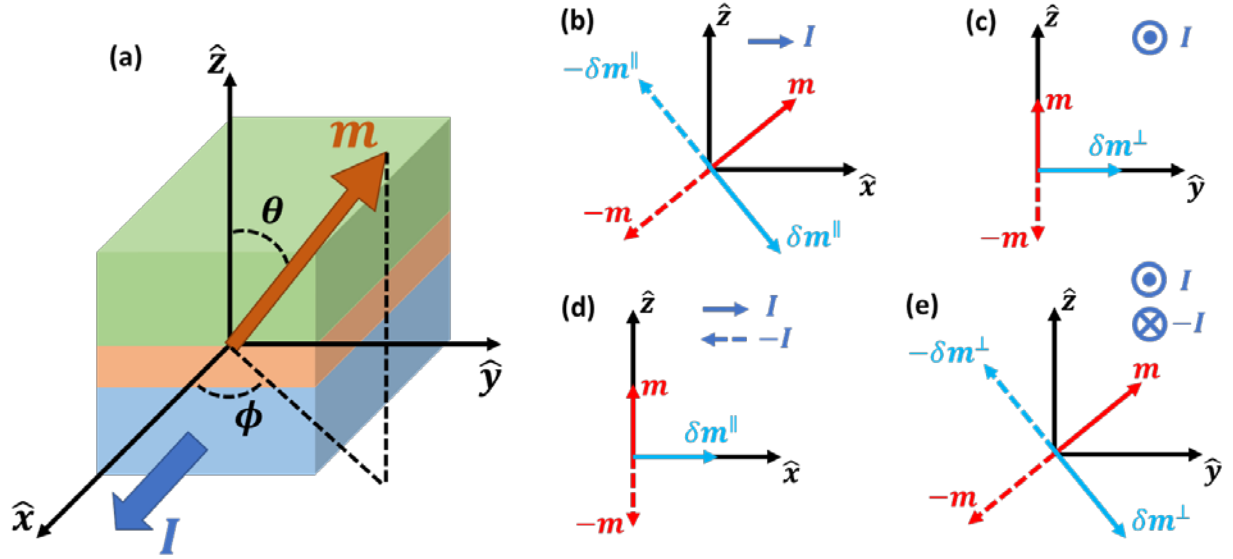
Figure 2.1. Transformation of applied current (I), magnetization (m), and spin accumulation ($\delta m^{\perp}$ and $\delta m^{\parallel}$) under mirror reflections. (a) Schematics of the studied heterostructure, consisting of a high-SOC layer, a ferromagnet, and an oxide. The structure lacks inversion symmetry along the z axis. (b-c) Magnetization in the $x-z$ plane with mirror reflection in the $x-z$ plane. The negative sign and dashed lines represent the mirrored vectors. (d-e) Magnetization in the $y-z$ plane with mirror reflection in the $y-z$ plane. Here, we are closely following the discussions in Ref. (*41*).

First, we consider the case where the magnetization is in the $x-z$ plane and electron current I is applied in the x direction. We are interested in exploring effective SOT fields that are linear with the current and are a function of both the current and the magnetization m. Based on the symmetry arguments, we can see that two forms of δm are allowed: (i) a longitudinal one $\delta m^{\parallel}$, which lies in the $x-z$ plane, and (ii) a transverse one $\delta m^{\perp}$, which in general is in the $y-z$ plane and in this case points in the y direction (see Figure 2.1 (b-c)). We should note that we are only considering the spin accumulation δm that is perpendicular to the magnetization, hence, δm can be decomposed into the two longitudinal and transverse terms. Let us now look at the vector transformations under symmetry operations. First, we look at mirror reflection with respect to the $x-z$ plane. Electric current I is invariant under such a reflection, however, both m and $\delta m^{\parallel}$ are inverted since they are axial vectors. On the other hand, $\delta m^{\perp}$ remains invariant.

17

Consequently, $\delta\boldsymbol{m}^\parallel$ has to be an odd function of $\boldsymbol{m}$, while $\delta\boldsymbol{m}^\perp$ should be an even function. We can arrive at the same conclusion by looking at the mirror reflection by the $y-z$ plane and then 180° rotation around the z axis. On the other hand, since the structure lacks inversion symmetry along the z axis, there is no symmetry operation that forbids either $\delta\boldsymbol{m}^\parallel$ or $\delta\boldsymbol{m}^\perp$ (*41*). As an example, let us assume that the structure has inversion symmetry. In this case, electron current will change sign under inversion, but $\boldsymbol{m}$ and $\delta\boldsymbol{m}$ would remain the same. As a result, currents in both directions should yield the same spin accumulation, meaning that the spin accumulation should be zero in the linear regime.

Next, we consider the case where the magnetization is in the $y-z$ plane and electron current is applied in the x direction. Here, $\delta\boldsymbol{m}^\parallel$ is along the x axis, and $\delta\boldsymbol{m}^\perp$ is in the $y-z$ plane (noting that we only consider $\delta\boldsymbol{m}$ perpendicular to the magnetization $\boldsymbol{m}$), as shown in Figure 2.1 (d-e). Mirror reflection in the $y-z$ plane inverts the electric current $\boldsymbol{I}$, $\boldsymbol{m}$, and $\delta\boldsymbol{m}^\perp$, but not $\delta\boldsymbol{m}^\parallel$. As a result, and within the linear regime, $\delta\boldsymbol{m}^\perp$ is an even function of $\boldsymbol{I}$, and $\delta\boldsymbol{m}^\parallel$ is an odd function, just like the previous case. We arrive at the same conclusion by looking at the mirror reflection in the $x-z$ plane followed by 180° rotation around the z axis. In the special case of $\boldsymbol{m} \parallel y$, the spin accumulation $\delta\boldsymbol{m}$ vanishes. However, if magnetization has a non-zero out-of-plane component then we will not have this problem. Since we are considering the linear response regime, we can find the general forms of $\delta\boldsymbol{m}^\parallel$ and $\delta\boldsymbol{m}^\perp$ by a superposition of the two presented cases for any magnetization direction.

Summarizing the results so far and considering the lowest order contributions, we have shown that for $\boldsymbol{m}$ in the $x-z$ plane (*41*):

$$\delta\boldsymbol{m}^{\parallel} \propto I\,\boldsymbol{m} \times \hat{y}, \tag{2.1}$$

$$\delta\boldsymbol{m}^{\perp} \propto I\,\hat{y}, \tag{2.2}$$

where I denotes the electron current magnitude. For the $\boldsymbol{m}$ lying in the $y-z$ plane we have:

$$\delta\boldsymbol{m}^{\parallel} \propto I\,\boldsymbol{m} \times \hat{y}, \tag{2.3}$$

$$\delta\boldsymbol{m}^{\perp} \propto I\,(\boldsymbol{m} \times \hat{y}) \times \boldsymbol{m}. \tag{2.4}$$

We can now find the effective spin-orbit torques as $\boldsymbol{\tau} \propto \boldsymbol{m} \times \delta\boldsymbol{m}$. Both cases discussed above will yield a similar result for the spin-orbit torques forms, consequently we can summarize the allowed torques as:

$$\tau^{\parallel} \propto I\,\boldsymbol{m} \times (\boldsymbol{m} \times \hat{y}), \tag{2.5}$$

$$\tau^{\perp} \propto I\,\boldsymbol{m} \times \hat{y}, \tag{2.6}$$

which correspond to the damping-like and field-like torques of Eqs. 1.3 and 1.4, respectively, by noting that the spin current $\boldsymbol{J}_s$ points along the y axis. In other words, we can see that by only invoking the symmetry arguments, the allowed spin current lies in the in-plane direction and is perpendicular to the electron current, i.e., it is perpendicular to both the current and inversion asymmetry directions. Based on these arguments, we can generalize Eqs. 2.3 and 2.4 to obtain the generic allowed current-induced SOT effective fields (43):

$$\boldsymbol{B}^{I} \propto I\,\boldsymbol{m} \times \left(\hat{k} \times \boldsymbol{i}\right) + \beta I\left(\hat{k} \times \boldsymbol{i}\right), \tag{2.7}$$

where $\boldsymbol{B}^{I}$, $\hat{k}$, and $\boldsymbol{i}$ are the SOT effective fields, unit vector along the inversion asymmetry direction, and unit vector along the current direction. The first term on the right side shows the

damping-like effective field, the second term shows the field-like effective field, and β denotes the relative magnitude between the two terms.

In the following, we focus on the case where in addition to the structural asymmetry in the z direction, the structure also lacks an inversion symmetry along the y axis, which is transverse to the current direction. This case has practical importance for realizing deterministic SOT switching of perpendicular magnetization, which will be discussed in detail in Chapter 4. In this scenario, the structure only has a mirror symmetry with respect to the $y - z$ plane, and it no longer has the continuous rotational symmetry around the z axis. In other words, $\hat{k}$ (from Eq. 2.7) has components along both the y and z axes. Consequently, for current applied in the x direction, we can write the general forms of spin-orbit torques ($\boldsymbol{m} \times \boldsymbol{B}^I$) as (*43*):

$$\boldsymbol{\tau}_{SOT} = \gamma H_y^{FL} \boldsymbol{m} \times \hat{y} + \gamma H_y^{DL} \boldsymbol{m} \times (\boldsymbol{m} \times \hat{y}) + \gamma H_z^{FL} \boldsymbol{m} \times \hat{z} + \gamma H_z^{DL} \boldsymbol{m} \times (\boldsymbol{m} \times \hat{z}), \quad (2.8)$$

where γ is the gyromagnetic ratio. Here, H_y^{FL} and H_y^{DL} denote the strengths of the conventional field-like and damping-like SOTs. H_z^{FL} and H_z^{DL} show the strengths of the additional field-like and damping-like SOTs emerging because of the reduced symmetry. We will show in Chapter 4 that these additional SOT terms can be used for realizing deterministic SOT switching of perpendicular magnetization without any external magnetic fields.

3 DETERMINISTIC SPIN-ORBIT TORQUE SWITCHING WITH AN IN-PLANE EXCHANGE BIAS

3.1 GENERAL IDEA AND BACKGROUND

In this chapter, the focus is on the experimental results of deterministic field-free SOT switching using an in-plane exchange bias field. As discussed in Chapter 1, an external in-plane magnetic field collinear with current can break the symmetry between up/down states, resulting in deterministic switching of perpendicular magnetization. Although the application of an external field is not a practical solution, but if a fixed in-plane magnetic field is integrated in the device structure, then one can realize the deterministic switching in a practical way. This is the main idea behind the work presented in this chapter: replacing the external field with a built-in exchange bias field.

But how can we integrate fixed magnetic fields inside the SOT heterostructure? It has been long known that at the interface of an antiferromagnet and a ferromagnet, a built-in fixed magnetic field could be created, which is called the exchange bias field (*44*). In a simple antiferromagnet, neighboring spins point in opposite directions, as a result, antiferromagnets have no net magnetization although they have a magnetic order. Consequently, they have a very weak response to external magnetic fields. When ferromagnetic-antiferromagnetic interfaces are cooled through the Néel temperature (T_N) of the antiferromagnet (with the Curie temperature T_C of the ferromagnet larger than T_N), an exchange bias is introduced in the ferromagnet which causes shifts in its hysteresis loop (see Figure 3.1 (a)). This exchange bias field could be viewed as

a kind of fixed built-in magnetic field, if the heterostructure is kept below T_N and the blocking temperature (the temperature at which the exchange bias vanishes) (see Figure 3.1 (b)).
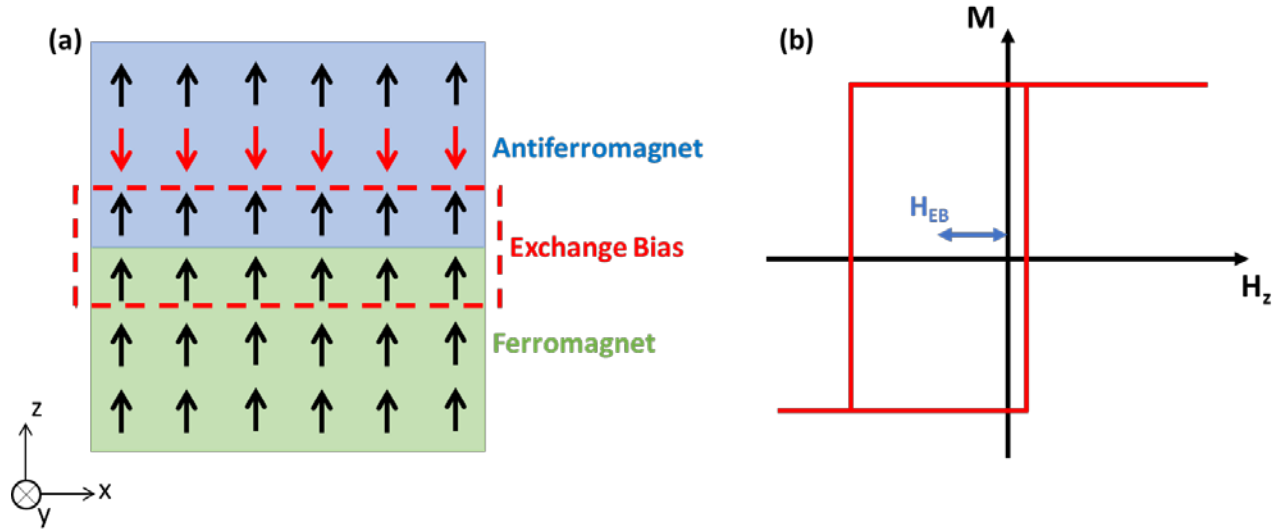
Figure 3.1. Exchange bias field. (a) The exchange bias field may be created at an antiferromagnet-ferromagnet interface. (Note: antiferromagnets have many different types, the cartoon here only shows a specific type of antiferromagnets, but the arguments are generic). (b) Exchange bias field (H_{EB}) manifested as a shift in the ferromagnet's hysteresis loop. The amount of shift from zero field corresponds to H_{EB}. Here, it is assumed that the exchange bias is along the z axis, consistent with the picture on the left side.

In practice, in order to induce exchange bias along a certain direction, one has to anneal the sample at a temperature higher than the antiferromagnet's T_N (or alternatively, higher than the blocking temperature in thin films), with an applied magnetic field along that direction.

We discuss the experimental results in the following. It should be noted that the work presented in this chapter (on Pt-CoFe-IrMn material system (*45*)) was not the first published work to realize deterministic SOT switching with the exchange bias. Several other similar works were also published around the same time (*46-49*). However, we have done a comprehensive study of several crucial aspects of these devices, including a quantitative characterization of switching percentage, Joule heating effect, and exchange bias training effect.

3.2 Materials and Experimental Setup

The samples consisting of Ta(2)/Pt(3)/CoFe(0.9; 1.1)/IrMn(3)/Pt(1) (thicknesses in nm) were grown on Si/SiO2 substrates by DC magnetron sputtering at room temperature. Here, the bottom Ta serves as a buffer layer, Pt(3) is the main heavy-metal which provides the SOTs, CoFe is the ferromagnet in which the magnetization is switched, IrMn is an antiferromagnet which provides the necessary exchange bias, and the top Pt(1) layer serves as capping to protect the sample from exposure to air. We chose Pt(3) here because it is known to have a high SOC and SOTs. Also, Pt has a spin diffusion length of around 2-3 nm and increasing its thickness beyond that will not help with the increasing of SOTs. We chose CoFe(~ 1 nm) because CoFe has a very high Curie temperature and 1 nm thickness of it can promote perpendicular magnetic anisotropy. Furthermore, IrMn has a high T_N and is commonly used in magnetic devices, and it can give rise to a sizable exchange bias at room temperature.

In order to characterize the magnetic properties, we mostly use anomalous Hall effect by reading the Hall voltage in our magnetic system. The anomalous Hall resistance (R_H) is proportional to the z (out-of-plane) component of magnetization. The studied samples all have perpendicular magnetic anisotropy, which means that the anomalous Hall resistance is a suitable measure for magnetic characterization. For the measurements, the samples were patterned into an array of Hall bar devices by standard photolithography and dry etching techniques. The Hall bars have dimensions of 20 μm × 130 μm. These devices were measured using a Keithley 6221 current source, a Keithley 2182A nano-voltmeter and a Stanford Research Systems SR830 lock-in amplifier. For low temperature measurements, physical properties measurement system (PPMS) was used. The external magnetic field was generated by an electromagnet, driven by a Kepco

power supply. Almost all measurements were carried out at room temperature, unless specified.

All the magnetic characterizations were done on the device level rather than the film level, in

order to be more consistent with the rest of the results. The resistance characterizations were

carried out using four-probe measurements.

The current-driven field-free SOT switching mechanism is depicted in Figure 3.2 (a). A charge

current passing through Pt generates a spin current via the spin Hall effect (or Rashba-Edelstein

effect), and the resulting spin current exerts torques on the magnetization of the CoFe layer. The

schematic of the measurement is depicted in Figure 3.2 (b).
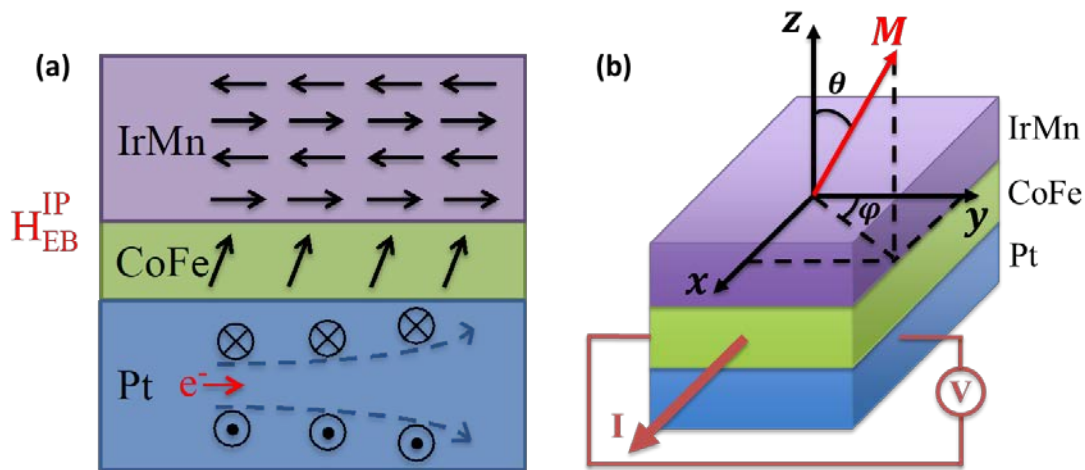
Figure 3.2. Deterministic SOT switching with an in-plane exchange bias. (a) Exchange bias formed at the antiferromagnet-ferromagnet (IrMn-CoFe) interface (H_{EB}^{IP}) enables deterministic switching without any external magnetic fields. Pt provides the necessary SOTs, where the spin Hall effect is schematically depicted inside the Pt layer. (b) The schematics of the measurement configuration using anomalous Hall effect. (45)

The magnetic properties characterized by anomalous Hall measurement are shown in Figure 3.3.

Here, the samples were annealed with an out-of-plane magnetic field of 1 T for 10 minutes,

applied along the z direction. Figure 3.3 (a) and (b) show anomalous Hall resistance as a function

of out-of-plane and in-plane magnetic fields, respectively. In Figure 3.3 (a) the difference

24

between the resistances of two states is defined as ΔR_{field}, which represents the total change in perpendicular magnetization when an out-of-plane external field is used to switch the magnetization. Perpendicular magnetic anisotropy and out-of-plane exchange bias is present in both samples. The abrupt and gradual change of R_H in Figure 3.3 (a) and (b) shows that the sample has perpendicular magnetic anisotropy. The small hysteresis loops in Figure 3.3 (b) may be a result of a slight misalignment between the external in-plane field and the film's surface. It should also be noted that because of the exchange bias, in Figure 3.3 (b) the magnetization does not switch between the two stable states along the easy-axis, only one of the up or down states is observed. Exchange bias is an interfacial effect, so it scales roughly as the inverse of the ferromagnet's thickness (*44*). As expected, the sample with CoFe thickness (t_{CoFe}) of 0.9 nm has a larger exchange bias, because of its thinner ferromagnetic layer. However, for the switching measurements we use the sample with t_{CoFe} of 1.1 nm, since it has a lower anisotropy and switches at lower critical current densities, which reduces the Joule heating effects. We also tried CoFe layers thinner than 0.9 nm, but as expected, they have even larger critical switching currents, and consequently, a more pronounced Joule heating effect. Furthermore, samples with CoFe layers thicker than 1.1 nm do not have a good perpendicular magnetic anisotropy and are not useful for the applications (perpendicular anisotropy is also an interfacial effect).
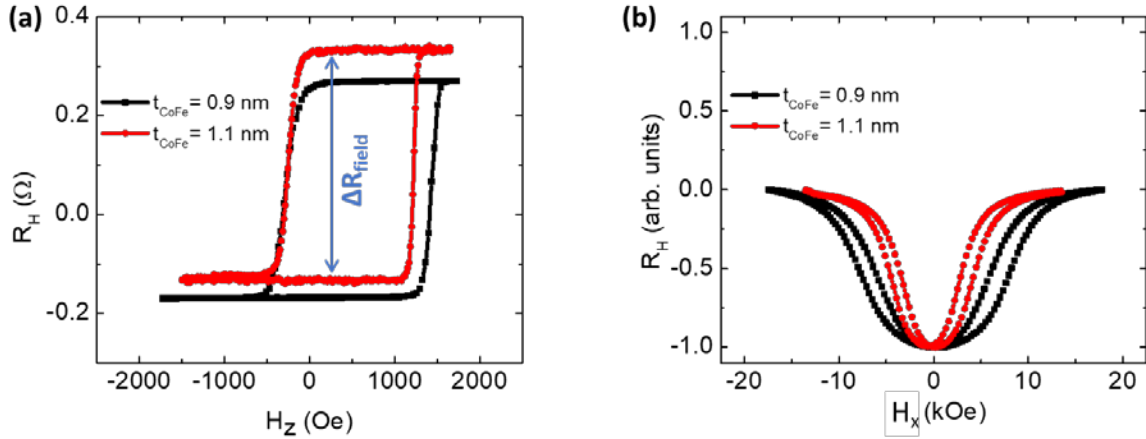
Figure 3.3. Characterization of perpendicular magnetic anisotropy and perpendicular exchange bias in the IrMn-CoFe-Pt material system. (a) Easy-axis hysteresis loop obtained by anomalous Hall resistance (R_H) when magnetic field is scanned along the z axis (H_z). Shift of the hysteresis loop from the zero field is equal to the negative of exchange bias field. ΔR_{field} shows the maximum achievable anomalous Hall resistance when an external field is used to switch all the domains in the device. t_{CoFe} represents the CoFe layer thickness. (b) Hard-axis loops when the external field is scanned along the current (longitudinal $\hat{x}$) direction (H_L). The gradual change in R_H is a result of the sample's perpendicular anisotropy. (*45*)

3.3   SOT Switching with Out-Of-Plane Exchange Bias

We first discuss the situation in which the exchange bias is induced in the out-of-plane direction (such as Figure 3.3) by annealing the sample in the presence of a perpendicular magnetic field. In this case, the exchange bias does not break the symmetry between up/down states, and we need to apply an external magnetic field for deterministic SOT switching. Here, we also show the characterization of SOTs using a harmonics technique (*50-52*). We excite the system with an AC current $I = I_0 \sin \omega t$, and measure the Hall voltage $V_H = I R_H$ at first- (V_ω) and second-harmonics ($V_{2\omega}$). We can find these harmonics components by Taylor expanding Hall resistance up to linear term in I:

$$R_H(I) = R_H^0 + \left(\frac{dR_H}{dI}\right) I. \tag{3.1}$$

26

Hence, we can obtain the first- and second-harmonic voltages as

$$V_\omega(t) = V_\omega \sin \omega t, \quad V_\omega = I_0 R_H^0 \tag{3.2}$$

$$V_{2\omega}(t) = V_{2\omega} \cos 2\omega t, \quad V_{2\omega} = -\frac{I_0^2}{2}\frac{dR_H}{dI} \tag{3.3}$$

The information about spin-orbit torques is contained in the $\frac{dR_H}{dI}$ term.

For the harmonic measurements, a small AC current (with a frequency of 173.333 Hz) is passed through the current channel, in the presence of an in-plane magnetic field, applied along current (voltage) channel for measuring damping-like (field-like) fields. The ratios corresponding to damping-like (B_x) and field-like (B_y) torques are then calculated, (52)

$$B_{x(y)} = -2(\frac{\partial V_{2\omega}}{\partial H_{x(y)}})/(\frac{\partial^2 V_\omega}{\partial H_{x(y)}^2}), \tag{3.4}$$

where V_ω and $V_{2\omega}$ are the first and second harmonic anomalous Hall voltages, respectively. The harmonic voltages are detected using two lock-in amplifiers. Figure 3.4 shows the results for the first and second harmonic measurements, which are fitted by parabolic and linear functions, respectively. Finally, we can obtain the damping-like (ΔH_x) and field-like (ΔH_y) fields, (52)

$$\Delta H_x = (B_x \pm 2\xi B_y)/(1 - 4\xi^2), \tag{3.5}$$

$$\Delta H_y = (B_y \pm 2\xi B_x)/(1 - 4\xi^2), \tag{3.6}$$

where due to our measurement configuration, we use the positive sign in the numerator. It should be noted that in this device, $\xi \equiv \Delta R_P/\Delta R_A = 0.12$, which is the ratio between the planar Hall effect and anomalous Hall effect resistances. To measure ΔR_P (planar Hall effect resistance), a large in-plane field of 1.5 T was applied to the sample to make the magnetization in-plane.

Then, the transverse (along $\hat{y}$) resistance was measured as a function of the angle between the in-plane field and the current direction. ΔR_P is defined as the difference between the maximum and the minimum values of the transverse resistance. Furthermore, ΔR_A (anomalous Hall resistance) is defined in the same way as ΔR_{field}, shown in Figure 3.3 (a).
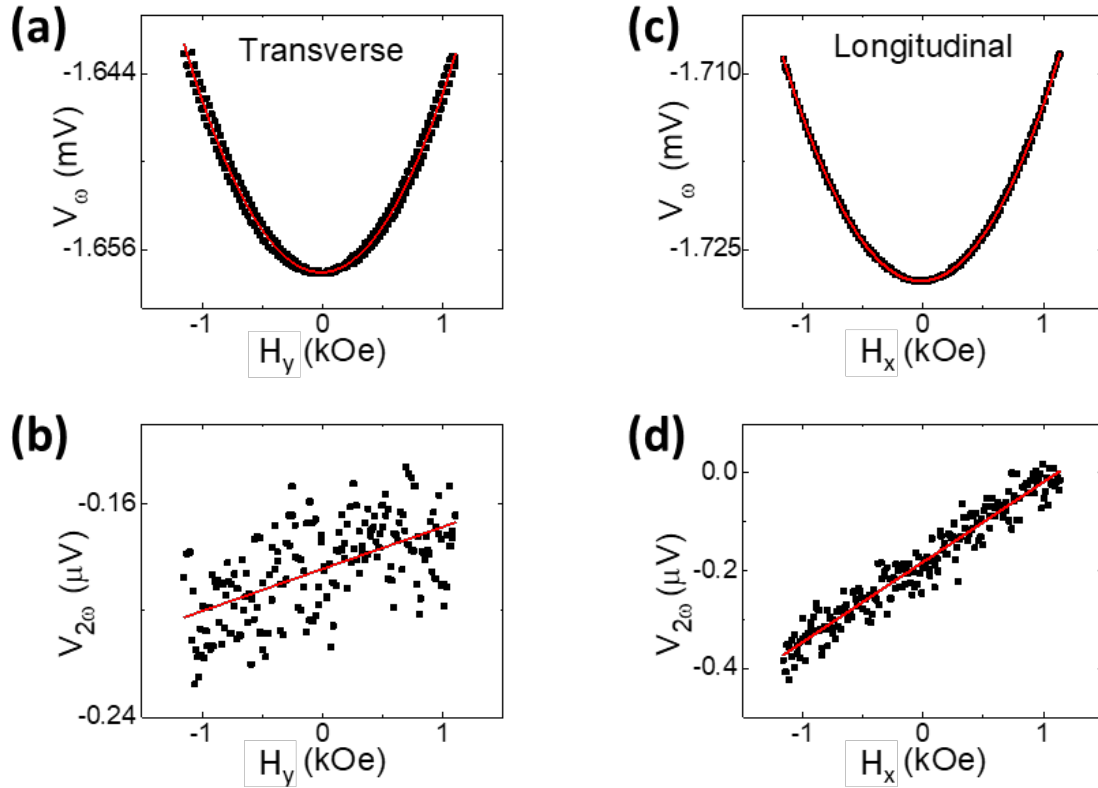
Figure 3.4. Characterization of SOTs in Pt-CoFe-IrMn system, using the harmonics technique. (a)-(b) First and second harmonic Hall voltage signals when the external field is scanned along the transverse $\hat{y}$ direction (with respect to current direction). (c)-(d) First and second harmonic Hall voltage signals when the external field is scanned along the longitudinal $\hat{x}$ direction (with respect to current direction). (*45*)

Figure 3.5 shows the field-like and damping-like fields, at different peak currents. In the small current regime, the effective fields have a linear dependence on the applied current. Based on the resistances of each layer, the portion of current flowing through the Pt layer was calculated. We estimate that about 47% of the total current passes through the Pt layer. Therefore, the

effective damping-like and field-like field efficiencies ($\Delta H_{x(y)}/J$) are calculated to be 22.31 and

7.04 Oe per 10^7 A/(cm)^2, respectively, where J is the peak current density passing through Pt.

These values are slightly smaller than other reported values (*53, 54*). This can be due to the fact

that a much smaller portion of the current passes through the IrMn layer, which also generates

SOT, and its torques tend to partially cancel the torques from the Pt layer, since they have the

same sign of spin Hall angle (*55*). It should be noted that the SOT responsible for switching stems

from the Pt layer, rather than IrMn, because of its much higher conductivity. Assuming that the

damping-like torque is a result of spin Hall effect solely, we can find the spin Hall angle using

$\theta_{SHE} = \frac{-2|e|M_s t_F}{h} \times \frac{\Delta H_L}{J}$, where $|e|$, h, t_F, and M_s represent the absolute value of the electron's

charge, Planck's constant, ferromagnetic layer thickness, and the saturation magnetization of the

ferromagnetic layer (*56*). Using SQUID measurement, the saturation magnetization was found to

be 1100 emu/cm^3. The obtained spin Hall angle for Pt in this structure is 0.082, which is similar

to the other reported values for Pt (*57*).

In order to achieve deterministic switching, we need to break the inversion symmetry, thus, as

expected, the out-of-plane EB does not result in field-free switching. Anomalous Hall resistance

is used for current-driven switching characterization, and the measurement setup is depicted in

Figure 3.2 (b). For the switching measurement, first an initialization current pulse of +60 mA was

applied to the sample. Then, the applied current was swept from +60 mA to −70 mA, and back to

+60 mA, in the presence of different in-plane magnetic fields, which were collinear with the

current direction. To make the switching measurements consistent with the other switching

measurements in this work, pulses with 200 μs widths and a one-second wait between

successive pulses were used to drive the magnetization switching.
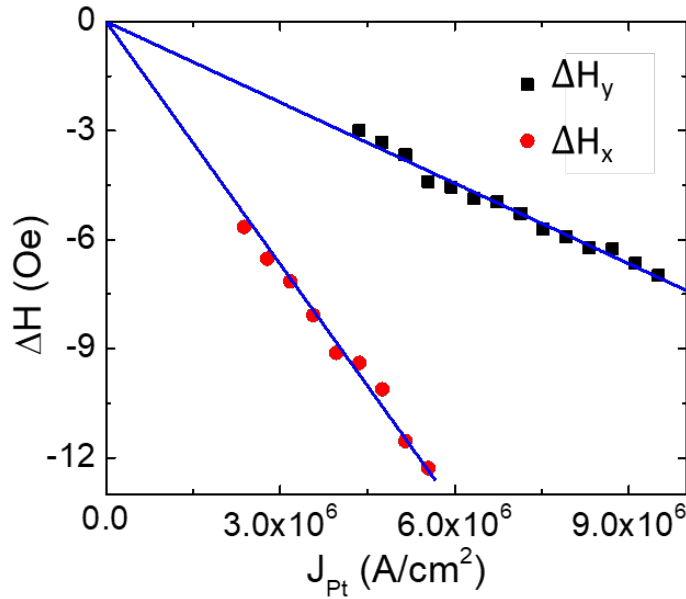
Figure 3.5. Damping-like (ΔH_x) and field-like (ΔH_y) effective fields as a function of the current density through the Pt layer in the Pt-CoFe-IrMn system.

The resulting switching plots are shown in Figure 3.6. The anomalous Hall resistance is proportional to the perpendicular magnetization, thus, in order to better describe the current-driven switching under different in-plane magnetic fields, we look at the total change in anomalous Hall resistance after sweeping the current ($\Delta R_{current}$). On the other hand, ΔR_{field} represents the total perpendicular magnetization reversal when an out-of-plane field is swept. In this case, $\Delta R_{field} = 0.473 \ \Omega$. As can be seen in Figure 3.6 (a), $\Delta R_{current}$ is almost negligible for the zero field case, which shows that there is no field-free switching indeed. Applying negative and positive in-plane fields results in different switching polarities because of the opposite SOT directions (*58*); however, $|\Delta R_{current}|$ is symmetric around the zero field. This shows that there is no shift in the switching diagram, which is reasonable since the exchange bias direction is out-of-plane. The switching diagram is plotted in Figure 3.6 (b). The vertical axis shows $\Delta R_{current}/\Delta R_{field}$, which is plotted as a function of different external in-plane magnetic fields,

H_x. $\Delta R_{current}/\Delta R_{field}$ can be interpreted as the switching percentage of the sample's area (or magnetic domains) as a result of applying current, detected by anomalous Hall effect. In our notations $\Delta R_{current}$ has a positive (negative) value if at large positive currents, the state with positive (negative) anomalous Hall resistance is preferred. Thus, positive and negative values of $\Delta R_{current}$ correspond to different switching polarities. In this case we do not have field-free switching; the very small shift in the switching diagram is negligible and may be due to the remnant in-plane field of the magnet.
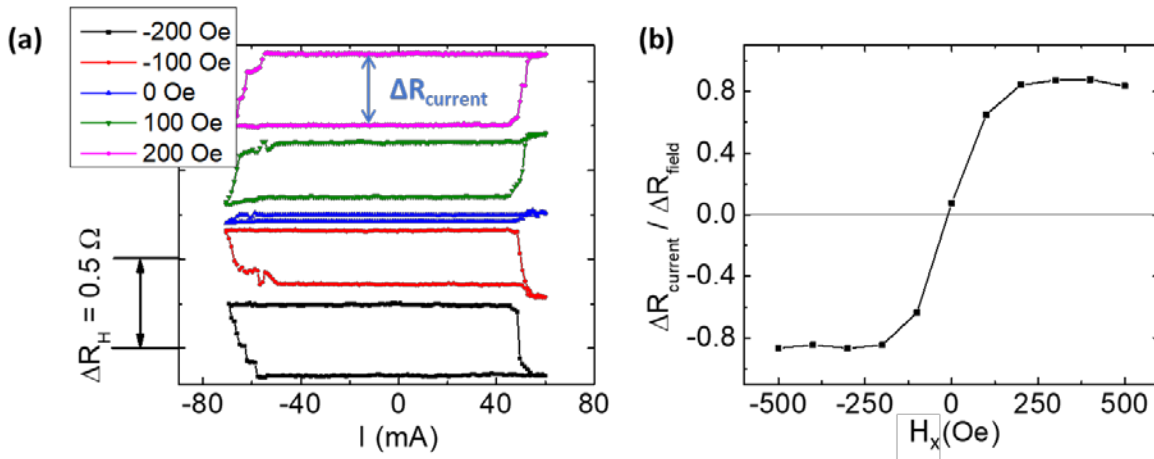
Figure 3.6. Current-driven SOT switching in the sample with out-of-plane exchange bias. (a) Characterization of SOT switching in the presence of different external magnetic fields (H_L). The blue curve shows the results in the absence of external field, where no switching is observed. ΔR_current is defined as the maximum achievable anomalous Hall resistance when the sample is switched with SOTs. A current of 45 mA corresponds to a current density of $\sim 4.7 \times 10^7$ A/cm^2, passing through the Pt layer. (b) SOT Switching percentage plotted as a function of different applied in-plane magnetic fields. Here, ΔR_current is normalized by ΔR_field to show the percentage of switched magnetic domains in the sample. Positive and negative values correspond to different switching polarities (up→ down or down→ up). For this sample, ΔR_field = 0.473 Ω.

As can be seen in Figure 3.6 (b), $\Delta R_{current}$ does not reach 0.473 Ω, even in the presence of larger in-plane magnetic fields, which means that not all of the domains are switched. We suppose this is due to the fact that the current density is smaller on the Hall bar cross section area and does

31

not reach the critical value. Furthermore, the additional pinning effect at the cross section area may make complete switching difficult (*55*). Hence, the cross-section region of the device is not completely switched and $\Delta R_{current}$ does not reach ΔR_{field}. Similar result is typically observed in relatively large Hall bar structures.

3.4   IN-PLANE EXCHANGE BIAS CHARACTERIZATION IN PT-COFE-IRMN SYSTEM

In order to realize field-free SOT switching, we first need to induce an in-plane exchange bias in the structure. In this section, we show how such an exchange bias field can be experimentally characterized using the anomalous Hall effect.
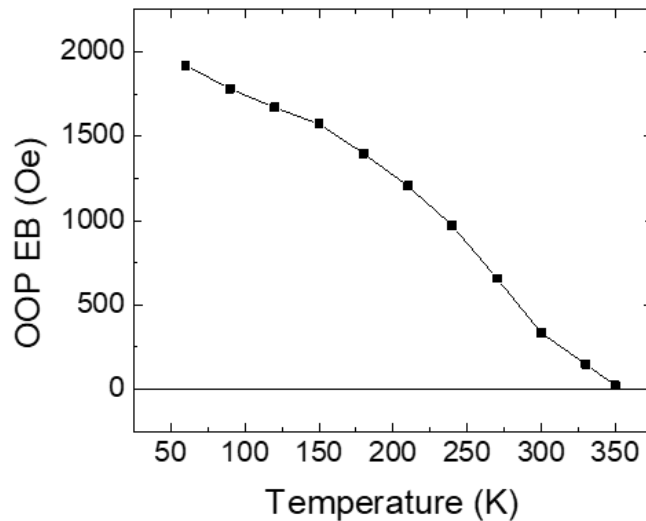
Figure 3.7. Characterization of the exchange bias blocking temperature. It is defined as the lowest temperature at which the exchange bias field goes to zero. Here we have used out-of-plane exchange bias (OOP EB) to extract the blocking temperature, which is around 360 K.

For inducing an in-plane exchange bias, the sample's temperature should be raised above the blocking temperature in the presence of a large in-plane magnetic field. The blocking temperature is defined as the lowest temperature at which the exchange bias disappears (*59*). In

32

order to extract the blocking temperature quantitatively, we measured the temperature-dependence of the out-of-plane exchange bias (see Figure 3.7). First, the sample was annealed with an out-of-plane field. Then, its temperature was reduced to 100 K in vacuum and in the presence of an out-of-plane field of 1 T. Subsequently, the out-of-plane EB was measured at different temperatures, up to 350 K, and by fitting the data the blocking temperature was found to be around 360 K.

The devices were annealed using current-induced Joule heating in the presence of a large in-plane magnetic field that could saturate the magnetization. In this technique, a DC current with proper amplitude is applied to the device, which is placed inside a magnetic field. The amplitude of the applied current is large enough to raise the sample's temperature above the blocking temperature, but not to burn the device. The appropriate amplitude was found experimentally for each CoFe thickness. The magnetic field was applied along the longitudinal $\hat{x}$ direction of the Hall bar; hence, a longitudinal exchange bias was obtained as shown in Figure 3.2 (b). For the sample with $t_{CoFe} = 1.1$ nm, 20 mA and 30 mA DC currents were applied, for the 10 μm and 20 μm Hall bar widths, respectively, which translates to a temperature of 400 K, according to the temperature-dependence of the resistance in the sample. This temperature is indeed higher than the blocking temperature. This amplitude resulted in the largest in-plane exchange bias without damaging the structure. The current was applied for 10 minutes in the presence of an external field of 1.5 T. Then the samples were cooled for 5 minutes in the air with the magnetic field on. The samples had the same total resistance change ΔR_{field}, measured by anomalous Hall effect, after this procedure, which suggests that the magnetic properties are not degraded.

In order to measure the in-plane exchange bias field, the anomalous Hall resistance was measured as a function of in-plane external field. The total magnetic energy can be expressed as

$$E = (-K_u + 2\pi M_s^2)\cos^2\theta - M_s(H_y \cos\varphi \sin\theta + H_x \sin\varphi \sin\theta + H_z \cos\theta), \qquad (3.7)$$

where K_u is the perpendicular magnetic anisotropy energy, M_s is the saturation magnetization, θ and φ are the polar and azimuthal angles of the magnetization, respectively, and H_y, H_x, and H_z are the transverse, longitudinal, and perpendicular magnetic field components, respectively, as illustrated in Figure 3.2 (b). It should be noted that here we are assuming that the magnetization remains uniform in the process. For in-plane exchange bias measurement, an external field in the longitudinal direction was applied; hence $\varphi = 90°$. Thus, the above equation can be rewritten as

$$E = (-K_u + 2\pi M_s^2)\cos^2\theta - M_s H_x' \sin\theta, \qquad (3.8)$$

where $H_x' = H_x + H_{EB}^{IP}$ should be used instead of H_L, to account for the in-plane exchange bias field. Here, we have assumed that the out-of-plane exchange bias is small and negligible, which can be confirmed by the out-of-plane AHE loop. For different values of external magnetic field, the total energy should be minimized with respect to θ, as a result

$$\frac{\partial E}{\partial \theta} = (-K_u + 2\pi M_s^2)(-\sin 2\theta) - M_s H_x' \cos\theta = 0. \qquad (3.9)$$

Since H_x' is small compared to the anisotropy field, then $\cos\theta = 0$ is not a physically valid solution. Thus,

$$\sin\theta = \frac{M_s H_x'}{2(K_u - 2\pi M_s^2)} = \alpha H_x', \qquad (3.10)$$

where $\alpha H'_x$ is very small, and α is a constant for each sample. The anomalous Hall resistance is proportional to the out-of-plane component of the magnetization, or $R_H \propto M_z = M \cos\theta = M\sqrt{1 - (\alpha H'_x)^2}$, which can be approximated near $\alpha H'_x = 0$ as $R_H \propto M \left(1 - \frac{\alpha^2 H'^2_x}{2}\right) = M(1 - \frac{\alpha^2}{2}(H_x + H^{IP}_{EB})^2)$. Consequently, in order to find the exchange bias field, R_H is measured at multiple in-plane magnetic fields around its extremum, then a quadratic function is fitted, and the extremum value is found. The extremum is where $H'_x = H_x + H^{IP}_{EB} = 0$, so the exchange bias field can be extracted. This is illustrated in Figure 3.8. Here, an in-plane exchange bias field has been introduced in two opposite directions, $\pm\hat{x}$, in a sample with t_{CoFe} = 1.1 nm. A small current of 0.5 mA amplitude was used to measure the anomalous Hall resistance, and the exchange bias fields were extracted using the method described above. In this measurement, the in-plane magnetic field was swept back and forth, and each point on the graph represents the average of the two values. The exchange bias magnitudes for the opposite directions were obtained from two different devices. However, these devices both have the same structure and are from the same film; thus, this small difference does not affect the validity of the arguments.

This method enables us to quantitatively measure the in-plane exchange bias at different stages in the process. Hence, we were able to do a comprehensive study on the Joule heating and training effects on the in-plane exchange bias and field-free switching. These will be discussed in more detail in following sections.
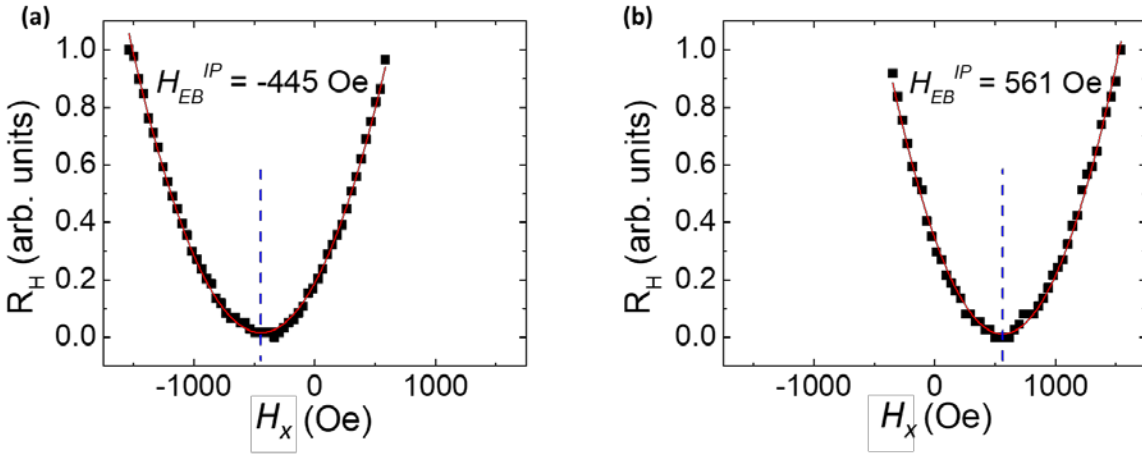
Figure 3.8. Characterization of the in-plane exchange bias field. The exchange bias has been induced in opposite directions in (a) and (b), $\pm\hat{x}$, by annealing the sample under two opposite magnetic fields. $H_{EB}{}^{IP}$ represents the in-plane exchange bias. t_{CoFe} = 1.1 nm in these devices. (*45*)

3.5   FIELD-FREE DETERMINISTIC SPIN-ORBIT TORQUE SWITCHING

After obtaining large in-plane exchange bias fields, field-free current-driven magnetization switching can be realized. Again, for SOT switching measurements a pulsed current is used to suppress the Joule heating effects. The results are depicted in Figure 3.9 (a) and (b), where field-free switching is observed as expected. The field-free switching polarity with positive (negative) exchange bias field is the same as that with positive (negative) external in-plane field, which indicates that the in-plane exchange bias indeed plays the role of the external field. Unlike Figure 3.6 (b), in this case $|\Delta R_{current}|$ is asymmetric with respect to different in-plane magnetic fields, H_L. We attribute this phenomenon to the presence of in-plane exchange bias, which has shifted the switching percentage diagram. Switching diagrams are plotted in Figure 3.9 (c) and (d). A clear shift in two different directions is observed, which is consistent with the exchange bias field directions for each case. As a result of these shifts, field-free switching is achieved. This can be described very well with the depicted switching diagrams; in these cases, $\Delta R_{current}$ is large at

36

zero field, but vanishes at some other in-plane field, where the exchange bias cancels the external field, and no switching is observed. In these switching diagrams, $\Delta R_{current}/\Delta R_{field}$ at zero field are around 50% and 90% of the maximum values, respectively. The maximum value of 0.81 is obtained for a 400 Oe in-plane field.
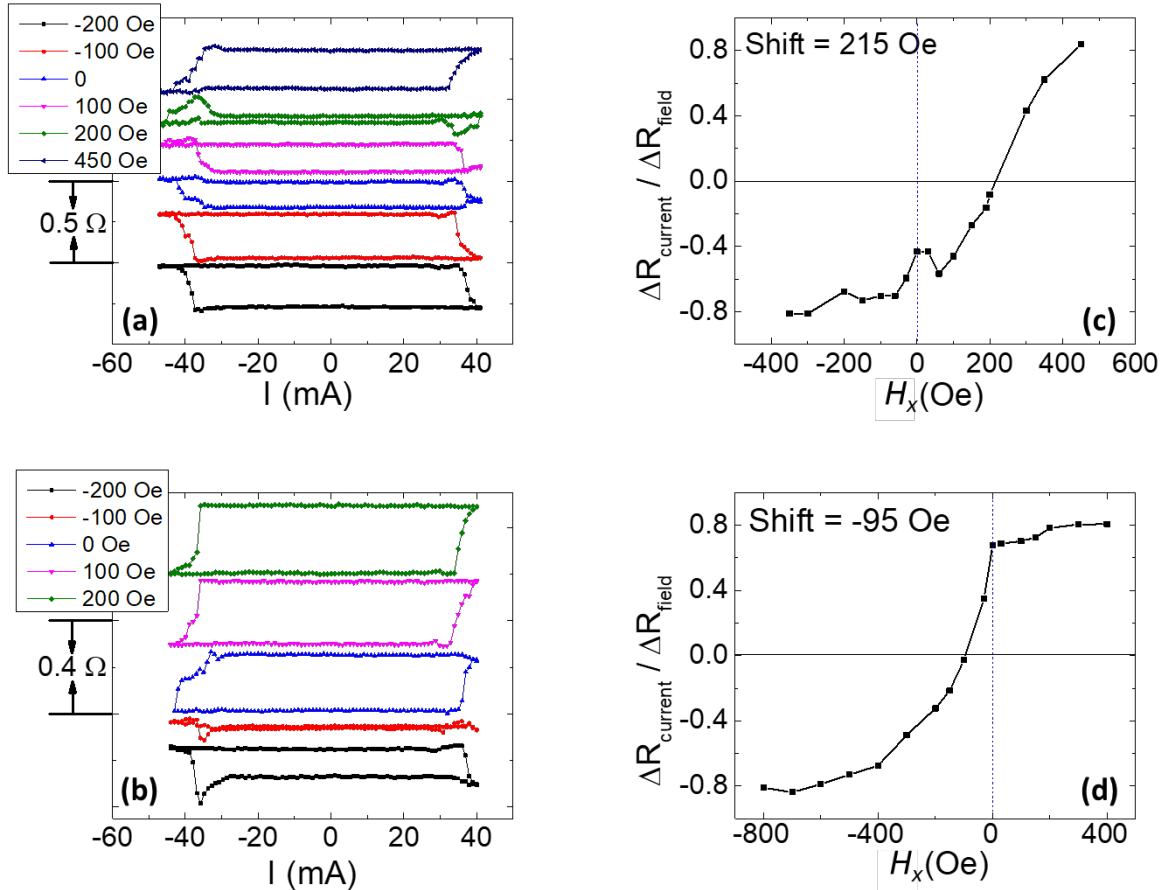
Figure 3.9. Deterministic field-free SOT switching with in-plane exchange bias. (a) and (b) show the SOT switching in two different devices with opposite directions of exchange bias fields, corresponding to Figure 3.8 (a) and (b). These measurements are done in the presence of different in-plane external fields, where the 0 Oe curves correspond to field-free switching. (c) and (d) show $\Delta R_{current}$/ ΔR_{field} (switching percentage) as a function of the applied external field, for devices shown in (a) and (b), respectively. (45)

It should be noted that in both cases, the shift in the switching diagram is smaller than the measured in-plane exchange bias field. This can be a result of the non-uniformity of the exchange

bias field throughout the device (*47*), or the in-plane exchange bias reduction because of Joule heating or exchange bias training effect (*60*). Furthermore, the amount of shift in Figure 3.9 (c) and (d) is not the same. This may again be due to Joule heating or exchange bias training effect, which can change the in-plane exchange bias during the measurement and consequently the observed shifts in the switching diagrams depend on the sequence in which the measurement was carried out.

In the next sections we will focus on explaining the role of Joule heating and exchange bias training effects in more detail.

3.6 JOULE HEATING EFFECT ON FIELD-FREE SOT SWITCHING WITH EXCHANGE BIAS

In order to limit the heating effects in the current driven switching measurements, pulsed currents was used. The critical current for switching is around 40-50 mA, depending on the device dimensions, which translates to a current density of ~4×10^7 A/cm^2 passing through the Pt layer. These relatively large currents can increase the sample's temperature through Joule heating. The IrMn thickness of the structure used in the measurements is 3 nm; thus, a low blocking temperature should be expected (*61*). Experimentally, we found the exchange bias blocking temperature to be around 360 K.

For a quantitative study of the Joule heating effects, we measured how the temperature of the sample changes in the switching measurement. To that end, we measured how the resistance of the sample changes during the time that the pulses are applied for switching. We also measured the temperature-dependence of resistance, in a range from 110 K to 350 K, and we extrapolated the resistance at higher temperatures. By comparing these two sets of data we were able to

estimate the temperature changes during switching. As can be seen in Figure 3.10, the temperature can rise to 500 K during the switching, which is well above the blocking temperature. This can result in an irreversible loss of the exchange bias.
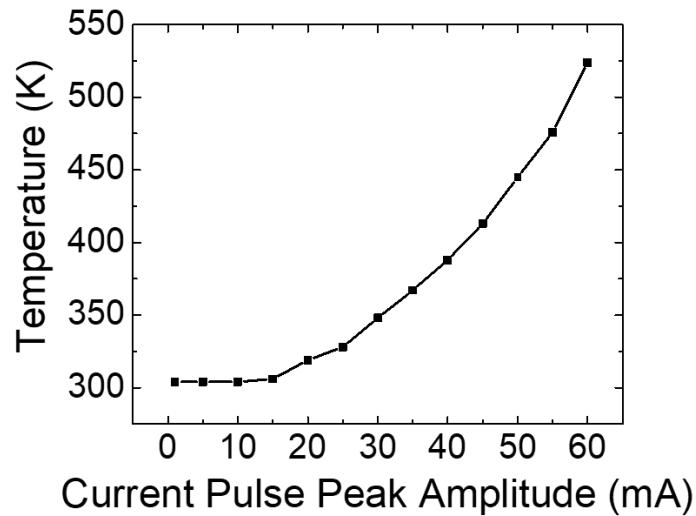
Figure 3.10. Sample's temperature rises during the SOT switching process. Temperature is calibrated by resistance. (*45*)

In order to show the importance of heating effects in these structures, we compare the field-free switching of a sample under pulsed and DC currents. For the DC current measurement, which is an extreme case in terms of Joule heating, the amplitude of the applied current changes from large negative values to large positive values, and back, with no delay between consecutive values. Each value is applied for around 200 ms.

For this purpose, a sample with $t_{CoFe} = 1.1$ nm was annealed using the current. An in-plane exchange bias field of 540 Oe was introduced in the sample. Then the sample was switched using DC current at zero external field. Afterwards, the annealing procedure was repeated to ensure that the in-plane EB field of 540 Oe is still present. This time the sample was switched at zero

external field using pulsed current. The results are shown in Figure 3.11. With pulsed current, field-free switching is achieved, while with DC current almost no change in Hall resistance (or equivalently in perpendicular magnetization) is observed. We attribute this effect to Joule heating, and its impact on the disappearance of the in-plane exchange bias, since the temperature of the sample rises above the blocking temperature during the measurement.
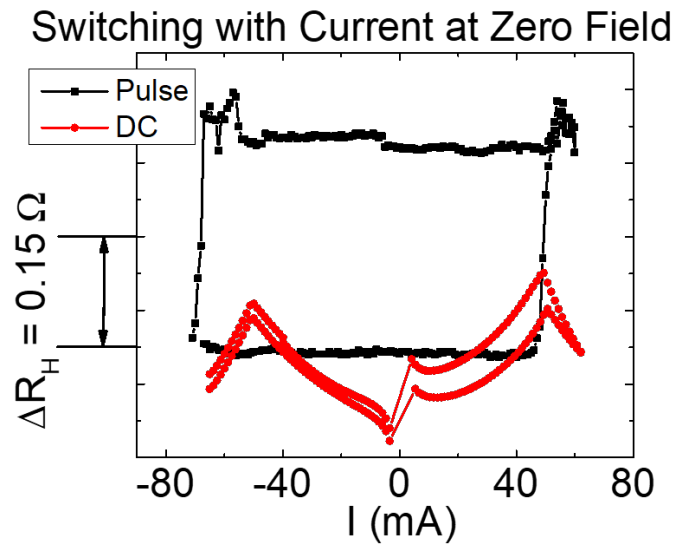
Figure 3.11. Comparison of field-free switching with DC and pulsed currents. Absence of switching in the DC case is attributed to significant Joule heating effect. (*45*)

Furthermore, even if pulsed current is used, the field-free switching still degrades after repeating the measurement several times. This can be seen in Figure 3.12. Here, the field-free switching measurement, of the same structure used above, is repeated 12 times. The total change in Hall resistance in the switching measurement is decreased, and the field-free switching is disappearing over time. This can again be attributed to the Joule heating effect. However, in this case the exchange bias training effect may also be a contributing factor, which will be discussed in the next section.

40
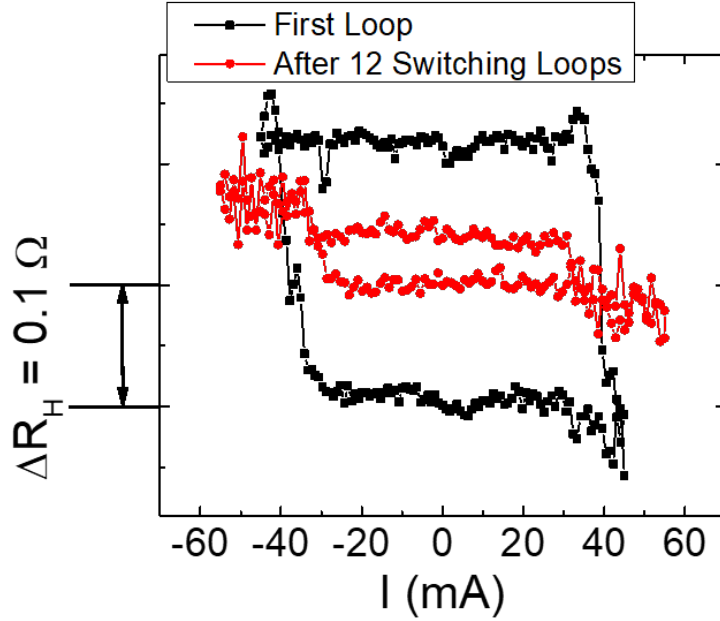
Figure 3.12. Field-free switching with exchange bias degrading after several switching cycles. The reason is that the exchange bias gradually decreases because of the Joule heating and exchange bias training effects. (*45*)

With the help of the device-level in-plane exchange bias measurement technique, it was observed that after each current-driven field-free switching cycle, the in-plane exchange bias was reduced, and eventually it disappeared, as depicted in Figure 3.13. As noted before, in the switching measurement, the temperature of the sample goes above the blocking temperature during the pulse application time. On the other hand, the relevant timescale τ for antiferromagnetic re-ordering is given by (*62, 63*)

$$\frac{1}{\tau} = \nu_0 \exp\left(-\frac{E_b}{k_B T}\right), \tag{3.11}$$

where $\nu_0 \approx 10^9$ Hz is the attempt frequency, E_b is the energy barrier for antiferromagnetic grain reversal, k_B is the Boltzmann's constant, and T is the temperature. For samples with several weeks of stability, τ is around 10^6 s at room temperature (T_0), which results in $E_b \approx$

$34.5 \times k_B T_0$. The temperature in our measurement goes as high as 500 K, so the corresponding timescale τ would be ~1 s, which is much longer than the pulse duration of 200 μs. Consequently, the exchange bias does not vanish with one large pulse, rather, it decreases gradually after many pulses. This can also explain why in the DC measurement no field-free switching is observed. In the DC measurement the high temperature is kept for much longer than 1 s; as a result, the exchange bias vanishes after the measurement, and no field-free switching is observed. It should be noted that the Joule heating of the 0.1 mA current, used for in-plane exchange bias measurement, was found to be negligible based on a control measurement. In the control measurement, the sample was not switched; only an in-plane field was applied to measure the in-plane exchange bias successively, and after 20 times there was no significant change in the exchange bias value. This shows that the heating effect of the 0.1 mA current can be neglected.
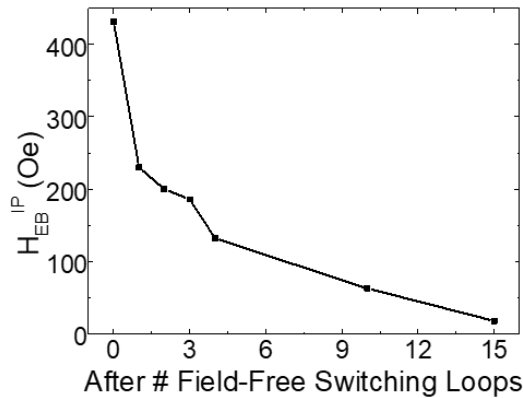
Figure 3.13. Loss of in-plane exchange bias ($H_{EB}{}^{IP}$) after several SOT switching loops. The exchange bias quickly drops to almost zero, only after 15 switching loops. (*45*)

The disappearance of the in-plane exchange bias as a result of heating can be further supported by the comparison of anomalous Hall data, R_H as a function of H_z, at different stages in the process: before and after current annealing with an in-plane field, and after the current-driven switching measurement, shown in Figure 3.14. After annealing in the presence of a large in-plane

magnetic field, the out-of-plane exchange bias decreases, which shows that the pinning is in the in-plane direction. Also, the coercivity is decreased by $\sim$100 Oe when the out-of-plane exchange bias decreases, which agrees with other reported findings (*64*). After annealing, current was used to switch the sample over twelve cycles, where the critical current for switching was around 45 mA. After the current-driven switching measurement, the out-of-plane exchange bias appears again, this time in the form of double loops. This further indicates the presence of heating effects. The temperature of the sample, with perpendicular easy axis, is raised above the blocking temperature during the switching measurement, in the absence of any large external fields. Consequently, the out-of-plane exchange bias tends to appear again, but there is no preference between upward and downward pinning directions, because both are along the easy axis and there is no external field to make a preference. Thus, some parts of the sample have an upward and the other parts have a downward pinning exchange bias, hence the double loop exchange bias appears.

One simple way for reducing the effect of Joule heating might be to enhance the blocking temperature by increasing the IrMn thickness. However, this is not a desirable approach, since it will also increase the shunting effect, and even more current will be required for SOT switching. The SOT for switching stems from the Pt layer, since with these thicknesses, Pt has a much lower resistance. By increasing the IrMn thickness, the shunting effect becomes significant and less current passes through Pt. Consequently, the critical current for switching increases. Samples with thicker IrMn layers up to 10 nm were tested, but field-free switching was not achieved in them.

The Joule heating effect is helpful when switching is assisted with an external in-plane field. In the same sample, using DC current reduces the critical current density for switching by 10% compared to the case where pulsed current is used. This is because Joule heating effect raises the temperature of the sample and reduces the anisotropy, and consequently switching becomes easier. On the other hand, when an in-plane exchange bias is used for field-free switching, the heating effect is no longer desirable since it reduces the in-plane exchange bias field. In this case avoiding the thermal effect is crucial.
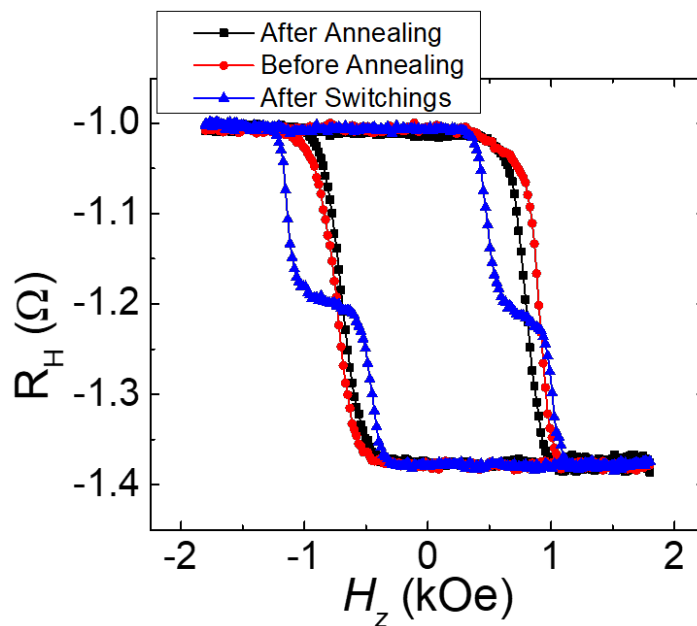
Figure 3.14. Comparison of the anomalous Hall data before annealing, after annealing, and after the SOT switching measurement. The appearance of double loops after SOT switching shows that the out-of-plane exchange bias appears again, but this time it is randomly distributed in up or down direction between different magnetic domains, hence the double loop appears. (*45*)

All these results show that the Joule heating effect can be a major obstacle for the practical application of field-free SOT switching using in-plane exchange bias. This problem might be mitigated to some extent if more thermally robust antiferromagnetic materials such as PtMn are

used, however, keeping an in-plane exchange bias in samples with intrinsic perpendicular magnetic anisotropy is fundamentally challenging.

3.7   EXCHANGE BIAS LOSS DUE TO TRAINING EFFECT

Even if very short pulses with negligible heating effects are used, the in-plane exchange bias will not be constant after successive switchings, due to the exchange bias training effect. The training has mostly been investigated in cases where an external magnetic field is used for cycling through hysteresis loops (*60, 65, 66*). However, it can also exist when SOT is used for magnetization switching. The spin structure at the antiferromagnet/ferromagnet interface deviates from its equilibrium state when an exchange bias field is created. Consecutive switchings can result in a rearrangement of the IrMn's spin structure at the interface of IrMn/CoFe towards an equilibrium state (*60*). Consequently, a gradual decrease in the in-plane exchange bias is expected. It should be noted that there are also some other models and explanations provided for the origin of exchange bias training effect (*66-71*). However, in this work we only focus on the general concept.

In order to show this effect in our structure, a sample with $t_{CoFe} = 1.1$ nm was current-annealed, with a resulting in-plane exchange bias field of 560 Oe. Then an out-of-plane external field was used to switch the sample back and forth. Afterwards, the in-plane exchange bias was measured and we repeated this cycle. The result is depicted in Figure 3.15. After each out-of-plane loop, the in-plane exchange bias is decreased, which can be attributed to training effect. In our case, SOT is used to switch the perpendicular magnetization. However, as described above, multiple switchings of the magnetization itself results in a reduction of the in-plane exchange bias. This can be a major problem for these devices, since the in-plane exchange bias is essential for field-

free switching. As shown in Figure 3.15, after only 20 successive switchings, the in-plane exchange bias is reduced by around 30%. This effect will deteriorate the device performance very fast over the time. By comparing the results of Figure 3.13 and Figure 3.15, it can be seen that in our measurements, the Joule heating effect is dominant over the exchange bias training effect in decreasing the in-plane exchange bias.
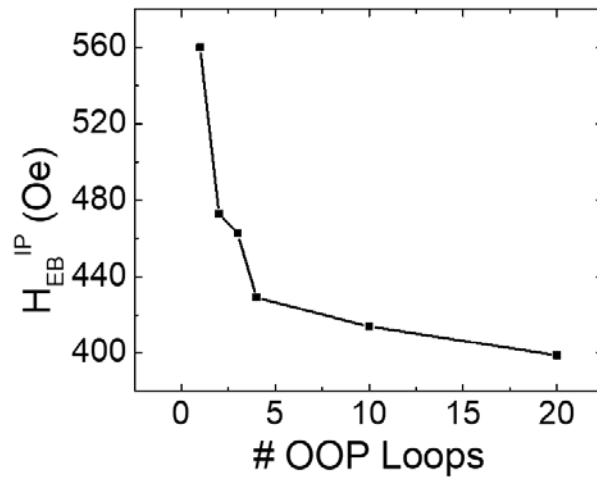
Figure 3.15. Exchange bias training effect. In-plane exchange bias (H_{EB}^{IP}) is reduced after several back-and-forth switching with an out-of-plane (OOP) field. (*45*)

Although deterministic field-free SOT switching can be realized using an in-plane exchange bias, but our results show that there are several important factors that needs to be taken into consideration. Most importantly, presence of multiple magnetic domains due to pinning centers enhanced by the exchange bias, Joule heating effect, and exchange bias training effect must be mitigated for the practical application of this strategy.

Another important aspect of SOT devices is that they should be compatible with magnetic tunnel junction (MTJ) geometry to allow for a high-ratio electrical readout based on the tunneling magnetoresistance (TMR) effect. In MTJ structures (shown in Figure 1.3 (c)), a free and a fixed

magnetic layers are separated by a relatively thin oxide tunneling barrier, where the total resistance of this trilayer depends on the relative orientation of the magnetizations. Thus, in order to enable TMR readout, the free magnetic layer should be placed next to the oxide tunneling barrier. We used Pt-CoFe-IrMn as a prototype to study the field-free switching with exchange bias, however, this structure is not compatible with MTJs, since the CoFe layer is not placed next to an oxide. That forms the motivation for studying the IrMn-CoFeB-MgO material system, explained in the following section.

3.8 FIELD-FREE SWITCHING IN IRMN-COFEB-MGO MATERIAL SYSTEM

In order to have field-free SOT switching in a structure compatible with the TMR readout in MTJs, one needs to place the ferromagnetic layer next to an oxide tunneling barrier. Among the known TMR stacks, CoFeB-MgO-CoFeB multilayer gives rise to the highest room-temperature TMR by far (*72, 73*). As a result, a practical SOT heterostructure should incorporate a CoFeB layer as a free magnet, placed adjacent to an MgO layer. MgO neither has atoms with high spin-orbit coupling, nor a magnetic order. So to realize field-free SOT switching with exchange bias in such a stack, both the exchange bias field and the SOTs should originate from a single layer placed on the bottom of CoFeB, i.e., we should use an antiferromagnetic material with a high spin-orbit coupling. IrMn is a special antiferromagnet in the sense that it contains the 5d heavy-metal Ir, which has a strong SOC. Consequently, we can update the Pt-CoFe-IrMn stack by removing the Pt layer, and still realize SOT switching. Considering all these aspects, we chose IrMn-CoFeB-MgO as a practical platform for studying field-free SOT switching (see Figure 3.16). We should also add that around the same time another work with a similar material stack and concept was published

(*49*). [Note: even in Pt-CoFe-IrMn we have the SOT from IrMn, however, because of the Pt's low resistance, much of the current passes through Pt and IrMn does not have a significant contribution to the SOTs.]
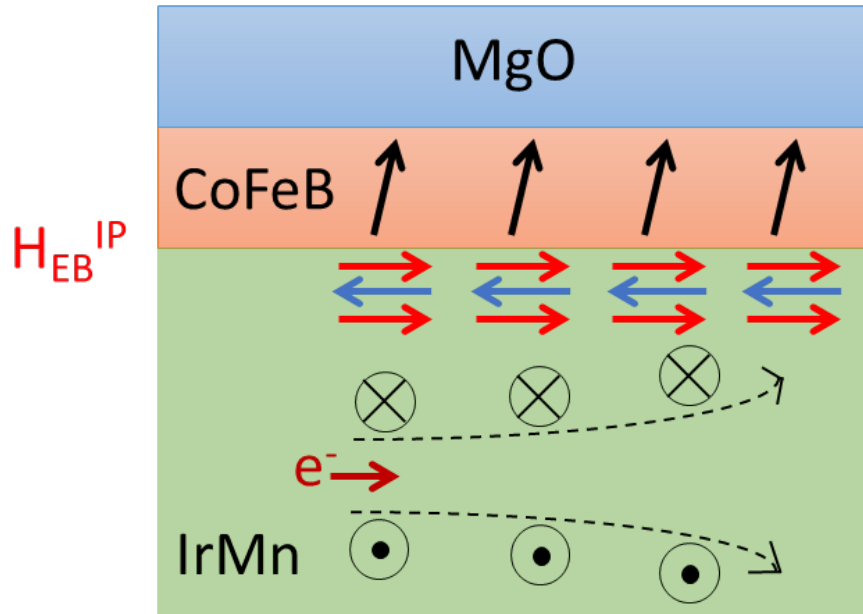
Figure 3.16. Schematics of field-free SOT switching with exchange bias in a structure that is compatible with MTJ integration. IrMn provides both the in-plane exchange bias (H_{EB}^{IP}) and the SOTs. The spin-dependent scattering inside IrMn represents the spin Hall effect process.

We first establish the presence of a sizable SOT from the antiferromagnet $Ir_{22}Mn_{78}$ (22% and 78% show the stoichiometric material composition). We again used the harmonics technique (*50-52*) to characterize the SOTs in IrMn-CoFeB-MgO material system (*74*), shown in Figure 3.17. We find that IrMn has a relatively large spin Hall angle of 0.057 ± 0.002, with the same sign as that of Pt, but opposite to that of Ta. We also found that the spin Hall angle in $Ir_{22}Mn_{78}$ is larger than the reported value for $Ir_{50}Mn_{50}$ (*75*).

After establishing the possibility of SOT switching with IrMn (*74*), we optimized the material stack to allow for the simultaneous presence of perpendicular magnetic anisotropy, sizable SOT, and an in-plane exchange bias field at room temperature.
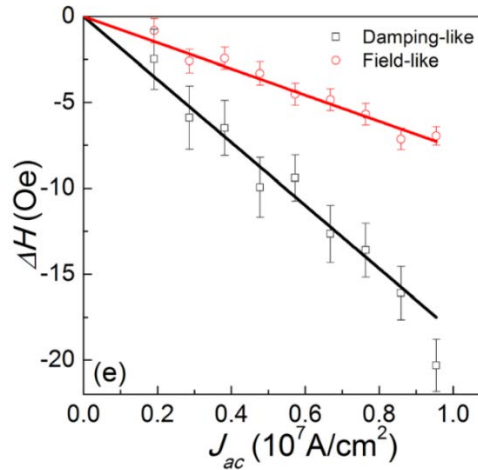
Figure 3.17. Spin-orbit torque effective fields in IrMn, characterized by the harmonics technique. Figure is taken from Ref. (*74*).

We deposited this optimized stack using magnetron sputtering on Si/SiO_2 substrates: Ta(2) / IrMn(5) / CoFeB(0.9) / MgO(2) / Ta(2) – numbers represent thicknesses in nm. The 2 nm Ta layers at the bottom and top are used as buffer and capping layers, respectively. In order to find the optimized thickness of IrMn there are some trade-offs to be considered. Exchange bias blocking temperature depends on the antiferromagnet's layer thickness in thin films. We found that for IrMn layers thinner than 5 nm, the blocking temperature is below the room temperature and hence not useful. This sets the lower bound on the IrMn thickness. On the other hand, in stacks with IrMn thicker than 5.5 nm, the CoFeB layer does not have perpendicular anisotropy, most probably because of an increased surface roughness. Hence, we also have an upper bound of 5.5 nm on IrMn thickness and we find the optimal IrMn thickness to be around 5 nm. For CoFeB layer, we need to optimize its thickness to obtain perpendicular anisotropy. The perpendicular

anisotropy has an interfacial origin, so we need to keep the CoFeB thickness small. But making it too small (less than 0.7 nm or so) would result in a non-continuous layer. On the other hand, we find that CoFeB thickness of more than 1.0 nm has an in-plane anisotropy and as a result, the optimized value is around 0.8-0.9 nm, where we chose 0.9 nm. For the MgO layer, optimizing the thickness is crucial for TMR stacks and typical values are around $1.5 - 2.0$ nm to allow for electron tunneling.

We characterized the exchange bias field and the perpendicular anisotropy in our optimized films using magneto-optical Kerr effect (MOKE). In the MOKE measurement, the signal is proportional to the perpendicular (z) component of the magnetization. The results are plotted in Figure 3.18. As can be seen, the exchange bias fields are around 20-30 Oe and around the same order as the coercive fields. We used a relatively low-temperature annealing at 150 °C for 30 minutes to reduce the elemental diffusion.
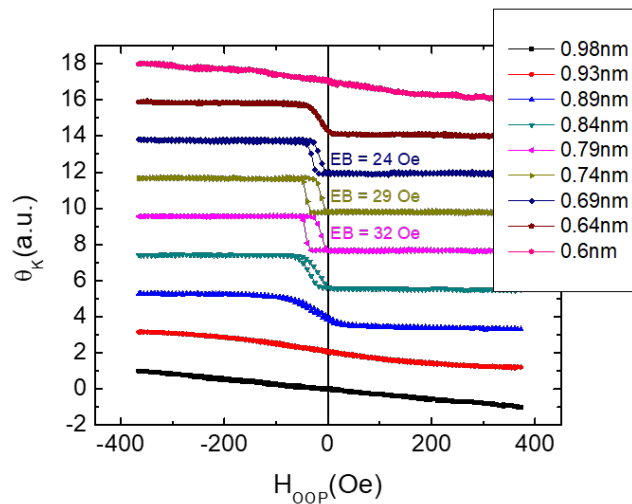
Figure 3.18. Characterization of perpendicular exchange bias (EB) field in IrMn(5) / CoFeB(t) / MgO(2) stack. θ_K shows the Kerr rotation, and different curves are for different CoFeB thicknesses.

With the induced in-plane exchange bias, we can realize field-free deterministic SOT switching in the optimized stack. The results are shown in Figure 3.19. We characterize the Hall resistance when an external out-of-plane field is used to switch the sample, as shown in Figure 3.19 (a). Then we use SOT to drive the switching and obtain the plot on Figure 3.19 (b). By observing the total anomalous Hall resistance change, we can see that the switching percentage is close to 35%, i.e., only 35% of the magnetic domains are switched, which is again a typical property of field-free switching using an in-plane exchange bias.
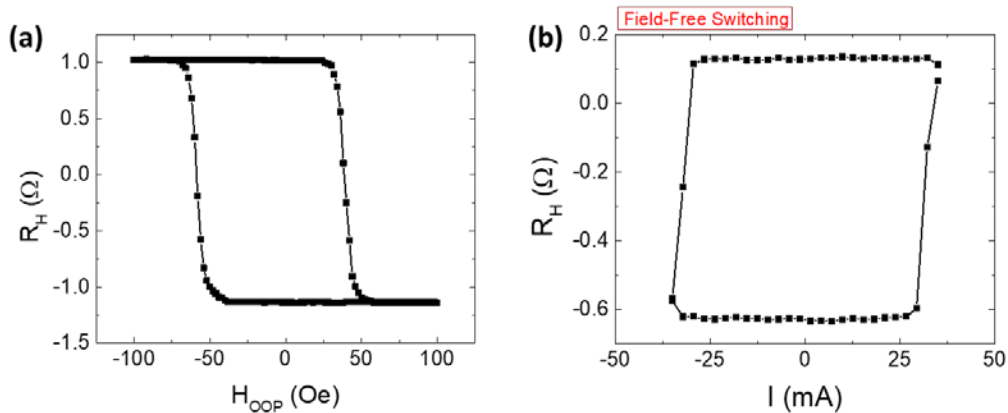
Figure 3.19. Field-free SOT switching in IrMn-CoFeB-MgO material system. (a) Anomalous Hall resistance as a function of the out-of-plane (z direction) magnetic field. (b) Field-free SOT switching, measured with anomalous Hall resistance as a function of the applied current peak through the sample.

Besides the field-free SOT switching, IrMn-CoFeB-MgO material system has several other interesting properties. Although we primarily developed this material system for SOT applications, but later on we found that the IrMn-CoFeB-MgO system exhibits several other interesting phenomena as well, such as the Dzyaloshinskii-Moriya interaction, voltage-control of magnetic anisotropy, and hosting magnetic skyrmions. In Chapter 5, we discuss these other interesting effects in the IrMn-CoFeB-MgO material system.

51

3.9 SUMMARY

The possibility of realizing field-free deterministic SOT switching was demonstrated using an in-plane exchange bias field created at an antiferromagnet-ferromagnet interface. We realized this concept in two material systems of Pt-CoFe-IrMn and IrMn-CoFeB-MgO, where the latter is compatible with integration in MTJ structures. In these systems, the exchange bias field plays the role of the in-plane external magnetic field and breaks the symmetry between up/down states for a deterministic switching.

However, there are several disadvantages and challenges associated with this approach. As was described in previous sections, the exchange bias field is very susceptible to the Joule heating effect. In these structures, the exchange bias is in the in-plane direction but the ferromagnet's easy axis is perpendicular to the film plane. As a result, when the sample is heated during the current-induced SOT switching, the relaxed interfacial spins will partly reorient to the out of plane direction. Furthermore, multiple magnetization reversals at the interface will also result in a reduced exchange bias field, which in turn results in the loss of field-free switching, through both Joule heating and exchange bias training effects. In these studies, we have used relatively long current pulses of 200 μs, but the heating effects could be reduced with shorter current pulses. However, we should also note that for shorter current pulses on the order of few nanoseconds or less, one needs to apply substantially larger current densities to the sample for achieving switching (*76*). Another strategy for decreasing the effect of heating might be to enhance the exchange bias blocking temperature. This can be done by increasing the antiferromagnet's thickness. The main tradeoff here is that an enhanced exchange bias field also increases the interfacial pinning. In other words, a large exchange bias will pin the ferromagnet's magnetization

52

in the in-plane direction, which will make the SOT switching harder and increases the required switching current density.

Another problem in using exchange bias field is that it has a non-uniform distribution across the device's area (*47*). As a result, not all the magnetic domains feel the same amount of effective in-plane field; some of the domains feel a strong field and some feel a very weak one. Consequently, when current-induced SOTs are used, only a portion of magnetic domains that feel a strong in-plane field are switched, resulting in the partial switching phenomena that is widely observed across all the works with the in-plane exchange bias (*77*). This problem can be mitigated to some extent if high-temperature annealing is used to make the grains with uniform exchange bias larger, however, we should note that a high-temperature annealing will also increase the elemental diffusions which is especially detrimental at the antiferromagnet-ferromagnet interfaces, where no diffusion barriers can be inserted. Using thermally robust antiferromagnets such as PtMn might mitigate this problem.

Furthermore, the MTJ-compatible structures of antiferromagnet-ferromagnet-oxide limit the SOT material choices to antiferromagnets exclusively, where there are only a few viable options such as PtMn or IrMn. But these materials do not possess high spin Hall angles, so the resulting switching current densities are relatively high.

We can see that there are many stack design tradeoffs that must be considered and studied for obtaining field-free deterministic SOT switching with an in-plane exchange bias. Some of these tradeoffs impose very hard requirements for applications, which may make this approach impractical. It would be desirable to have a deterministic switching mechanism that does not rely

on fragile effects such as the exchange bias field, and one that is compatible with different material systems. This is the motivation behind the next presented approach for field-free switching, explained in detail in the next chapter.

4 DETERMINISTIC SPIN-ORBIT TORQUE SWITCHING USING STRUCTURAL ASYMMETRIES

4.1 MOTIVATION AND BACKGROUND

The problem of deterministic SOT switching of perpendicular magnetization is rooted in the fact that in conventional sputter-deposited SOT heterostructures, the current-induced net spin polarization lies in the in-plane direction. The reason is that in such structures, the inversion symmetry is broken only in the perpendicular direction (z axis), consequently, applying an in-plane current along the x axis can only create a net spin polarization in y direction (based on the symmetry arguments presented in Chapters 1 and 2). But can we have a partly perpendicular spin polarization upon the application of an in-plane current? One way of achieving this goal is to use certain high-SOC crystals that lack an in-plane inversion symmetry along the y axis. In this case, a partly perpendicular net spin polarization is allowed by symmetry arguments. This strategy has been employed in experiments, where use of WTe$_2$ as a SOT layer results in the creation of a net perpendicular spin polarization (*78*). However, use of single-crystal structures with specific symmetries is not practical for memory applications in the industry.

One can also break the in-plane inversion symmetry using the sputtering process and allow for deterministic SOT switching. This idea was first explored in 2014 (*37*), even before the use of crystals lacking in-plane inversion symmetry. In that work, the oxide layer is sputter-deposited in a wedge shape, by oblique angle deposition without substrate rotation. As a result, an asymmetric structure is obtained in the lateral direction relative to the in-plane current, and out-

55

of-plane effective magnetic fields are created which allow for field-free SOT switching (as explained in the last part of Chapter 2). The work presented in this chapter follows the same physics, however, we expand on the earlier work and modify it for practical applications. We modify the conventional SOT heterostructure by inserting a slightly asymmetric light-metal at the heavy-metal/ferromagnet interface. The light-metal layer is deposited at an oblique angle by stopping the substrate rotation and thus breaks the structural symmetry. The broken symmetry enables the creation of current-induced out-of-plane effective magnetic fields (H_z^{eff}), whose direction only depends on the current polarity. Consequently, H_z^{eff} breaks the symmetry between the up and down states for each current polarity and allows for deterministic SOT switching at zero external magnetic field.

Although structural symmetry breaking has been explored in previous works (*37, 79*), but the underlying physics were not understood very well. Furthermore, in those works, a large gradient of magnetic anisotropies was observed, which makes them impractical for applications. Here, we show that the creation of H_z^{eff} can potentially be explained by the Rashba-Edelstein effect, where the effective built-in electric field in our samples is slightly tilted away from the perpendicular direction. We also demonstrate that the magnetic anisotropy and switching current density in our samples is almost independent of the light-metal insertion thickness, which mostly originates from the fact that light-metals have a very low spin-orbit coupling (noting that the magnetic anisotropy depends on spin-orbit coupling, refer to Appendix A.2). Furthermore, we study the scalability of our approach and realize field-free SOT switching in device sizes ranging from 20 μm down to 300 nm. Most of the data in this chapter is published in Ref. (*80*).

4.2   Spin-Orbit Torques in Laterally Asymmetric Structures

In conventional SOT heterostructures with uniform heavy-metal/ferromagnet/oxide layers, structural symmetry is broken along the growth direction, which we denote as the z axis. Following Eqs. 2.5 and 2.6, the broken symmetry along z axis allows for the creation of a perpendicular built-in electric field ($\boldsymbol{E_{bi}}$) and SOTs, which consist of a field-like (FL) term and a damping-like (DL) term, proportional to $\gamma H_y^{FL}\boldsymbol{m} \times \hat{\boldsymbol{y}}$ and $\gamma H_x^{DL}\boldsymbol{m} \times \boldsymbol{m} \times \hat{\boldsymbol{y}}$, respectively (*37*). Here, $\boldsymbol{m}$ denotes the unit vector of magnetization, γ is the gyromagnetic ratio, and $\hat{\boldsymbol{y}}$ is the in-plane direction perpendicular to the current axis ($\hat{\boldsymbol{x}}$). The creation of these SOTs can be attributed to the spin Hall effect (*22-24*) or interfacial Rashba-Edelstein effect (*28, 29*). We modify this conventional SOT structure by inserting a slightly asymmetric light-metal at the heavy-metal/ferromagnet interface, as shown in Figure 4.1 (a).
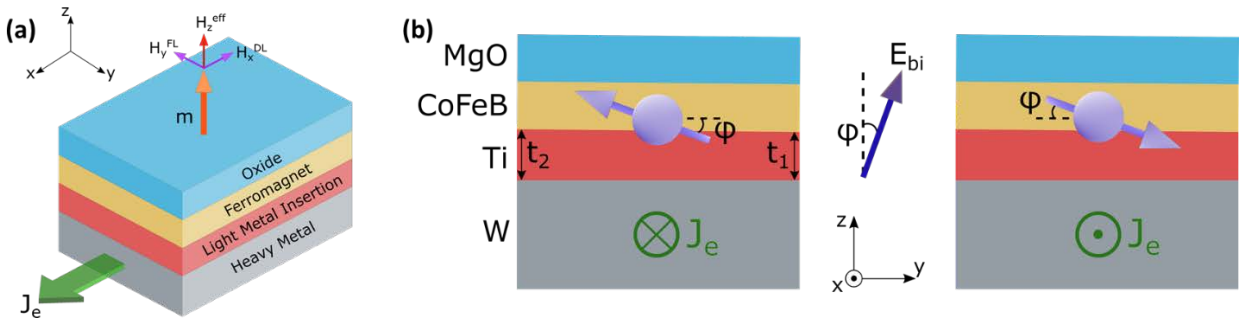
Figure 4.1. Creation of out-of-plane current-induced effective magnetic fields (H_z^{eff}) by inserting a slightly asymmetric light-metal layer. (a) Schematics of the studied SOT structure. H_x^{DL}, H_y^{FL}, and H_z^{eff} denote the damping-like, field-like, and effective out-of-plane magnetic fields, respectively. J_e denotes the charge current and m is the unit vector of magnetization. The light-metal layer is slightly asymmetric and allows for the creation of H_z^{eff}. **B**, Creation of a net out-of-plane spin polarization and effective magnetic field in the studied W/Ti/CoFeB/MgO heterostructure. The Ti layer is slightly asymmetric, hence two different thicknesses t_1 and t_2. The broken symmetry along y and z axes results in an effective electric field, E_{bi}, tilted by angle φ from the z-axis. Based on the structures symmetries, the spin polarization can have components along both y and z axes, where the z-axis component gives rise to H_z^{eff}, whose direction changes upon reversing the charge current direction. (*80*)

This light-metal layer (Ti) is deposited at an oblique angle with respect to the substrate surface (along y axis) without rotating the substrate, so it is grown in a tilted direction away from the substrate normal (see Figure 4.2). Consequently, it breaks the mirror symmetry with respect to the x-z plane and allows for the creation of a built-in effective electric field along the y axis. We should note that in practice, the thickness of the light metal insertion layer changes very slightly, i.e., we do not need a large thickness gradient. In this modified stack, the structural symmetry is broken along both z and y axes, so in principle, the total built-in effective electric field E_{bi} has components along both of these axes as shown in Figure 4.1 (b).
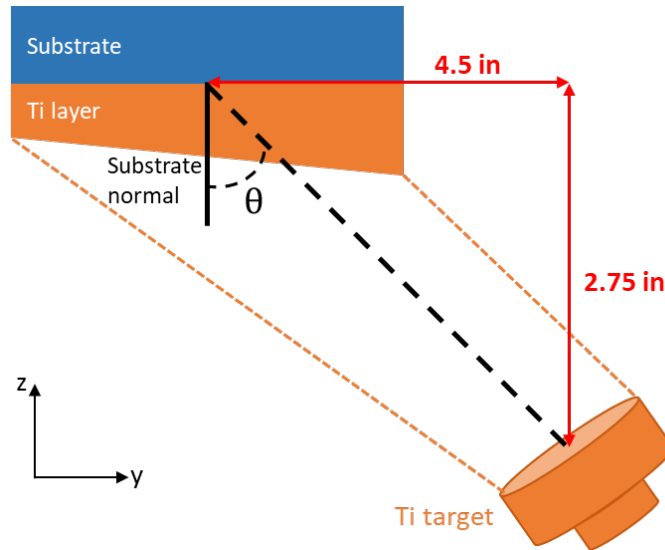
Figure 4.2. Ti deposition at an oblique angle. Ti layer is deposited at an oblique angle by stopping the substrate rotation. Consequently, the effective growth direction is tilted by angle θ with respect to the substrate normal direction. The dimensions correspond to the actual dimensions of our sputtering chamber. (*80*)

Following the symmetry arguments of Chapter 2, here we have a structure with reduced symmetry, so we no longer must impose the symmetry of SOT effective fields under reflection in the x-z plane. This in turn allows for the emergence of two additional terms, $H_z^{FL}\hat{\boldsymbol{z}}$ and $H_z^{DL}\boldsymbol{m} \times \hat{\boldsymbol{z}}$ (*37*), both of which transform as pseudo-vectors under reflection in the y-z plane.

Microscopically, we can see the emergence of these new fields by looking at the Rashba effect as an example. According to the Rashba spin-orbit coupling, the effective Hamiltonian can be modelled as $H_R = \frac{\alpha_R}{\hbar} \boldsymbol{\sigma}.(\boldsymbol{E} \times \boldsymbol{p})$ (*28, 29, 81*), where α_R, $\hbar$, $\boldsymbol{\sigma}$, $\boldsymbol{E}$, $\boldsymbol{p}$ denote the Rashba parameter, reduced Plank constant, Pauli matrices, effective electric field, and electron momentum, respectively. Although a nonzero equilibrium macroscopic electric field along the y-axis is forbidden within a metallic system, but atomic-scale effective electric fields can still exist in such systems, where they average to zero on scales longer than the screening length. Consequently, such microscopic effective electric fields can give rise to an out-of-plane spin-polarization based on the microscopic Rashba Hamiltonian (*82*). With a charge current applied along the x axis $\boldsymbol{p} \parallel \hat{\boldsymbol{x}}$, and $\boldsymbol{E_{bi}}$ having both y and z components, we can see that two effective magnetic fields along the y and z axes can be created, resulting in a net spin-polarization along these axes, as shown in Figure 4.1 (b). The y-component of this effective magnetic field is absorbed into effective fields of SOTs terms and the z-component is shown by H_z^{eff} in Figure 4.1 (a). We can also see that by reversing the charge current direction, the direction of the effective magnetic field and spin-polarization should be reversed. Consequently, each current polarity has a determined H_z^{eff} direction. This current-induced magnetic field can then be used to break the symmetry between up and down magnetization states for each current polarity, and enable deterministic SOT switching without any external magnetic fields.

4.3 MATERIALS AND EXPERIMENTAL SETUP

All the materials in these samples are deposited on a thermally oxidized Si/SiO_2 substrate by magnetron sputtering using an AJA International Physical Vapor Deposition System at room

temperature. The metal and MgO layers are deposited using dc and rf power sources, respectively. The Ti layer was deposited at an oblique angle without rotating the sample, yielding a continuous gradient of thickness along the length of the sample. It should be noted that there is a 2 nm Ta buffer layer under W, and a 2 nm Ta capping layer on top of the MgO layer in all these samples. We also carried out cross-sectional high-resolution transmission electron microscopy (HRTEM) imaging on a representative sample, shown in Figure 4.3, with the help of our collaborators at Chinese Academy of Sciences (*80*). We can see that Ti and CoFeB layers are continuous and flat in nm scales, despite their very small thicknesses. We also see that the interfaces are flat and sharp.
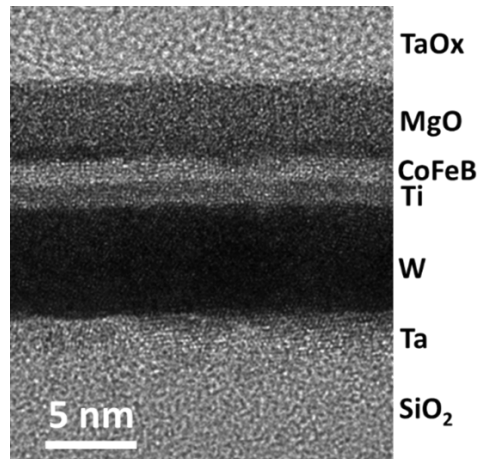
Figure 4.3. HRTEM image of a representative Ta(2.0) / W(5.0) / Ti(~1.0) / CoFeB(0.9) / MgO(2) / TaOx(2) sample (nominal thicknesses in nm). (*80*)

For micrometer-size devices (20 × 130 μm^2), the films were patterned into arrays of Hall bars by standard photolithography and dry-etching techniques. The smaller Hall bar devices with widths of 1 μm, 500 nm, and 300 nm were fabricated by e-beam lithography and dry etching techniques with HSQ/PMMA double-layer resist, by our collaborators in Chinese Academy of Sciences, Institute of Physics. The measurements were carried out using a Keithley 2612 dual source-meter,

a Keithley 6221 current source, and Stanford Research Systems SR830 lock-in amplifiers. The external magnetic field was generated by an electromagnet driven by a Kepco power supply. All measurements are carried out at room temperature.
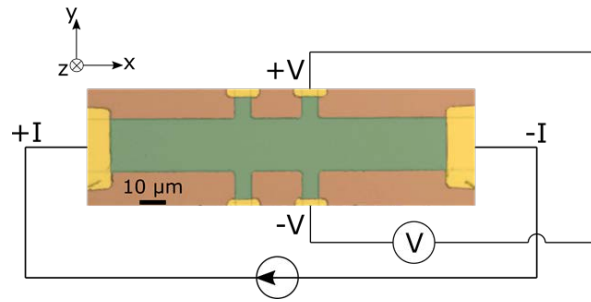
Figure 4.4. Micrometer Hall bar structure and the measurement configuration. The Ti thickness is slightly asymmetric along the y axis. I and V show the applied current and measured Hall voltage, respectively. (80)

Experiments were carried out on the core structure consisting of a W(5.0)/Ti(t)/CoFeB(0.9)/MgO(2) stack (thicknesses in nm), in which all the layers were deposited by the magnetron sputtering method. Here W is the heavy-metal layer that provides a large spin-orbit coupling, Ti is the light-metal insertion, CoFeB is the ferromagnet, and MgO is the oxide which can be used as a tunneling barrier in a magnetic tunnel junction. The Ti layer has a wedged shape, where its thickness slightly and linearly changes by 0.17 nm per cm of the sample length (from 0.48 to 1.32 nm). This gradient translates to a thickness difference of around 3.5 nm over an 8-inch wafer (note that magnetic tunnel junctions usually have a total thickness of around 40 nm (83)). The films were then patterned into an array of micrometer or nanometer Hall bars (see Figure 4.4), where the Ti thickness changes along the y direction, breaking the mirror symmetry with respect to the x-z plane. The small thickness gradient means that the Ti layer is essentially uniform over each of the studied Hall bars. Nevertheless, sputtering at the oblique angle by

61

stopping the substrate rotation breaks the symmetry along the y-axis, which can be understood as an effective tilted growth direction towards the y-axis (see Figure 4.2). Consequently, the creation of H_z^{eff} is expected upon the application of a charge current along the x-axis. We should also note that beside the Rashba effect, a possible tilted crystal texture in Ti (or CoFeB) might also contribute to the creation of H_z^{eff}, similar to the effect observed in WTe$_2$ (*78*). The perpendicular magnetic anisotropy and the coercivity of the sample at different Ti thicknesses are studied using the magneto-optical Kerr effect as shown in Figure 4.5, where a constant coercivity throughout the whole length of the sample is observed. This uniformity is in contrast to the previous works with structural asymmetry (*37, 79*), and the key reason is that Ti is a light-metal with a very small spin-orbit coupling, so its thickness does not affect the magnetic anisotropy or coercivity much.
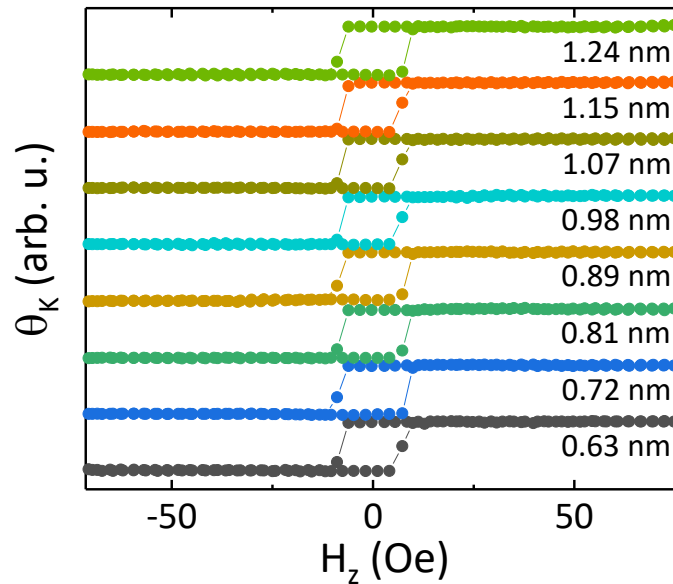
Figure 4.5. Perpendicular magnetic anisotropy and coercivity of the sample at different nominal Ti thicknesses measured by magneto-optical Kerr effect. Here, θ_K denotes the Kerr rotation which is

proportional to the z-component of magnetization, and H_z is the applied perpendicular magnetic field. The coercivity of the sample is almost independent of the Ti insertion thickness. (*80*)

4.4   CHARACTERIZATION OF OUT-OF-PLANE EFFECTIVE MAGNETIC FIELDS

In order to characterize current-induced out-of-plane effective magnetic fields (H_z^{eff}), we performed anomalous Hall effect (AHE) measurements on the Hall bar structures with the current applied along the x-axis. The hysteresis loops are shifted from zero external field to two opposite directions for opposite current polarities (see Figure 4.6 (a)). The value of these shifts for each current density corresponds to the opposite of current-induced effective magnetic field H_z^{eff}.
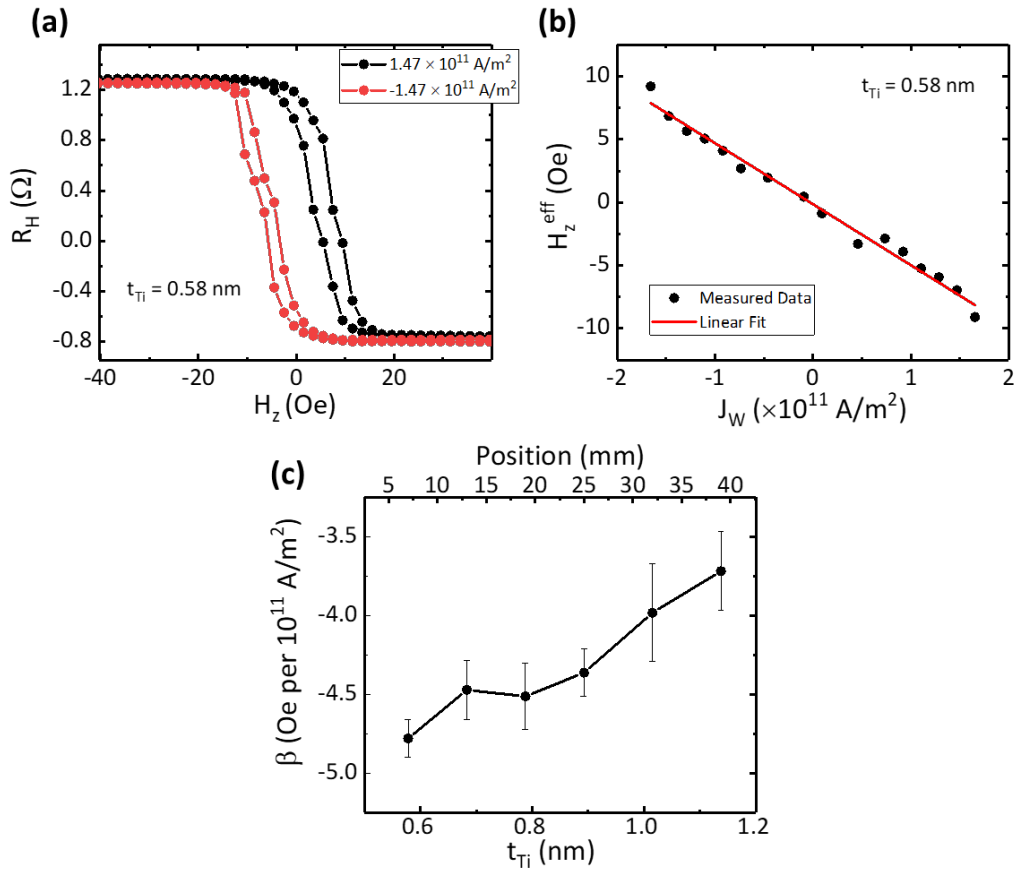
Figure 4.6. Out-of-plane current-induced effective magnetic fields measured using anomalous Hall effect. (a) Out-of-plane hysteresis loops are shifted to opposite directions for opposite current polarities. Here, R_H and H_z denote the anomalous Hall resistance and applied perpendicular magnetic field, respectively. The estimated current densities are for the W layer, and the Ti thickness in this device is 0.58 nm. (b) Current-induced out-of-plane effective magnetic fields as a function of applied current density, where a

linear relationship is observed. The slope of this plot is denoted by β. J_W is the current density through the W layer. (c) The slopes β plotted as a function of Ti thickness and the device positions on the sample. The error bars originate from averaging three different devices as well as the linear fitting errors. The negative sign of β shows that for a current applied in $+\hat{x}$, H_z^{eff} points to $-\hat{z}$. (80)

Furthermore, we observe a linear relationship between H_z^{eff} and the applied current densities as shown in Figure 4.6 (b), consistent with the analysis discussed earlier. The slope of this linear relationship is denoted by β, which is plotted for devices with different Ti thicknesses in Figure 4.6 (c). We note that $|\beta|$ decreases gradually with increasing the Ti insertion thickness, which can be attributed to the gradual change of the growth direction towards normal angle; at the thicker side of the sample, the angle in which the sputtering target views the sample surface is closer to the normal (see Figure 4.2), which means that the effective electric field $\boldsymbol{E_{bi}}$ is less tilted from the z-axis. However, the exact relationship between the slopes β and the Ti insertion thickness also depends on the details of interfacial properties and requires further study. Although $|\beta|$ decreases slightly with the Ti thickness, but we will show later that this change in $|\beta|$ does not affect the switching properties between different devices and a nearly uniform switching current density is obtained everywhere.
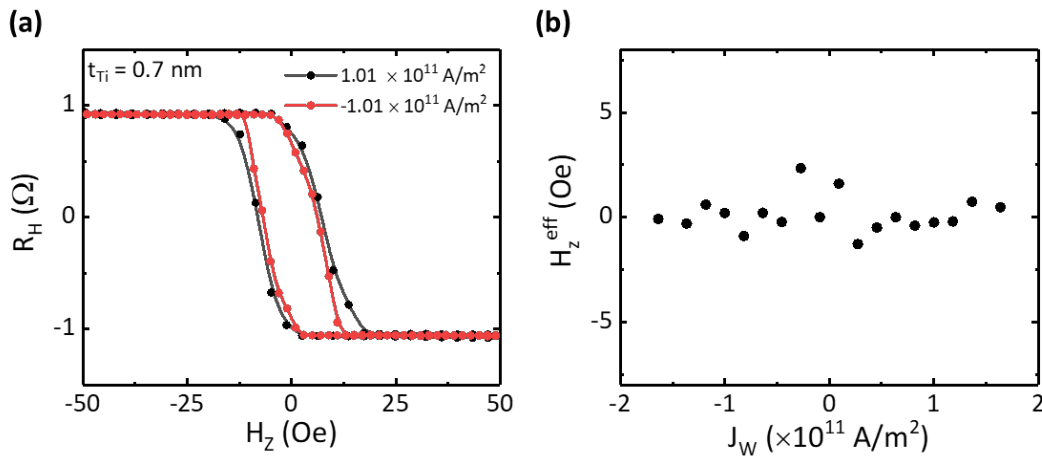
Figure 4.7. Absence of H_z^{eff} in samples with uniform Ti thickness. (a) Out-of-plane hysteresis loops characterized by anomalous Hall resistance (R_H) under different polarities of applied current. H_z represents

Furthermore, to verify the importance of the symmetry breaking along the y-axis, we performed additional experiments with similar structures but with a uniform Ti layer. We grew a uniform film with the core stack of W(5.0) / Ti(0.7) / CoFeB(0.9) / MgO(2.0), where numbers show the thicknesses in nm. In this film, all the layers have uniform thicknesses. Without a symmetry breaking along the y-axis, no perpendicular effective magnetic field H_z^{eff} is created, and consequently, the anomalous Hall hysteresis loops are not shifted from the center, even when large current densities on the order of 2×10^{11} A/m^2 are applied to the devices (see Figure 4.7). This observation further emphasizes the importance of symmetry breaking for inducing H_z^{eff} and realizing deterministic SOT switching.

In addition to the loop shifts method presented in Figure 4.6, we also quantified the H_z^{eff} and β values in our samples using a second-harmonic method where a large magnetic field is applied in y direction. Here we examine the induction of H_z^{FL} (which we show is equal to H_z^{eff}) and H_z^{DL} even when the sample is forced to have a single-domain magnetization under a strong applied field, larger than the anisotropy field. We follow the discussion presented in the supplementary of Ref. (*37*).

For the measurements, we use two lock-in amplifiers to simultaneously obtain first- and second-harmonic voltages. We apply a magnetic field larger than the anisotropy field (which is around 4-5 kOe) to ensure single-domain behavior. To extract H_z^{FL} and H_z^{DL}, we set the direction of the magnetic field to be along the y-axis (the wedge direction). In this case, the normalized second-harmonic voltage reads

$$\frac{V_{2\omega}}{V_{AH}} = -\frac{1}{2}\left[\frac{H_z^{FL}}{H_{ap} - H_K} + \frac{R_P(H_z^{DL} + B)}{R_{AH}H_{ap}}\right], \tag{4.1}$$

where V_{AH} is the first-harmonic anomalous Hall voltage, and B is a constant (following the discussion provided in the supplementary of Ref. (37)). Here, R_P and R_{AH} are the planar and anomalous Hall resistances, respectively. The $\frac{R_p}{R_{AH}}$ ratio in the studied devices is around 0.12, consequently, the contribution of H_z^{DL} to the second-harmonic voltage is much smaller than H_z^{FL} and can be ignored. Besides, $\frac{1}{H_{ap}-H_K} > \frac{1}{H_{ap}}$ when $H_{ap} > H_K$. However, we should note that in principle, both of these effective fields are present in our samples.

By fitting the second-harmonic voltage at large magnetic fields applied along y-axis, we can extract the out-of-plane components of spin-orbit fields. Figure 4.8 (a) and (b) shows the first- and second-harmonic voltages, with the external field applied in y direction. Here, an AC current at 173.333 Hz frequency is applied to the device (with 0.9 nm of Ti insertion) with a peak amplitude of 5 mA. By fitting the second-harmonic voltage above 4 kOe according to Eq. 4.1, we find a very good linear relationship between $\frac{V_{2\omega}}{V_{AH}}$ and $\frac{1}{H_{ap}-H_K}$ as shown in Figure 4.8 (c). Similar results were obtained for higher current amplitudes (measured up to 10 mA peak amplitude). After extracting the slope, we find H_z^{FL} per current density (or β) to be -4.2 Oe per 10^{11} A/m^2, which is in good agreement with the one extracted from the loop shifts method (-4.4 Oe per 10^{11} A/m^2). Similarly, for another device with 1.13 nm of Ti insertion, we find -3.4 Oe per 10^{11} A/m^2, which is again in good agreement with the loop shifts method result (-3.7 Oe per 10^{11} A/m^2).
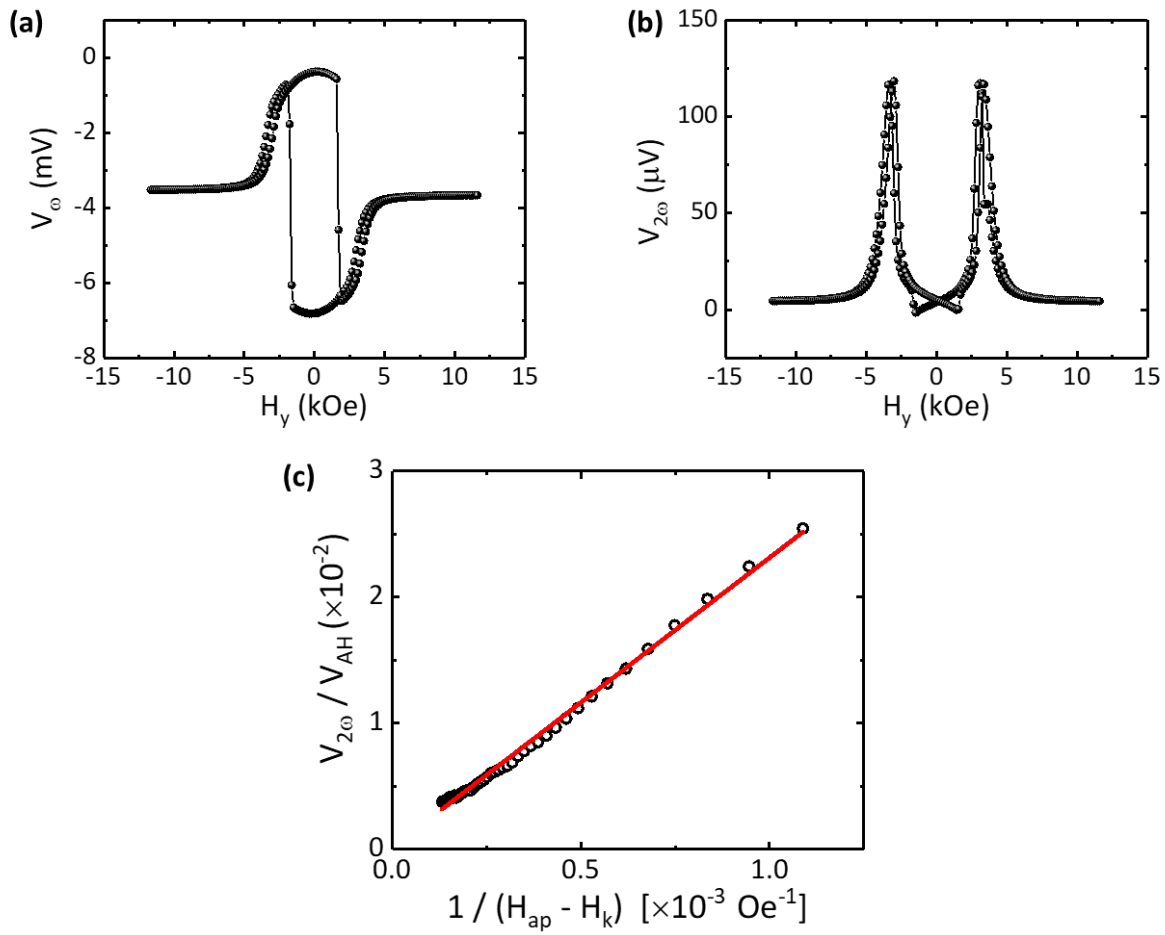
Figure 4.8. Quantifying H_z^{eff} (or H_z^{FL}) with the harmonics method. (a) First-harmonic voltage for a sample with Ti insertion of 0.9 nm under an AC current with 5 mA peak amplitude and at 173.333 Hz frequency. (b) Second-harmonic voltage. (c) Normalized second-harmonic voltage at large magnetic fields ($H_{ap} > H_K$). The slope yields H_z^{FL} according to Eq. 4.1. (*80*)

These results unambiguously show the presence of out-of-plane effective fields in our samples, probed by two methods: the harmonics and loop shifts methods. Since the harmonics data is obtained at very large magnetic fields (larger than the anisotropy field), it shows that these effective fields are induced even for the case of single-domain magnetization dynamics, hence ruling out the preferential domain nucleation mechanism (*84*). We can also rule out the role of tilted anisotropy for field-free switching (*85*), since these results show the presence of spin-orbit fields H_z^{eff} even when the magnet is saturated along the y axis.

4.5   Deterministic Spin-Orbit Torque Switching by a Light-Metal Insertion

With the help of current-induced H_z^{eff}, we can realize deterministic SOT switching without the need of any external magnetic fields as shown in Figure 4.9 (a). For each current polarity, H_z^{eff} breaks the symmetry of SOTs for the up/down states and sets the switching destination. For a positive current (applied in $+\hat{x}$), H_z^{eff} points towards $-\hat{z}$, so the down state is preferred, as shown in the 0 Oe curve of Figure 4.9 (a) (note that the state with higher resistance in our sample corresponds to the down magnetization state, $-\hat{z}$). Changing the current polarity reverses all these directions, i.e., a negative current prefers the up state. Upon applying a small 20 Oe in-plane magnetic field parallel/anti-parallel to the current, the switching polarity changes, showing that at these non-zero magnetic fields the switching is determined by the external magnetic field.

We also studied the repeatability of SOT switching at zero field by applying successive positive/negative current pulses to the sample (see Figure 4.9 (b)), which shows the stability of our approach against current-induced Joule heating. With each current pulse, the magnetization is fully switched between the up/down states, and the switching does not degrade over time, in stark contrast to the case with an in-plane exchange bias. It should be noted that the data in Figure 4.9 is obtained with current pulses of 1 ms duration.
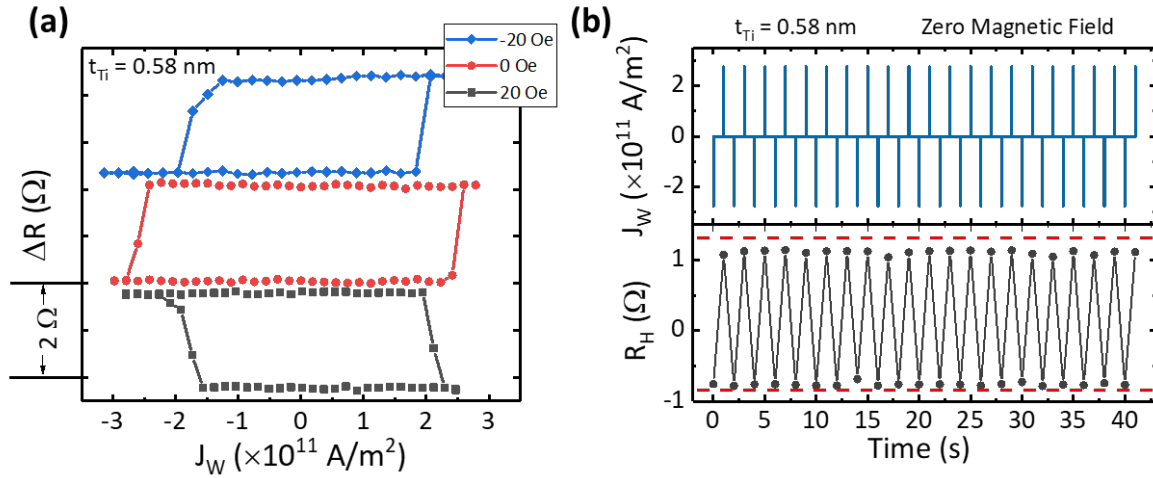
Figure 4.9. Deterministic spin-orbit torque switching without the need of any external magnetic fields. (a) SOT switching under different in-plane magnetic fields. ΔR is the change of anomalous Hall resistance, and J_W is the current density through the W layer. (b) Repeatable SOT switching at zero field with successive positive/negative current pulses with a 1 ms duration at a period of 1 s. The red dashed lines represent the highest and lowest achievable anomalous Hall resistances with an external perpendicular magnetic field. (*80*)

We performed the field-free SOT switching process with other current pulse widths as well, ranging from 5 ms down to 10 ns. In these measurements, a switching pulse with a certain duration is applied to the sample, and then after a 200 ms wait, a second low-amplitude pulse is applied to read the Hall resistance. The wait time between successive switching pulses is 1 second. Figure 4.10 (a) shows the field-free switching loop for a pulse width of 1 ms as an example. Here, the switching current density (J_{SW}) is defined as the required current density for switching the sample half-way, averaged for both positive and negative values. We expect the switching current density to increase as smaller current pulse widths are used. The reason is that for smaller current pulse widths, the Joule heating effect is smaller, and the sample's temperature undergoes a smaller raise. As a result, the anisotropy drops only slightly, and we need to apply more angular momentum and current to switch the sample. The switching current density dependence on the applied current pulse width is plotted in Figure 4.10 (b).
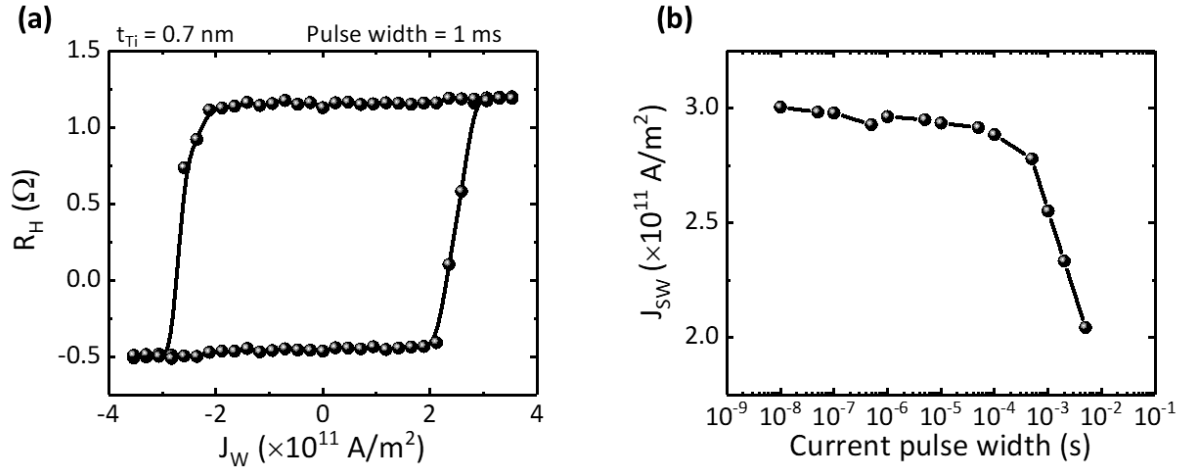
Figure 4.10. Field-free SOT switching dependence on current pulse widths. (a) Field-free SOT switching for a device with Ti insertion thickness of 0.7 nm and a pulse width of 1 ms at a 1 s period. (b) Extracted switching current densities for field-free SOT switching of the same device with different pulse widths down to 10 ns. (*80*)

We also studied the switching process using polar magneto-optical Kerr effect (MOKE) imaging technique, where we observed that field-free SOT switching happens via domain wall nucleation and propagation (see Figure 4.11). First the magnetization of the sample is initialized in the +z direction (corresponding to a low Hall resistance state). Then by applying 1-ms current pulses of positive and increasing amplitude (according to Figure 4.9 (a)), we can see that first the domains walls are nucleated and then they propagate until the whole area of the sample switches to a -z magnetization state. Similar results are obtained for the magnetization switching in the opposite direction. This result shows that the magnetization switching in our samples does not have a single-domain characteristic, which is expected because of the relatively large size of our samples. We can expect the same switching behavior persists until the device sizes are shrunk into single-domain limits. Although the switching process we observe is via domain wall nucleation and propagation, but as was shown earlier, we expect H_z^{eff} to be created even in the single-domain limit.

70
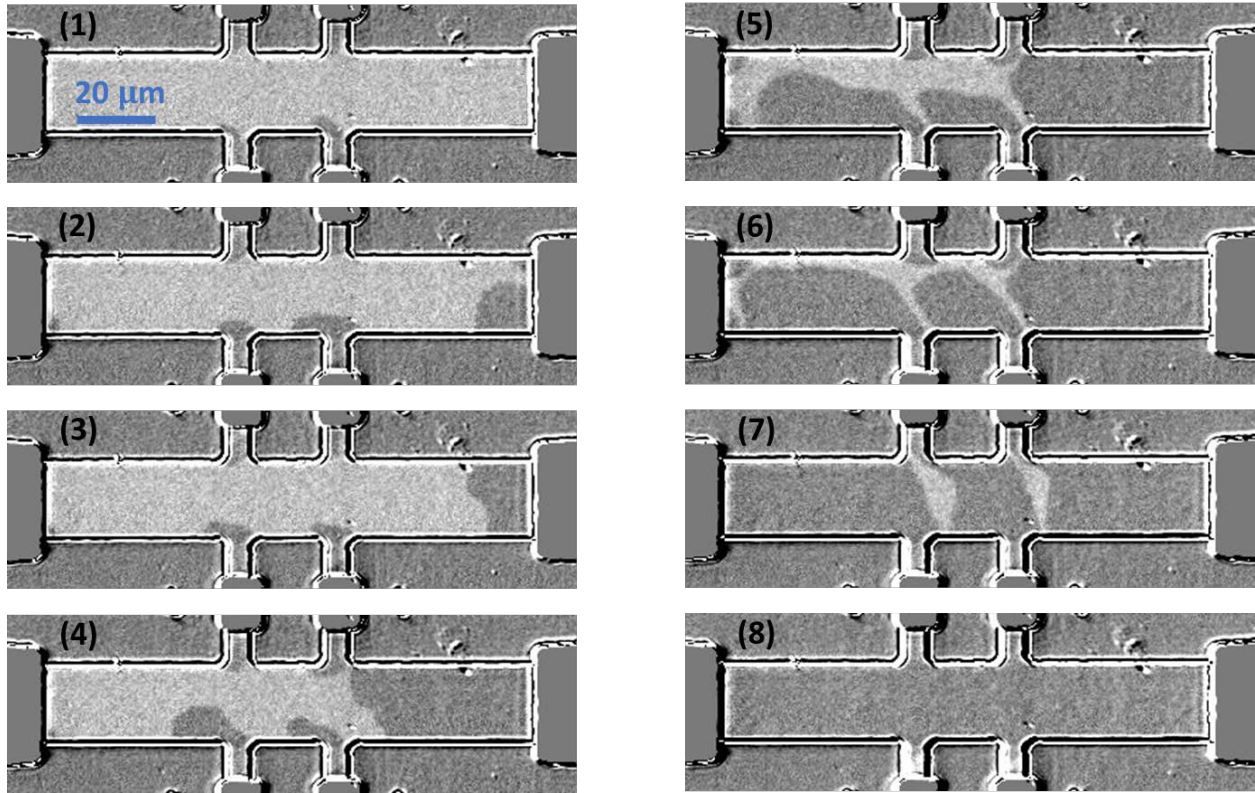
Figure 4.11. MOKE imaging of the field-free switching process. Bright (dark) areas correspond to a +z (-z) magnetization state. Snapshots 1-8 are taken in chronological order. The Ti insertion thickness in this device is 0.7 nm, and the wedge and current directions are perpendicular to one another. (*80*)

The main problem with previous works on lateral structural asymmetry was that very large gradients in magnetic/switching properties were observed in them (*37, 79*). The reason is that in those works, the wedged layer was one of the main layers in the SOT heterostructure, i.e., one of the heavy-metal, ferromagnet or oxide layers were asymmetric. But we know that these layers have all significant contributions to the magnetic properties, ranging from magnetization saturation and anisotropy to spin-orbit torques. As a result, the magnetic/switching properties had a strong dependence on the wedge layer insertion thickness and the device's position on the sample, making them impractical for wafer scale applications. However, here we are using a thin Ti layer, a light-metal, as an insertion layer. Hence, the magnetic/switching properties are not modulated much. We have quantitatively studied the uniformity of these properties. The

switching current density in our devices is almost independent of the Ti insertion thickness, as shown in Figure 4.12. As mentioned above, a sizable H_z^{eff} breaks the symmetry between the up/down states; however, small variations of its magnitude does not affect the switching current density much. Consequently, uniform magnetic anisotropy and a sizable β at all Ti thicknesses result in the nearly uniform switching performance, which is crucial for practical applications.
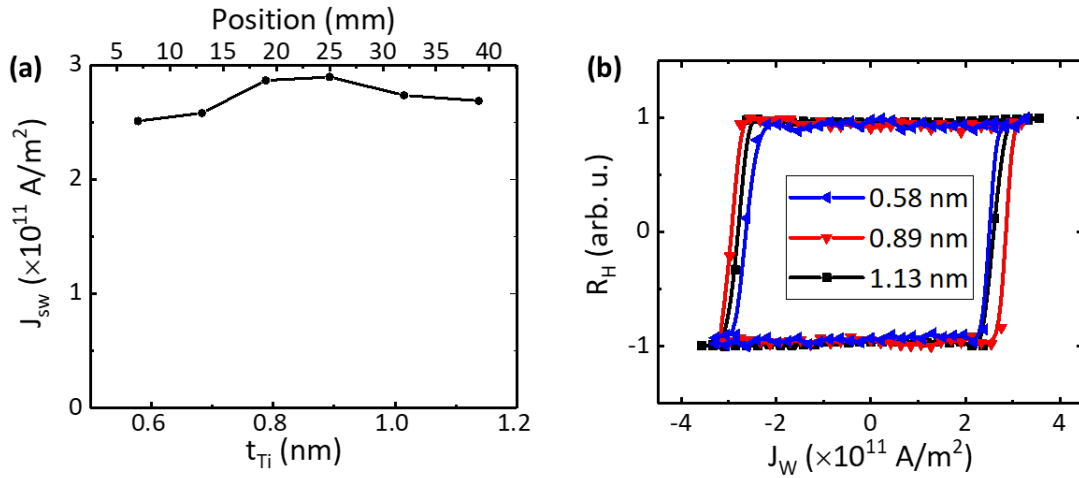
Figure 4.12. Uniformity of switching current density, despite the asymmetry of the Ti insertion layer. (a) Switching current density for devices with different Ti thicknesses on different positions of the sample. The switching current density (J_{SW}) is calculated as the average of the positive and negative switching currents through the W layer. (b) The corresponding SOT switching loops of devices with different Ti thicknesses characterized by anomalous Hall resistance (R_H). (*80*)

4.6 SCALABILITY OF FIELD-FREE SOT SWITCHING WITH LATERAL STRUCTURAL ASYMMETRY

One of the important aspects of using wedge-shaped layers in field-free SOT switching is their scalability, which had not been addressed in any of the previous experimental works. As was mentioned earlier, in these devices, the wedge layer has a very small thickness gradient (e.g., here the Ti layer has a nominal thickness gradient of 0.17 nm per cm of the sample length). When the films are patterned into Hall bar devices, the wedge layer's thickness difference across the two edges of the Hall bar is virtually zero (for a 20 μm wide Hall bar, the nominal Ti thickness

difference is less than 1 pm). This thickness difference scales linearly with the device dimensions, so for devices with tens of nm width, the nominal thickness difference is less than 1 fm. For such small thickness differences, it was not clear if an effective structural asymmetry persists in scaled devices. Furthermore, the relationship between the total thickness difference across the device and H_z^{eff} had not been studied. Here, we have addressed these questions by studying the induction of H_z^{eff} and subsequent field-free SOT switching by changing the Hall bars dimensions by two orders of magnitude.
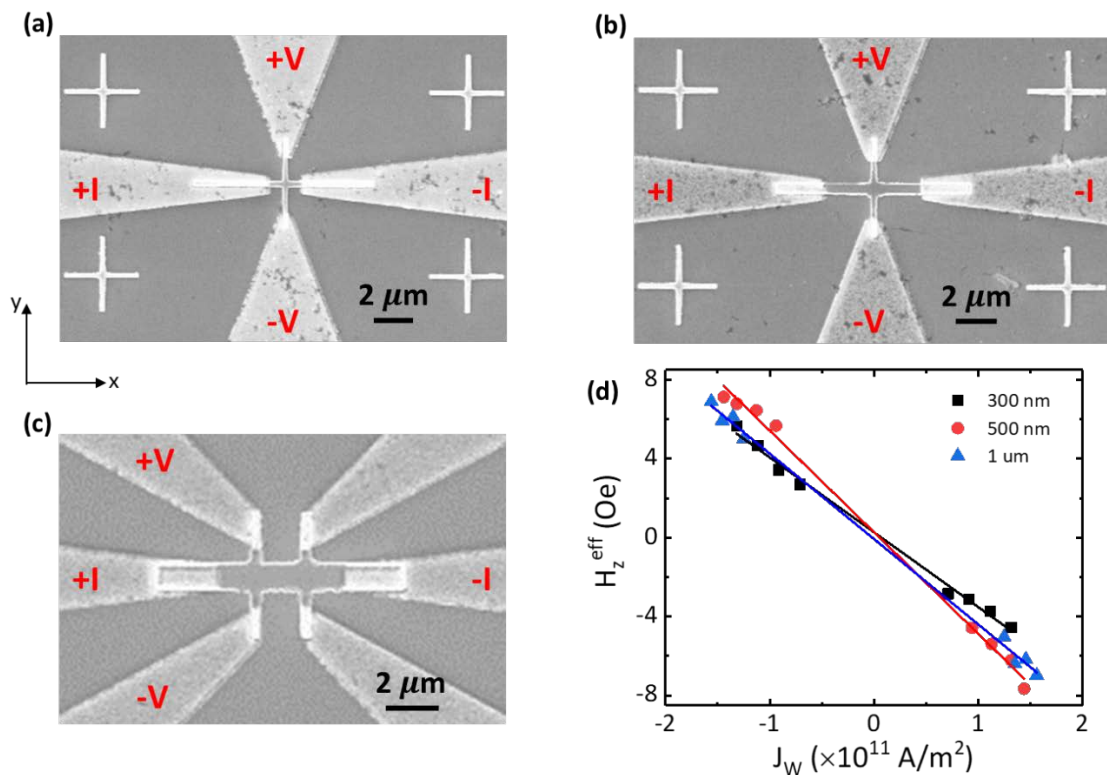
Figure 4.13. Scaled Hall bar devices and characterization of β values. Images of nano-scale Hall bar devices with widths of (a) 300 nm, (b) 500 nm, and (c) 1 μm, obtained using scanning electron microscopy (SEM). The current and voltage connection configurations for transport measurements are shown by I and V. (d) H_z^{eff} versus applied current density for devices with different Hall bar widths. The solid lines are the linear fittings to the data points. (*80*)

We observe both the presence of H_z^{eff} and SOT switching at zero external field in scaled devices down to nanometer sizes. We studied these effects in Hall bar devices with a variety of widths (1 μm, 500 nm and 300 nm), which were fabricated by our collaborators at the Institute of Physics, Chinese Academy of Sciences (see Figure 4.13) (*80*). We characterized β values in these devices by measuring H_z^{eff} as a function of applied current density (Figure 4.13 (d)), which shows that the β values obtained are nearly independent of device size.
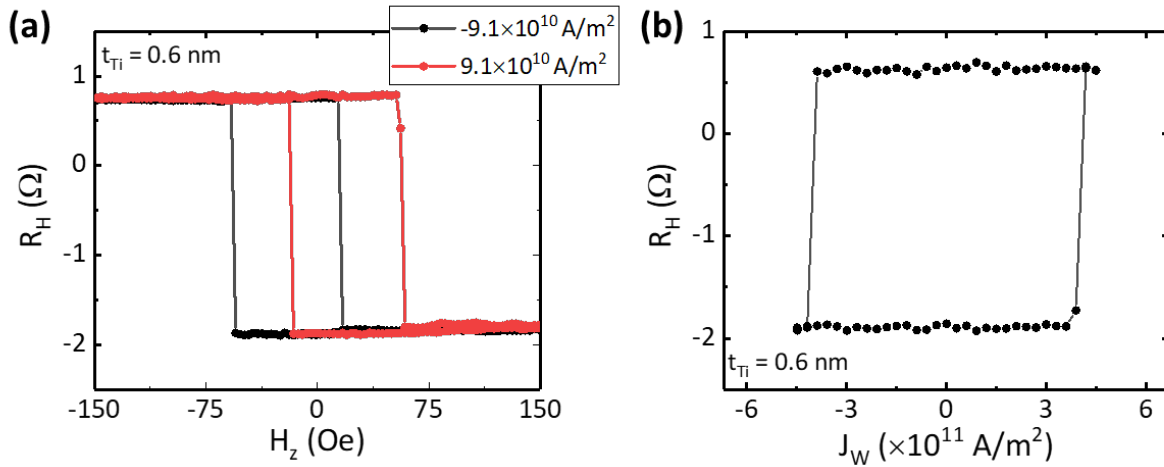
Figure 4.14. Scaling of field-free SOT switching down to 100s of nm device sizes. (a) Current-induced out-of-plane effective magnetic fields H_z^{eff} characterized with anomalous Hall effect in 500 nm wide Hall bars. Hysteresis loops are shifted to opposite directions upon changing the current polarity. In this device, the Ti thickness is 0.6 nm. R_H and H_z denote the anomalous Hall resistance and applied perpendicular field, respectively. (b) Deterministic SOT switching at zero external magnetic field for the same device. J_W shows the current density through W layer. (*80*)

As shown in Figure 4.14 (a), H_z^{eff} is created upon the application of in-plane current, manifested in the shift of hysteresis loops for two opposite current polarities. The current-induced perpendicular effective magnetic fields enable complete deterministic SOT switching at zero external field as well (see Figure 4.14 (b)). Here, we can observe a complete SOT switching of all the domains. We also compare the β value in devices with different widths, as shown in Table 4.1. We observe that the β value, which characterizes the strength of H_z^{eff} per unit current

74

density, is almost independent of the device sizes. Therefore, our approach for field-free switching remains applicable as devices are scaled to small dimensions, at least as long as the switching proceeds via domain-wall nucleation and propagation.

Hall Bar Width	$|\beta|$ (Oe per 10^{11} A/m^2)
20 μm	4.75
1 μm	4.59
500 nm	5.27
300 nm	4.13

Table 4.1. Scaling of perpendicular effective magnetic fields. We observe that β, which characterizes the strengths of H_z^{eff} per unit current density, is almost independent of the device size and is sizable down to nm scales. (*80*)

The nearly constant values of β for devices with different sizes suggests that the Ti thickness difference between the two edges of devices is not the reason for broken symmetry along the y axis. Instead, the symmetry breaking happens because of a more global property of our films, the Ti deposition at an oblique angle, which tilts the growth direction away from the z axis. This point in addition to Rashba-Edelstein effect can potentially explain why H_z^{eff} is present even for devices with virtually constant layer thicknesses. It can also explain why this approach is scalable: symmetry breaking is globally present in the film, hence, it does not depend on the device dimensions. It can be expected that by reducing the Ti layer thickness slope, one can still realize H_z^{eff} and deterministic SOT switching with a much lower thickness difference on large wafers.

75

However, the details of the relationship between H_z^{eff} and Ti thickness slope at the atomic scale needs further studies.

4.7 UNIFORM MAGNETIC PROPERTIES DESPITE THE ASYMMETRY OF THE LIGHT METAL INSERTION

In contrast to previous works on laterally asymmetric structures (*37, 79*), in our samples the magnetic anisotropy and coercivity are almost uniform and they do not change much with the Ti insertion thickness. In particular, previous works have found a very close correlation between the magnetic anisotropy gradient and the β values (*37, 79*), however, in our samples the anisotropy is almost constant with Ti thickness as shown in Figure 4.15.
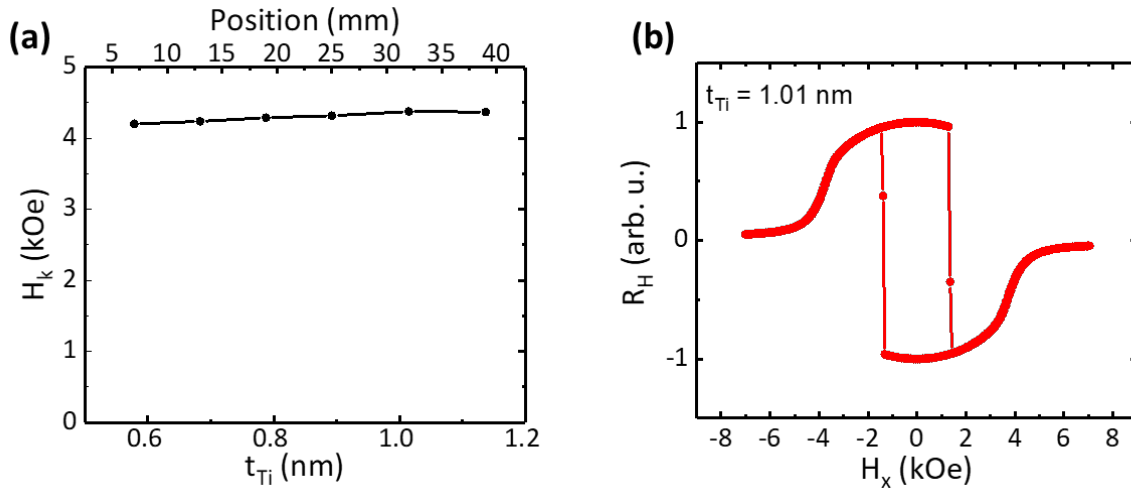
Figure 4.15. Uniform magnetic anisotropy and spin-orbit torques. (a) Effective perpendicular magnetic anisotropy field (H_k) as a function of Ti thickness/position of the devices. The anisotropy changes by around 5% with the different Ti thicknesses studied. (b) Anomalous Hall measurement carried out for extracting H_k fields, with anomalous Hall resistance (R_H) plotted versus an external in-plane magnetic field. H_k is defined as the point where the normalized in-plane component of magnetization $m_x = \sqrt{1 - m_z^2}$ reaches 0.98. It should be noted that R_H is linearly proportional to m_z. (*80*)

This suggests that the anisotropy gradient cannot explain the creation of out-of-plane magnetic fields H_z^{eff} in a generic asymmetric structure. We believe that the uniformity of magnetic anisotropy in our samples also originates from the fact that Ti has a very small spin-orbit coupling.

In order to quantitatively extract the effective anisotropy fields, we scanned the hard-axis hysteresis loop by applying an in-plane magnetic field to the sample until the magnetization is saturated along its hard axis (see Figure 4.15 (b)).
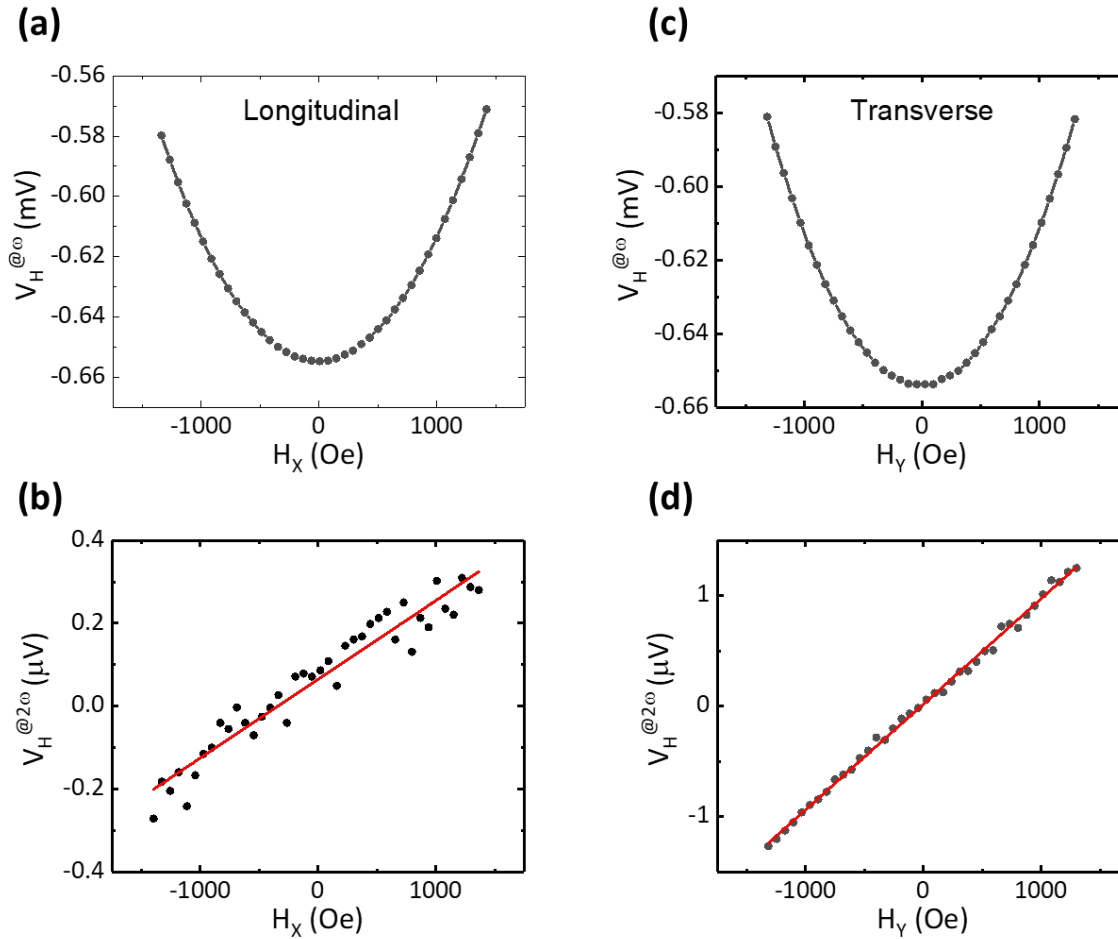
Figure 4.16. First and second harmonics Hall voltages for spin-orbit torques characterization. First harmonic (a) and second harmonic (b) Hall voltage for damping-like torque measurements. First harmonic (c) and second harmonic (d) Hall voltage for field-like torque measurements. The red lines in (b) and (d) are linear fittings to the data points. For (a-d), the applied current density through the W layer has a peak value of 2.73×10^{10} A/m², and the device has a Ti thickness of 1.0 nm. (*80*)

We also studied the SOT gradients in our samples using the harmonics method (*50-52*) (see Figure 4.16). A small ac current is applied to the device in presence of an in-plane magnetic field, either in the longitudinal (collinear with current) or transverse (perpendicular to current) directions for

damping-like and field-like fields, respectively. Following Eqs. 3.4-3.6, we can obtain the damping-like (ΔH_x^{DL}) and field-like (ΔH_y^{FL}) effective fields by considering the ratio between the anomalous and planar Hall effect resistances (ξ) (52):

$$\Delta H_x^{DL} = (B_x \pm 2\xi B_y)/(1 - 4\xi^2), \tag{4.2}$$

$$\Delta H_y^{FL} = (B_y \pm 2\xi B_x)/(1 - 4\xi^2), \tag{4.3}$$

where $\pm$ signs are used for down/up magnetizations. $\xi = \dfrac{R_{planar\ Hall}}{R_{anomalous\ Hall}}$ in our devices is around 0.12.

The extracted ΔH_x^{DL} and ΔH_y^{FL} for different applied current densities are plotted in Figure 4.17, where a linear dependence is observed. By a linear fitting we can obtain the effective damping-like and field-like efficiencies $\Delta H_{x(y)}^{DL(FL)}/J_W$, where J_W denotes the applied current density through the W layer. For both the damping-like and field-like cases, we find the effective SOT fields for both up and down magnetization states (for magnetization pointing along $\pm z$), where we observe a similar magnitude as expected.
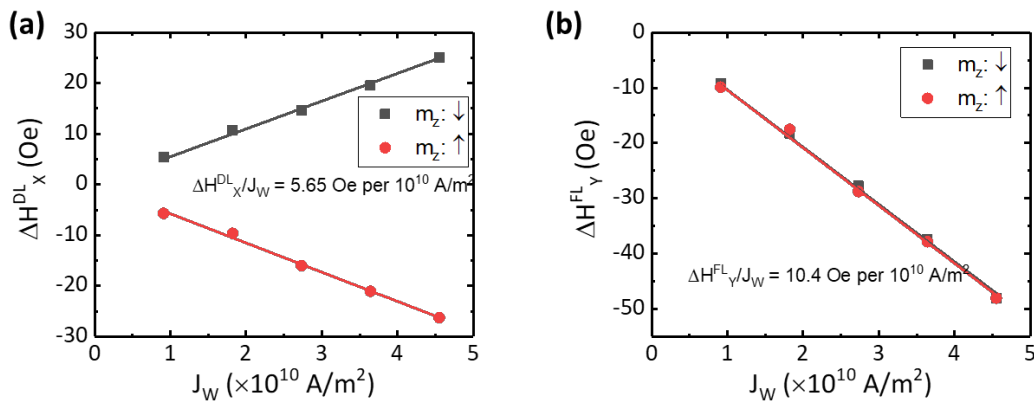
Figure 4.17. The extracted damping-like (ΔH_X^{DL}) and field-like (ΔH_Y^{FL}) effective fields, plotted in (a) and (b) for up/down magnetization states. By linear fitting, effective damping-like and field-like efficiencies

$\Delta H_{X(Y)}^{DL(FL)}/J_W$ are extracted (the numbers represent the average of the absolute values of down/up cases). (*80*)

We did the same measurements and analysis on different devices with different Ti insertion thicknesses to study the uniformity of SOT effective fields in our samples. We find that both the damping-like and field-like contribution to the SOTs are almost independent of the Ti insertion thickness (see Figure 4.18). This uniformity can be understood from the negligible spin-orbit coupling and long spin diffusion length of Ti. The SOTs in our samples have their main origin in the W layer, which is a 5d heavy metal, and the contribution of Ti (a 3d metal) to SOTs could be neglected because of its very small spin-orbit coupling. As a result, small variations of the Ti layer does not affect the SOTs in a rough approximation. Although the interfacial properties and spin-mixing conductance could be modified with different Ti insertion thicknesses, however, we find these variations to be quite small and less than 5%, based on the data from Figure 4.18. The obtained uniform magnetic anisotropy and switching current density suggests that our proposed approach is very promising for practical applications.
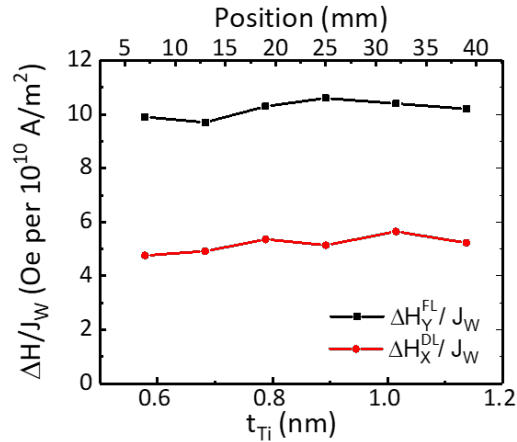
Figure 4.18. Field-like (ΔH_Y^{FL}) and damping-like effective fields (ΔH_X^{DL}) per unit current density applied to the W layer (J_W) as a function of the Ti insertion thickness/position of the devices. (*80*)

4.8 Angular Dependence of H_z^{EFF}

We studied the dependence of H_z^{eff} and β on the angle between current and Ti growth (wedge) directions. As expected from the broken symmetry, H_z^{eff} is proportional to $\boldsymbol{E_{ip}} \times \boldsymbol{p} = |\boldsymbol{E_{ip}}||\boldsymbol{p}| \sin \theta$ (according to the Rashba Hamiltonian mentioned earlier), where $\boldsymbol{E_{ip}}$ is the in-plane component of the effective electric field (along the wedge direction), $\boldsymbol{p}$ is the electron momentum, and θ is the angle between the two. Experimentally, we observe this $\sin \theta$ angular dependence (see Figure 4.19), in agreement with the physical picture discussed earlier. For these measurements, we fabricated a series of Hall bars rotated with some angle θ away from the wedge direction ($\theta = 0, 15, 30, 45, 60, 75, 90^o$) on a piece of film at the same Ti insertion thickness. For each of these devices, we measured H_z^{eff} as a function of the applied current density and subsequently extracted the corresponding slope $\beta = \frac{\partial H_z^{eff}}{\partial J}$. The maximum β is obtained when the current and wedge directions are perpendicular to one another, and as θ gets closer to 0°, the symmetry breaking is minimized and β is reduced. We should also add that for the case where wedge and current directions are parallel ($\theta = 0^o$), no deterministic switching is observed. These observations further confirm the significant role of structural symmetry breaking in our samples.
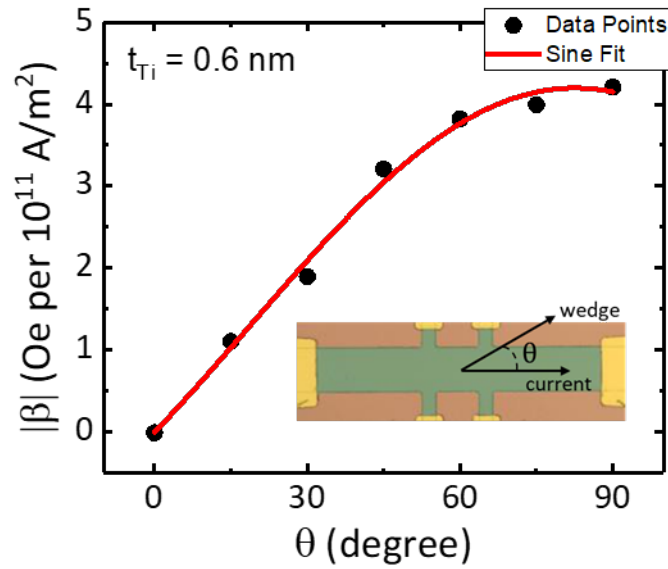
Figure 4.19. Angular dependence of β in devices with asymmetric Ti insertion. Here, θ is defined as the angle between Ti growth (wedge) and current directions, as shown in the inset. The Ti insertion thickness in this device is 0.6 nm. The red line shows a $\sin(\theta)$ fit to the data points. (*80*)

4.9 DISCUSSION ON RULING OUT TILTED ANISOTROPY

A trivial alternative explanation in our samples could rise from a possible tilted anisotropy away from the perpendicular direction. If because of the oblique-angle sputtering process, the magnetization's easy axis is tilted away from the z axis, then most of our observations could be explained without invoking the partly out-of-plane net spin polarization (*86*). However, we can experimentally rule out the role and presence of a possible tilted anisotropy in our samples. The first evidence was already provided in Figure 4.8, where we showed that H_z^{eff} is independent of the magnetization's direction, and is even created when the magnetization is fully saturated in the in-plane direction. This observation shows that we do not need a tilted magnetization to create H_z^{eff} and realize field-free SOT switching.

81

We can also quantitatively study a possible tilted anisotropy by observing the first harmonic data provided in Figure 4.16 (a) and (c). In these figures, the magnetic field is scanned along the x and y in-plane directions. If an anisotropy tilt (in y-z plane) exists in our samples, then the extrema of the first-harmonic signal should be shifted from zero, when the magnetic field is scanned along the y axis. After subtracting the external magnet's offset, we extracted the extrema of the first-harmonic signal by fitting it with a parabola in each case. After doing so, we found that on average, the extrema of the curves are very close to 0 Oe for the magnetic field scanned along both the x and y axes, which shows that no detectable anisotropy tilt exists in our devices.

We also did additional vibrating sample magnetometer (VSM) measurements with the help of our collaborators at the Chinese Academy of Sciences (*86*). We changed the angle between the perpendicular easy axis and the applied field (we rotated the applied field in y-z plane, with wedge direction being along the y axis). These results are shown in Figure 4.20. Here, 0° corresponds to magnetic field along the y axis, and 90° corresponds to magnetic field along the z axis. We can clearly see that our samples have perpendicular anisotropy. However, this method does not give us enough resolution to un-ambiguously resolve small changes in angle around the perpendicular applied field.
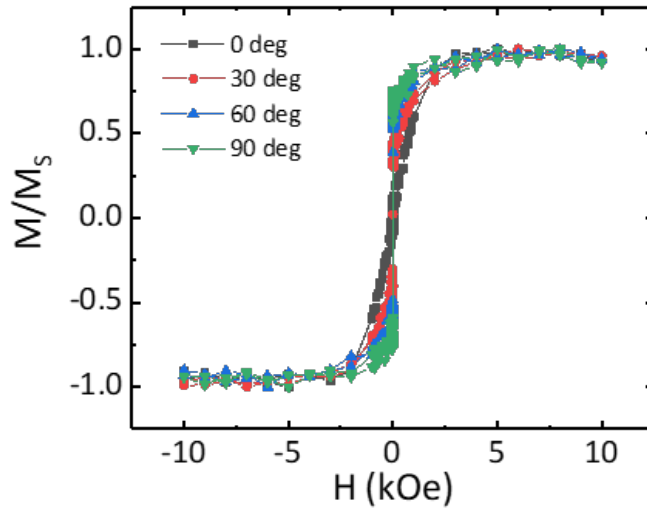
Figure 4.20. Angular-dependent VSM data. Hysteresis loops as a function of the angle between the perpendicular easy axis and the applied field along the y axis. 0° corresponds to magnetic field along the y axis and 90° corresponds to magnetic field along the z axis. Here, the Ti insertion thickness is 0.8 nm. (*80*)

4.10 OTHER ASYMMETRIC THIN LAYER INSERTIONS

The general concept presented for the case of W/Ti/CoFeB/MgO system mentioned above is not unique to this material system. Here we discuss similar observations in two other material systems: W/IrMn(w)/CoFeB/MgO and Pt/IrMn(w)/CoFeB/MgO (*87*). In these cases, W and Pt act as the main heavy metal layers in these two systems, respectively, and w denotes the wedge-shaped nature of the ultrathin IrMn insertion used for breaking the lateral structural symmetry. We should note that here the IrMn thickness is around 0.5-1 nm, so it does not have any antiferromagnetic properties at room temperature.

In Figure 4.21 we shows the results obtained for the W(5) / IrMn(w) / CoFeB(0.9) / MgO(2) system. As shown in Figure 4.21 (a), the hysteresis loops are shifted to opposite directions, just like the case of wedge-shaped Ti insertion. We also find a similar linear trend between the

83

induced effective fields H_z^{eff} and applied current density through the W layer (Figure 4.21 (b)).

Furthermore, a similar angular dependence for β as a function of the angle between wedge and

current directions is found (Figure 4.21 (c)). Similar results are also found for the case of Pt(5) /

IrMn(w) / CoFeB(0.9) / MgO(2) material system. The similarity of these results show that the

arguments presented earlier in this Chapter are general and not limited to a specific material

system, i.e., insertion of a thin asymmetric layer can generically give rise to H_z^{eff} and field-free

switching, expanding the choice of viable material systems.
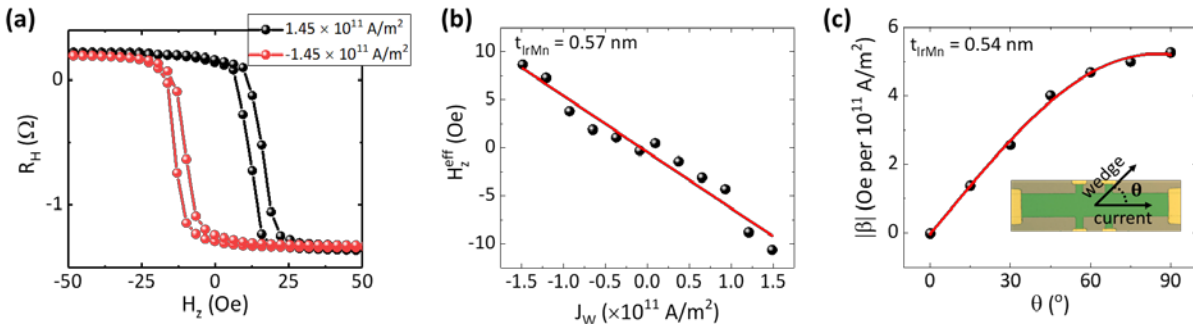
Figure 4.21. H_z^{eff} of the in W/IrMn(w)/CoFeB/MgO system. (a) Hysteresis loops with out-of-plane fields are shifted to opposite directions for opposite applied current densities, showing the induction of H_z^{eff}. (b) H_z^{eff} stays linear (in the studied range) as a function of the applied current density through the W layer (J_W). We defined β as the slope of this plot ($\frac{\partial H_z^{eff}}{\partial J_W}$). (c) Angular dependence of β as a function of the angle between the current and wedge directions (taken from Ref. (*87*)).

4.11 MOVING TOWARDS MUCH SMALLER THICKNESS GRADIENTS

Our data shows that SOT switching using an asymmetric light-metal layer can almost have all the

required characteristics of a practical solution to the deterministic field-free switching problem.

We obtain uniform coercivity, magnetic anisotropy, switching current density, and spin-orbit

torques. Furthermore, our solution has a very good thermal stability, and is not susceptible to

Joule heating effects. Another important advantage of this approach is that it is compatible with

any choice of high-SOC and magnetic materials and does not add any additional constraints on the material choice. The only minor disadvantage of this approach is that we still have a thickness gradient in the sample. As was mentioned earlier, the thickness gradient that we have used here translates to a thickness difference of around 3.5 nm over an 8-inch wafer. A typical magnetic tunnel junction has a thickness of around 40 nm (*83*), so there would be around 10% variation over the devices thickness on the two ends of the wafer. However, it could be expected that this thickness difference can be significantly reduced if one uses a smaller thickness gradient of the light-metal insertion layer. In our scaled devices, the Ti layer is virtually uniform and has no meaningful thickness difference across the device, but we still observe H_z^{eff} and field-free SOT switching. This shows the importance of the structural symmetry breaking because of the geometry of the sputtering process, i.e., the oblique angle deposition without substrate rotation. As a result, one can expect that by reducing the thickness gradient we can still observe similar effects. It will be very interesting to see if there is a lower bound on the thickness gradient, and to find the lowest possible one.

Along the same lines, we have observed similar effects even in devices with *nominal* uniform thickness. Namely, we sputter-deposited a stack of Ta(5) / $Co_{50}Fe_{50}$(0.45) / $Co_{40}Fe_{40}B_{20}$(0.45) / MgO(2) / Ta(2), where the numbers in parentheses represent thicknesses in nm. All these layers have uniform nominal thicknesses, and they are deposited with substrate rotation. The bottom Ta(5) serves as the material with high spin-orbit coupling and a source of SOTs, CoFe and CoFeB are both ferromagnets, MgO is an oxide that can be used as the tunneling barrier in MTJ structures, and the top Ta(2) serves as a capping layer to protect the sample from exposure to air. Here, instead of a single ferromagnet, we have used a bilayer ferromagnet.

For the experimental characterizations, we use anomalous Hall measurement on Hall bar devices, similar to the geometry shown in Figure 4.4.
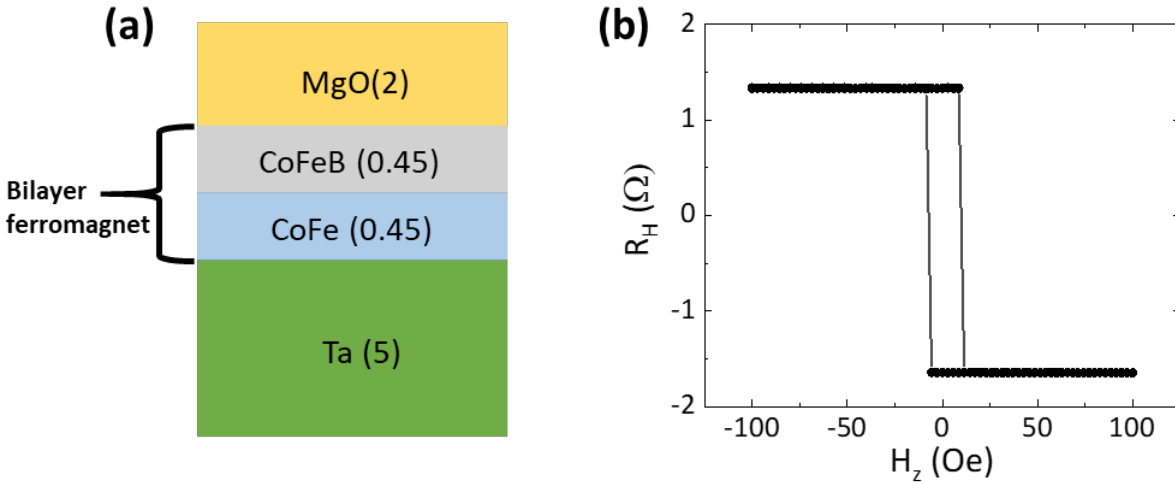
Figure 4.22. Bilayer ferromagnet heterostructure. (a) Core of the bilayer ferromagnet stack, where the numbers represent layer thicknesses in nm. (b) Anomalous Hall characterization of the easy axis loop. The sample has perpendicular magnetic anisotropy.

Figure 4.22 (a) shows the studied material system, in which CoFe/CoFeB is used as a bilayer ferromagnet. With these thicknesses, the sample has a perpendicular magnetic anisotropy, as can be seen from the anomalous Hall data in Figure 4.22 (b). We should note that all the layers in this sample have *nominal* uniform thicknesses. However, as we will see later, this might not be the case in practice.

We observe that the hysteresis loops are shifted to opposite directions upon applying currents along $\pm\hat{x}$, shown in Figure 4.23. This data shows that, similar to the case with Ti insertion, some current-induced effective out-of-plane magnetic fields (H_z^{eff}) are created in the sample.
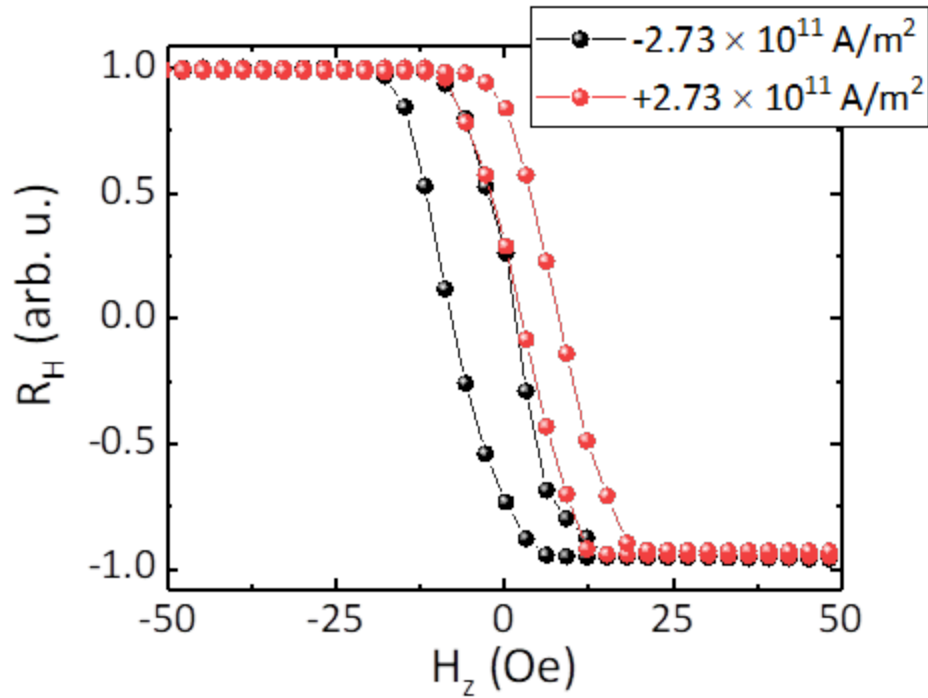
Figure 4.23. Hysteresis loop shifts in bilayer ferromagnet system, upon application of current in opposite directions ($\pm\hat{x}$). The current density is calculated for the Ta layer. R_H and H_z denote the anomalous Hall resistance and the perpendicular external field.

With the help of the induced H_z^{eff}, the symmetry between up/down states for each current polarity is broken and we can realize deterministic field-free SOT switching, as shown in Figure 4.24. For this measurement, current pulses of 1 ms duration are applied to the sample, with a 1 second wait between successive pulses. We can see that an almost complete magnetization switching is achieved by applying the current. Furthermore, this switching has a high thermal stability, meaning that it does not degrade because of the Joule heating effect.
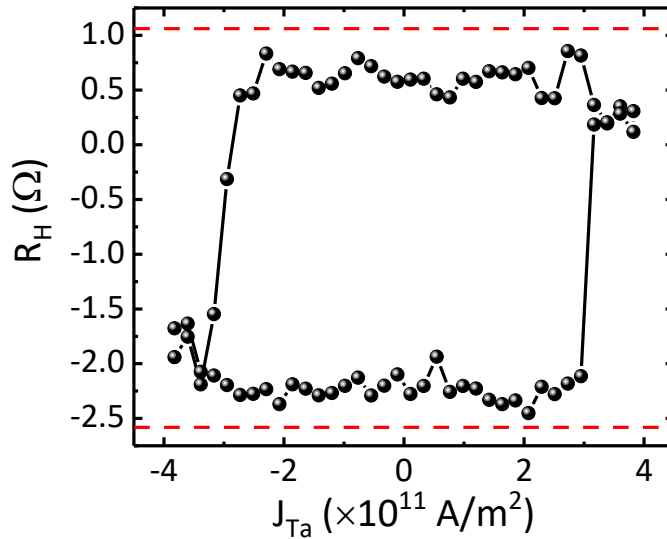
Figure 4.24. Deterministic field-free SOT switching using a bilayer ferromagnet. J_{Ta} represents the current density passing through the Ta layer. Red dashed lines show the maximum achievable anomalous Hall resistances. We can see that the SOT switching results in an almost complete reversal of the magnetic domains.

All these data are very similar to the results of the samples with asymmetric Ti insertion. Also,

from the symmetry arguments, we know that these are only possible if an inversion symmetry

breaking in the lateral direction exists in our samples (as explained in Chapter 2). In order to check

the presence of an in-plane broken inversion symmetry, we studied the angular dependence of

β values, defined in a similar way as $\beta = \frac{\partial H_z^{eff}}{\partial J_W}$, where J_W is the current density through the

heavy-metal layer.
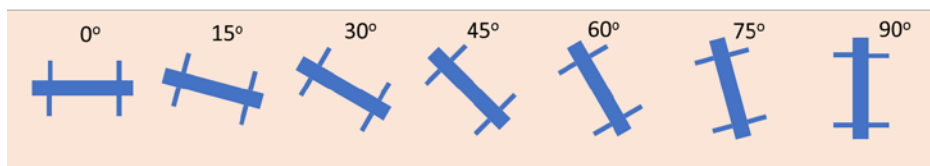
Figure 4.25. Device configuration for checking the angular dependence of β. 7 devices are fabricated on the film with different relative angles from 0° to 90°.

We fabricated our devices into Hall bars at different angles, where series of 7 devices with different relative angles are fabricated on the film (see Figure 4.25). The 0º device is fabricated in a random direction, as we do not have a well-defined symmetry breaking axis in our films. We then extracted the β in each of these devices by characterizing H_z^{eff} at different current densities. The resulting plot is shown in Figure 4.26.
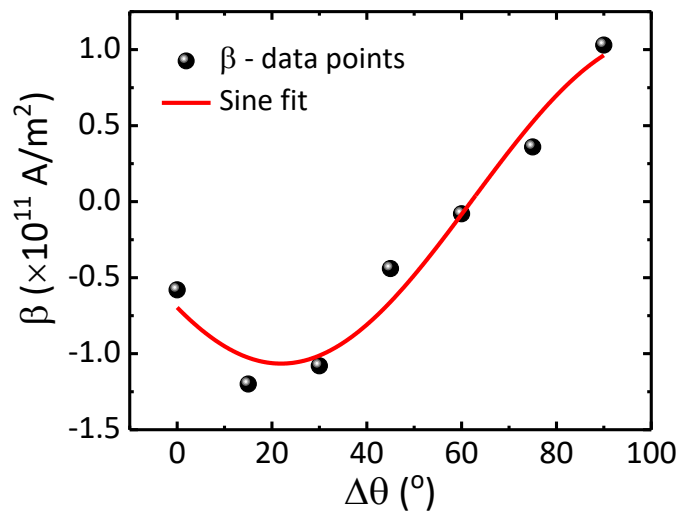
Figure 4.26. Angular dependence of β in devices with a bilayer ferromagnet.

We observe a very similar angular dependence to that of the devices with asymmetric Ti insertion layer (Figure 4.19). Such a sine function angular dependence can be well explained by the presence of an in-plane axis, along which the inversion symmetry is broken. In the case of the samples with asymmetric Ti insertion, we had a well-defined axis in the lateral direction, since we deposited Ti by stopping the substrate rotation. However, in the case of the bilayer ferromagnet, we do not have such a well-defined axis. We can conclude that although all the layers are *nominally* uniform, but in fact some of them have an asymmetric nature. We suspect that a slight asymmetry might exist in the bilayer ferromagnet. We should note that both the

CoFe and CoFeB are very thin (nominal thickness of 0.45 nm). With a deposition rate of around 0.3 $\mathring{A}$ per second, each of these layers are deposited in around 15 seconds, during which the substrate is constantly rotating. However, the substrate rotation frequency is around 0.5 Hz, meaning that in 15 seconds the substrate is rotated only 7-8 times. One plausible explanation might then be that 7-8 substrate rotations is not enough to induce a good uniformity over the whole sample, and a slight in-plane asymmetry might still exist. This can explain our observations based on the symmetry arguments presented earlier. However, more detailed studies are required to corroborate this conjecture.

The observed in-plane asymmetry and induction of H_z^{eff} in the bilayer ferromagnet system, which was supposed to be *nominally* uniform, suggests that the wedge effect can have very significant consequences, even if the thickness gradient is extremely small. Follow up studies are required to find the lower bound on the thickness gradient required for field-free SOT switching. These results suggest that field-free SOT switching with extremely small structural asymmetries might be possible.

4.12 SUMMARY

In this chapter, we discussed the realization of deterministic SOT switching without any external magnetic fields by inserting a slightly asymmetric thin light-metal layer at the heavy-metal/ferromagnet interface in conventional SOT heterostructures. The creation of current-induced H_z^{eff} can potentially be explained by the Rashba-Edelstein effect, where the light-metal layer deposited at an oblique angle breaks the symmetry in the lateral direction. By using this method, we have obtained uniform magnetic anisotropy, coercivity, spin-orbit torques and

switching current density across all the devices on a film, which is very promising for practical applications. We have also shown the scalability of our field-free switching approach by changing the device dimensions by 2 orders of magnitude. This method for field-free switching is also robust against the Joule heating effect, unlike the case of in-plane exchange bias field.

Furthermore, we realized field-free SOT switching in a structure with a bilayer ferromagnet, which supposedly had a uniform *nominal* thickness. However, we find that a slight in-plane asymmetry exists in the structure, which enables the induction of H_z^{eff} and field-free SOT switching. This promising result suggests that field-free SOT switching could be realized with extremely small thickness gradients, which will be compatible with wafer-scale device applications. We should also note that the proposed method for deterministic switching is compatible with various material systems, including topological insulators as a source of SOTs (*33, 34, 88-92*), promising a highly-efficient and practical magnetization switching mechanism.

5 OTHER RELATED WORKS

In this chapter, we discuss some of the unique and interesting aspects of the antiferromagnet-ferromagnet-oxide material system (IrMn/CoFeB/MgO), which we had developed primarily for field-free switching with the exchange bias field. In Chapter 3, we discussed the development of the IrMn/CoFeB/MgO material system, in which an exchange bias field and perpendicular magnetic anisotropy exists simultaneously (at room temperature). $Ir_{22}Mn_{78}$ is an antiferromagnet which also contains the 5d heavy metal Ir, $Co_{40}Fe_{40}B_{20}$ is a ferromagnet, and MgO is an oxide. In Chapter 3 we showed that an in-plane exchange bias field can be introduced at the IrMn/CoFeB interface, which can be used to replace the external field for realizing field-free deterministic SOT switching. Furthermore, we showed that IrMn can by itself create a sizable SOT for switching the CoFeB layer.

Here, we discuss several other effects that emerge in the IrMn/CoFeB/MgO material system. This material system has a number of interesting characteristics simultaneously: the presence of perpendicular magnetic anisotropy, a large spin-orbit coupling from Ir which facilitates spin-orbit torques and the Dzyaloshinskii-Moriya interaction (DMI), exchange bias field, voltage-control of magnetic anisotropy (VCMA), and hosting magnetic skyrmions. A basic discussion of the DMI, VCMA effect, and magnetic skyrmions is provided in the Appendix. In the following we show how the DMI in this structure can be used to stabilize magnetic skyrmions without any external magnetic fields. We also present that by applying voltage pulses and through the VCMA effect, we can create/annihilate magnetic skyrmions at zero external magnetic field. Furthermore, the spin-orbit torques from the IrMn layer can be used to drive the skyrmion motion. All these

interesting aspects of the IrMn/CoFeB/MgO material system makes it a very promising platform to enable the use of magnetic skyrmions for device applications. The data presented in this chapter is from several publications that I have co-authored, where I have contributed to material deposition and characterization, although I was not the leading author.

5.1 INTERFACIAL DZYALOSHINSKII-MORIYA INTERACTION AT THE IRMN-COFEB INTERFACE

The Dzyaloshinskii-Moriya interaction is an anti-symmetric exchange interaction which promotes the formation of chiral non-collinear spin texture in magnetic materials (refer to Appendix A1 for a detailed discussion of DMI). As such, DMI is fundamentally important in spintronic devices as it provides the spin texture chirality required for efficient domain wall motion, skyrmion stabilization, etc. There are two types of DMI, bulk and interfacial, where the latter is more important in thin film heterostructures presented in this dissertation. Interfacial DMI has been widely explored in heavy metal/ferromagnet heterostructures, where the perpendicular reflective symmetry is broken (*93-96*). However, it had been rarely studied in antiferromagnet/ferromagnet interfaces, where many interesting opportunities exist. IrMn-CoFeB provides such an interface; IrMn is an antiferromagnet which also has a high spin-orbit coupling because of Ir.

To study the DMI in this antiferromagnet-based structure, we sputter-deposited a series of IrMn-CoFeB-MgO thin films on Si/SiO$_2$ substrate and annealed them at 250 °C for 30 minutes. To induce exchange bias in the system and study its possible relationship with the DMI, we did the field cooling under an external magnetic field of 6 kOe to establish an in-plane exchange bias field. Then we obtained DMI coefficients D by examining the asymmetric spin wave dispersion in the

CoFeB layer, probed by Brillouin light scattering (BLS) measurements by our collaborators at UT Austin (*97, 98*). We observe that the D coefficient is inversely proportional to the CoFeB layer thickness, originating from the interfacial nature of the studied DMI (see Figure 5.1 (a)). In many previous studies on magnetic multilayers, the inverse proportionality to the ferromagnet thickness is considered as evidence for interfacial effects; other examples include exchange bias and magnetic anisotropy (*99, 100*). In these measurements, we kept the IrMn thickness at 5 nm.

Furthermore, we studied the DMI dependence on the IrMn thickness (and possibly on the antiferromagnetic order). Interestingly, we observed that the DMI coefficient increases almost linearly with the IrMn thickness, in the studied range of 1-7.5 nm (*97*) (see Figure 5.1 (b)). This dependence of DMI on the antiferromagnet thickness is different from that on the heavy-metal thickness in heavy-metal/ferromagnet interfaces.
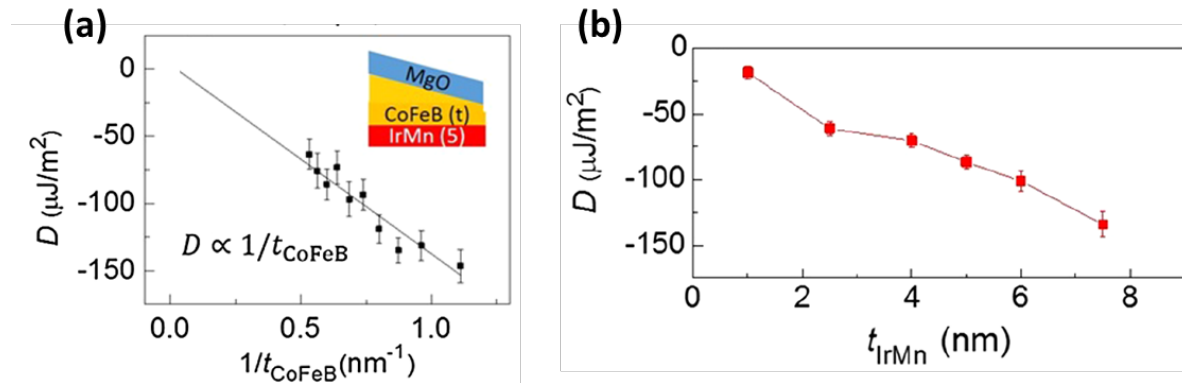
Figure 5.1. Interfacial DMI characterized in IrMn-CoFeB-MgO. (a) DMI coefficient dependence on the CoFeB thickness. Here the IrMn thickness is fixed at 5 nm. (b) DMI thickness dependence on the IrMn thickness. Here the CoFeB thickness is fixed at 2 nm. (taken from Ref. (*97*))

In this case of heavy-metal interface, it is suggested that the DMI is largely determined by the spin-orbit coupling of the first atomic layer of the heavy-metal, and extends weakly away from the interface (*93, 101*). In this case of interfacial DMI, the interaction between neighboring

ferromagnetic spins is mediated by the high-SOC site in the heavy-metal layer. As a result, increasing the heavy-metal layer's thickness beyond its spin diffusion length typically does not enhance the DMI. In other words, DMI dependence on the heavy-metal thickness has the form of:

$$D(t_{HM}) = \xi \left(1 - \exp\frac{-t_{HM}}{t_s} \right), \tag{5.1}$$

where ξ, t_{HM} and t_s are the maximum DMI coefficient, heavy metal thickness, and spin diffusion length of the heavy metal layer. However, our observations for the IrMn thickness-dependence of DMI is significantly different from the heavy metal case, noting that we assume the IrMn spin diffusion length is on the order of 1-2 nm (*102*). We suspect that the enhancement of DMI with increasing IrMn thickness beyond its spin diffusion length is correlated with the antiferromagnetic spin arrangement of IrMn (*97*). For thicker IrMn, the antiferromagnetic grain size increases and thermal fluctuations of spin arrangement decreases, which might contribute to the enhancement of DMI. It should also be noted that an alternative explanation might be that the spin diffusion length of IrMn is enhanced significantly with its thickness, which then results in a DMI enhancement as indicated by Eq. 5.1.

We also studied the simultaneous presence of exchange bias field and DMI in our samples. As mentioned in Chapter 3, the exchange bias field at room temperature appears in samples with IrMn thicknesses larger than about 5 nm. With a 5 nm IrMn, the obtained exchange bias is around 25 Oe, and the D coefficient is around 86 $\mu J/m^2$. With 7.5 nm IrMn, these numbers enhance to 350 Oe and 134 $\mu J/m^2$. Such magnitudes of DMI in IrMn are roughly similar to the ones with heavy-metal Au, larger than Ta or W, but smaller than those of Pt (*103*). Hence, although IrMn's

DMI is not very high, but it still is higher than many other conventional heavy metals, by which chiral domain walls and magnetic skyrmions have been enabled at room temperature. As a result, we can see that IrMn provides a unique platform for studying chiral spin textures by taking advantage of the exchange bias field simultaneously.

5.2 ROOM TEMPERATURE MAGNETIC SKYRMIONS IN IRMN-COFEB-MGO STABILIZED AT ZERO EXTERNAL FIELD

Here we show that the interfacial DMI at IrMn-CoFeB interface could be used to stabilize magnetic skyrmions at zero external field. Skyrmions are quasi-particles that can move around maintaining their configuration; as such they are a kind of soliton (refer to Appendix A.3 for more information on skyrmions). Magnetic skyrmions have a swirling spin texture with a nontrivial topology and can potentially have application in magnetic memory and storage devices (*104*). Furthermore, it has been proposed that skyrmion dynamics can be used as an intermediate step for voltage-induced magnetization switching (*105*).

Skyrmions have a chiral spin texture, consequently, they are stabilized by the chiral anti-symmetric exchange, i.e., the DMI. Skyrmions were first studied in bulk non-centrosymmetric B20 materials at low temperature (*106-108*), where they are stabilized by the bulk DMI (refer to Appendix A1 for more details on bulk and interfacial DMI). But later on, skyrmions with nanometer-scale dimensions were reported in thin film heterostructures (*109, 110*), stabilized by the interfacial DMI. More recently, skyrmions were found to be stable at room temperature in commonly used sputtered thin film heterostructures (*111-113*), promising potential applications in devices. In these systems, the interfacial DMI at the interface of a material with high SOC and

96

a ferromagnet is used to induce the chirality required for creating magnetic skyrmions. In all the previously studied material systems, a non-magnetic heavy metal was used as the material with high spin-orbit coupling. But as we have shown in Chapter 3, by using antiferromagnets as the SOC layer, one can add a variety of new functionalities into the system, including the exchange bias field. We show that the sizable DMI present at the IrMn-CoFeB interface could be used to create skyrmions, and by using the exchange bias magnetic field simultaneously present at the interface, we can stabilize skyrmions without any external magnetic field. This is in contrast to all of the previously studied thin film material systems, in which a small perpendicular magnetic field was required to stabilize skyrmions, making them impractical for applications. Furthermore, we show that the spin-orbit torques from the IrMn layer can be used to move skyrmions around. The data presented in this section is taken from Ref. (*114*).
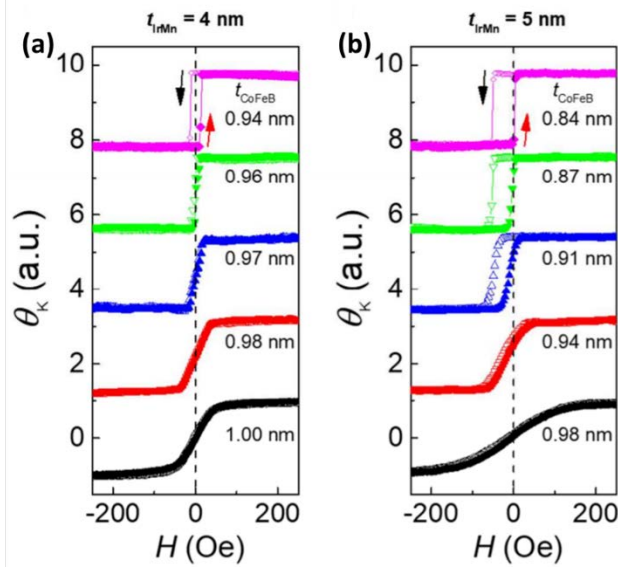
Figure 5.2. Tuning of perpendicular magnetic anisotropy using the CoFeB thickness. (a) and (b) show the out-of-plane (easy-axis) hysteresis loops obtained using MOKE, for samples with 4 and 5 nm of IrMn, respectively. (*114*)

Skyrmions are typically created with the right combination of perpendicular magnetic anisotropy, and DMI, consequently, we need to be able to tune both. A critical DMI magnitude D_c is necessary for skyrmion stabilization (*115*):

$$D_c \propto \sqrt{Jk}, \qquad\qquad (5.2)$$

where J and k are the exchange stiffness and effective uniaxial magnetic anisotropy constant, respectively. As was shown in Figure 5.1, we can easily tune the DMI strength by playing with the IrMn and CoFeB thicknesses. Perpendicular magnetic anisotropy could also be tuned by changing the CoFeB thickness (noting that the perpendicular anisotropy also has an interfacial origin). Figure 5.2 shows that even a small change of CoFeB thickness can cause the hysteresis loop to have a sharp/gradual switching, indicating a modulation of the effective anisotropy field. No exchange bias field is observed for the samples with 4 nm IrMn, since their exchange bias blocking temperature is below the room temperature (we define the blocking temperature as the temperature above which the exchange bias disappears). However, for samples with 5 nm of IrMn, an exchange bias field of around 20-40 Oe is created.
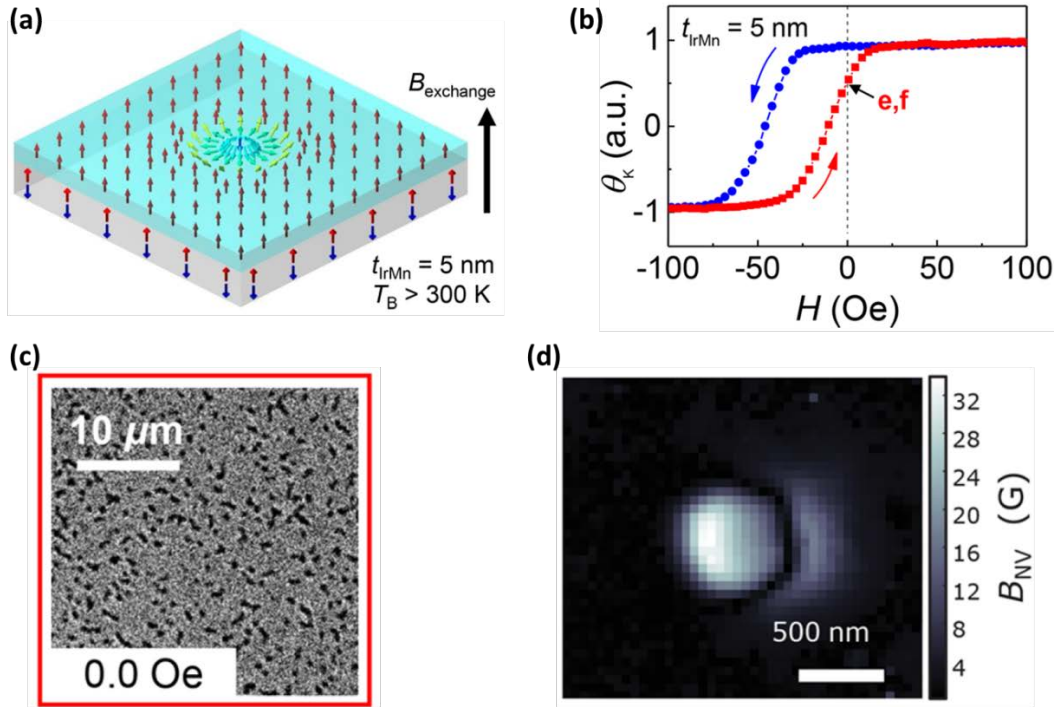
Figure 5.3. Zero-field skyrmions in IrMn-CoFeB-MgO. (a) Schematics of the skyrmion's spin texture stabilized by interfacial DMI. The exchange bias field replaces the external field and stabilizes skyrmions at zero external field. (b) Out-of-plane hysteresis loop of the optimized film stack, with nominal CoFeB thickness of 0.96 nm. (c) Polar magneto-optical Kerr effect (p-MOKE) image of the magnetic domains. The circular dots show magnetic skyrmions. (d) Scanning Nitrogen-Vacancy (NV) image of a single zero-field skyrmion, where the measured magnitude of the magnetic field along the NV axis is shown on right. (*114*)

By fine tuning the layers thicknesses, magnetic skyrmions were stabilized in this system (Figure 5.3). Importantly, we replaced the required external field for stabilizing skyrmions with the exchange bias field built-in in the material system, which is manifested in the hysteresis loop shift from the center in Figure 5.3 (b). In order to create skyrmions, first the magnetization is saturated by applying a large magnetic field in the negative direction, along the blue curve of Figure 5.3 (b). Then the magnetic field is reduced back to zero (red curve of Figure 5.3 (b), until it reaches point e,f). When the magnetic field is reduced back to zero, the magnetization starts to evolve into a multi-domain configuration, since the magnetic anisotropy is relatively small for the nominal CoFeB thickness of 0.96 nm. However, because of the presence of DMI, chiral spin textures, and

ultimately magnetic skyrmions emerged. We used polar MOKE imaging to study the magnetic domains, as shown in Figure 5.3 (c). Here, the small circular dots seem to show magnetic skyrmions, however, the MOKE microscope did not have enough resolution to resolve the skyrmion's spin texture. For a higher resolution image, NV-center imaging was performed by our collaborators at University of California, Santa Barbara (*114*). As shown in Figure 5.3 (d), skyrmions with a diameter of around 600 nm are observed.

These results show the creation of room-temperature skyrmions stabilized by the DMI from an antiferromagnet. The interfacial exchange bias field and stabilization of skyrmions at zero external field enable a lot of new possibilities for utilizing skyrmions in device applications. Furthermore, the SOT from the IrMn layer could be used to move magnetic skyrmions, as will be discussed in the next section. Next, we discuss an interesting demonstration of skyrmion creation/annihilation using single voltage pulses, based on the same material system of IrMn-CoFeB-MgO.

5.3 VOLTAGE-CONTROL OF MAGNETIC SKYRMIONS

In thin film heterostructures, skyrmions are created with the right combination of perpendicular magnetic anisotropy and DMI (see Eq. 5.2). In the previous section it was shown that both parameters can be adjusted by changing the thicknesses of different layers. However, it will be very desirable to have a dynamic control over these magnetic properties, as it would allow dynamic manipulation of the skyrmion/magnetic state. Here we show that using the voltage-controlled magnetic anisotropy (VCMA) effect, we can dynamically manipulate magnetic skyrmions that are fixed in space in a device (refer to Appendix A.2 for more details on the VCMA

effect). To demonstrate this manipulation, the same material system of IrMn-CoFeB-MgO was used. This work can potentially find applications in various kinds of memory/logic devices that utilize skyrmions. It can also be used to mediate voltage-induced magnetization switching (*105*). The data in this section is mostly taken from Ref. (*116*).
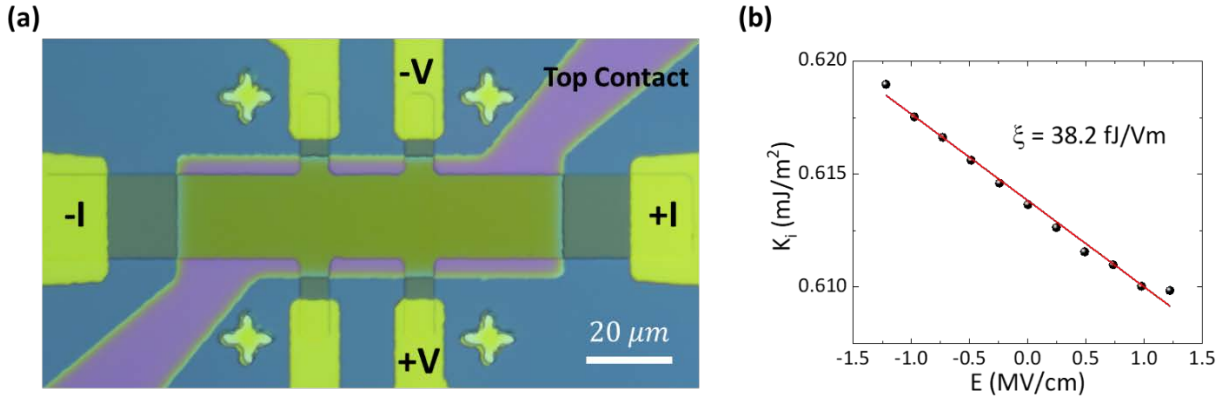
Figure 5.4. VCMA coefficient (ξ) in IrMn-CoFeB-MgO at room temperature. (a) Hall bar device with a top gate electrode. I and V shows the in-plane current and voltage channels used for anomalous Hall measurements. (b) The extracted interfacial perpendicular magnetic anisotropy energies (K_i) are plotted as a function of the electric field over the MgO layer. The slope yields the VCMA coefficient. (*116*)

We quantitatively characterize the VCMA coefficient in our material stack of IrMn-CoFeB-MgO, and the results is shown in Figure 5.4. These measurements are done on the Hall bar shaped devices with a gate electrode on top (see Figure 5.4 (a)). The full stack consists of Ta(2) / IrMn(5) / CoFeB(~1) / MgO(2) / Al$_2$O$_3$(35) / Cr-Au electrode, where the numbers represent thicknesses in nm. The bottom 2 nm of Ta serves as a buffer layer, MgO is the main insulating layer, and the thick Al$_2$O$_3$ is deposited to prevent vertical conduction under gate voltage (since the devices have large dimensions). Applied gate voltage can be converted to MgO's electric field using the relation

$E_{MgO} = \dfrac{V}{t_{MgO} + \frac{\epsilon_{MgO}}{\epsilon_{AlOx}} t_{AlOx}}$, where $\dfrac{\epsilon_{MgO}}{\epsilon_{AlOx}} = \dfrac{9}{7.5}$. For each of the electric fields shown in Figure 5.4, we

scanned the hard-axis hysteresis loop (with an in-plane magnetic field), and by fitting the areas

under the extracted curves we quantitatively found the effective interfacial anisotropy energy (detailed procedure can be found in (*117*)). The VCMA coefficient ξ can be found by linear fitting the data and finding the slope. We found ξ to be 38.2 fJ/Vm, which is a typical value for CoFeB-MgO before optimization for high VCMAs.

Using the VCMA effect in our samples, we can dynamically control the magnetic anisotropy and create/annihilate magnetic skyrmions with single voltage pulses at zero external magnetic field. In other words, by applying a gate voltage, the anisotropy is modified and hence the skyrmion stabilization condition is satisfied/dissatisfied (referring to Eq. 5.2). We first create skyrmions by scanning the external magnetic field starting from a uniform magnetization state (similar procedure as the one shown in Figure 5.3 (b)). Hence, the initialized state at zero magnetic field consists of several skyrmions and some chiral domains (see Figure 5.5). Here the skyrmions are stabilized by the interfacial exchange bias field. Next, by applying a single negative voltage pulse, we can annihilate skyrmions and go back to a uniform magnetization state. The VCMA coefficient in our samples is negative, so applying a negative voltage pulse enhances the magnetic anisotropy. An enhanced magnetic anisotropy overcomes the DMI effect and establishes a uniform magnetic state. Next, we apply a positive voltage pulse and we can again create some of the skyrmions. A positive voltage decreases the anisotropy and allows for the DMI to create skyrmions again. Interestingly, the skyrmion creation and annihilation processes are both non-volatile, meaning that applying the voltage pulse results in a permanent change of the magnetization state. As a result, a complete VCMA-control over the skyrmion creation/annihilation process without any external magnetic fields is demonstrated. This process is also repeatable, as shown in Figure 5.5.
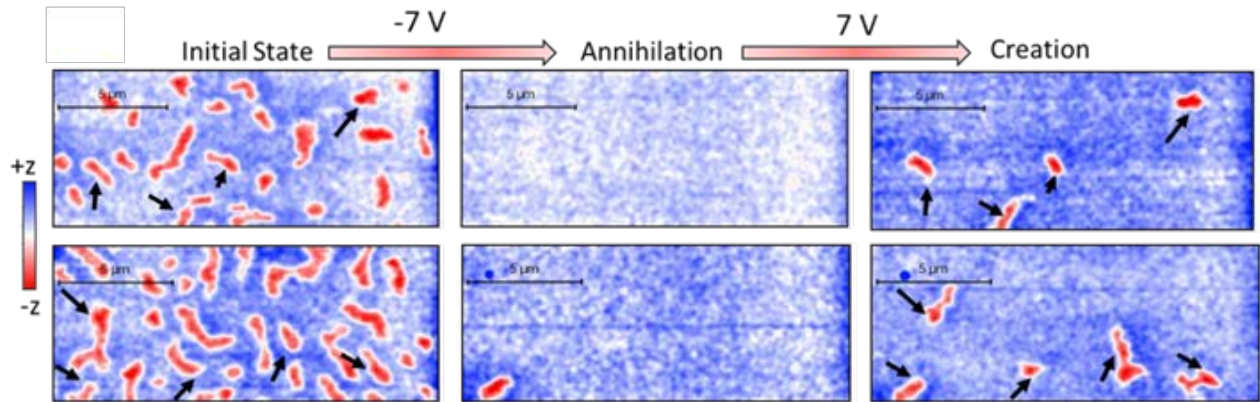
Figure 5.5. VCMA-control of skyrmion creation/annihilation process at zero external magnetic field. Starting from an initial state consisting of several skyrmions and domain walls, almost all of the skyrmions are annihilated by applying a single negative voltage pulse. Then, skyrmions and chiral domains are again created by applying a positive voltage pulse. These processes are all non-volatile. The two rows show the same procedure applied twice to the device. The images are obtained using magnetic force microscopy (MFM). The same device structure as that of Figure 5.4 is used. (*116*)

In this experiment, a single voltage pulse with a peak of 7.5 V is used, which corresponds to a 0.157 V/nm electric field in MgO. Here, the applied voltage pulses are 1-2 seconds long, however, we expect similar effects to occur with much shorter current pulses on the order of few nanoseconds at the least (timescale set by the skyrmion breathing mode). But the experimental study of the voltage pulse width remains for future work.

In Figure 5.5, the magnetic texture is captured using magnetic force microscopy (MFM), performed by our collaborators at Virginia Commonwealth University (*116*). But since MFM does not have enough spatial resolution, the spin texture of the created skyrmions could not be obtained. In order to show that the observed textures are indeed skyrmions, the skyrmion Hall effect was studied.
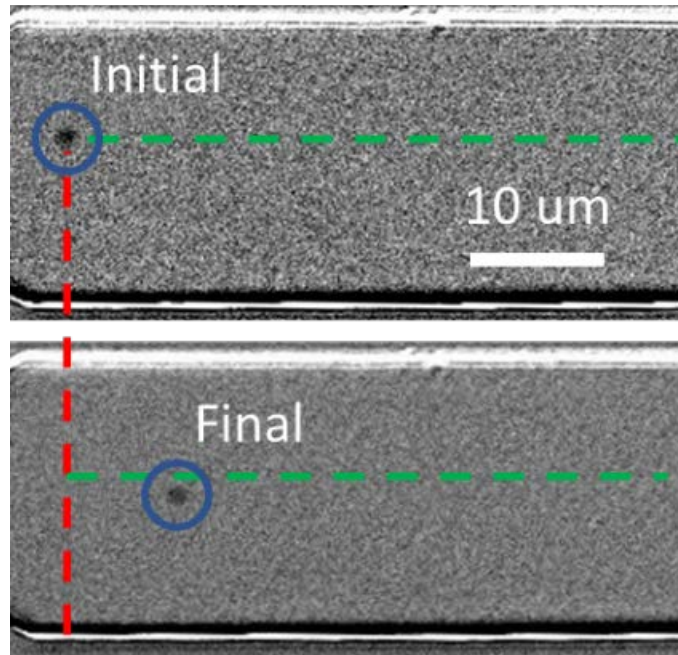
Figure 5.6. Current-driven skyrmion motion imaged using MOKE microscopy. The current pulse used has 9 mA amplitude (a current density of 8.3×10^6 A/m^2 through the IrMn layer) and a duration of 5 ms. Blue circles indicate the position of the skyrmion before and after the application of current pulse. The red and green dashed lines show the initial vertical and horizontal skyrmion position. The skyrmion shows a vertical shift in additional to the horizontal one, which is due to the skyrmion Hall effect. (*116*)

For these measurements, we first create skyrmions, then we apply an in-plane current to the

IrMn layer to create spin-orbit torques. We have shown in Chapter 3 that the IrMn SOTs are large

enough to drive domain wall motion and even switch the magnetization. We apply current pulses

of 9 mA in amplitude with a duration of 5 ms, and as a result of SOTs, skyrmions move with the

current pulses (see Figure 5.6). However, the direction of current-driven skyrmion motion is not

along the current direction and has a transverse component. This phenomenon is the so-called

skyrmion Hall effect (*118*), which is generated by a Berry phase from the topological structure of

a magnetic skyrmions, and serves as its signature. The calculated skyrmion Hall angle is 10.4°,

which is on the same order as that of similar material systems. This result further confirms our

observation that the observed magnetic textures have a topological texture and are indeed magnetic skyrmions.

Here we discuss several interesting perspectives that need to be studied further in the future. In all the analyses above, we have neglected the possible tuning of the DMI with the gate voltage. Since DMI is a result of SOC, we anticipate that it can be controlled by a gate voltage in our structure, like the VCMA effect. Although there are reports that the DMI can also be modulated by electric field (*119*), however, we assume that it has a small effect on our results. This hypothesis can be somewhat confirmed from micromagnetic simulations with the same material parameters and assuming a constant DMI, where very similar skyrmion dynamics has been reproduced by our collaborators at Virginia Commonwealth University (*120*). However, possible large DMI modulations by electric field could be further investigated for adding new functionalities to the existing devices. As mentioned previously, DMI is a very fundamental property in spintronic devices, and a dynamic control of the DMI can have many interesting applications.

Another aspect that needs more study is the applied voltage pulse width. As was mentioned above, we used a long voltage pulse of around 1-2 seconds for these measurements. However, it could be expected that similar results should still be obtained even if the voltage pulse width is reduced to the scale of the skyrmion dynamics timescale (set by the breathing mode), which is on the order of 1~10 ns (*105*). Furthermore, here using big Hall bar devices, the skyrmions are not affected by the boundaries of the device. But in a practical case, we need to confine skyrmions to nanometer-scale dimensions, which might impact the skyrmion diameter and its

dynamics. Studying skyrmion creation/annihilation in a scaled size geometry can be another interesting topic.

5.4 SUMMARY

In this chapter, we used the antiferromagnet-based material platform, IrMn-CoFeB-MgO, to study DMI, VCMA, magnetic skyrmions, and their voltage control. Although we developed and optimized this material system for the purpose of studying field-free SOT switching of perpendicular magnetization, but it turned out to be a perfect platform for exploring several other interesting physics and device applications. We showed that the IrMn-CoFeB interface has a sizable DMI that scales almost linearly with the IrMn thickness up to at least 7.5 nm. This DMI is large enough to create skyrmions at room temperature. Furthermore, the perpendicular exchange bias field in the IrMn-CoFeB could be used to stabilize skyrmions without requiring any external magnetic fields. SOTs from the IrMn layer were also shown to drive skyrmion dynamics.

In addition to studying DMI and skyrmions, the presence of a sizable VCMA effect in this material system was used to demonstrate skyrmions creation/annihilation with single voltage pulses of opposite polarity. The skyrmion creation/annihilation process is nonvolatile and repeatable. All these results show that the IrMn-CoFeB-MgO platform is very promising for studying skyrmions and their dynamics and may be further used for investigating interesting physics and useful device applications.

6 SUMMARY

Spintronic devices can offer a significant advantage in this era where the transistor scaling is getting close to its limits and is becoming increasingly hard. We can add a lot of functionalities to existing electronic devices if we use both the electron charge and the spin degrees of freedom. In this dissertation we showed one such added functionality, namely, switching magnetization with electric current that can find application in random-access integrated memory devices. The advantages of these magnetic memories include the zero standby power, non-volatility, fast operation speed and high endurance, which make them very desirable candidates for embedded applications.

Motivated by this goal, we focused on using spin-orbit torques for switching perpendicular magnetization. We discussed how we can use spin-orbit coupling in heavy metals to create a net spin polarization, and how we can use this spin polarization to apply torques on an adjacent magnet and switch it under proper conditions (Chapter 1). Furthermore, we discussed the symmetries and forms of spin-orbit torques in detail in Chapter 2. Although SOT switching of perpendicular magnetization has been demonstrated in research in the past decade, but for deterministic switching to happen, an external magnetic field collinear with the current is required which is not practical for device applications. We tackled this major issue by providing two main solutions based on using an in-plane exchange bias field (Chapter 3), and structural asymmetry (Chapter 4).

In the exchange bias approach, we replaced the external magnetic field required for deterministic switching by a built-in exchange bias field in the structure, created at an antiferromagnet-

ferromagnet interface. We also showed that this solution can be compatible with MTJs, if an antiferromagnet-ferromagnet-oxide (such as IrMn-CoFeB-MgO) heterostructure is used. In this case, the antiferromagnet provides both the exchange bias field and the SOTs, and the oxide layer serves as the tunneling barrier for MTJ readout. One potential drawback of this solution is that it limits the SOT material choice, i.e., we can only use certain antiferromagnets as the SOC layer. However, such antiferromagnets (e.g., IrMn, PtMn) do not possess very large SOTs (*46, 74*), limiting the energy efficiency. Furthermore, the non-uniform distribution of the exchange bias field over the device results in an incomplete magnetization switching (*47*). Another potential drawback of this approach is that the exchange bias is very sensitive to the Joule heating effect (*45*) due to a low blocking temperature required for low pinning, consequently, the current-induced heating reduces the exchange bias field and degrades the field-free switching.

In the second approach, we modified the structures symmetries to allow for the creation of an effective current-induced perpendicular magnetic field. Such an effective magnetic field breaks the symmetry between the up/down states and facilitates the complete magnetization switching without any external fields. We broke the structure's lateral symmetry by inserting an asymmetric light-metal layer between the heavy-metal and the ferromagnet of our structure. Light metals such as Ti have negligible spin-orbit coupling, consequently, they do not modulate the SOC-related parameters of the structure. As a result, we could obtain uniform magnetic anisotropy, SOTs, coercivities, and critical switching current densities, despite the slight non-uniformity of the structure. Furthermore, the creation of effective perpendicular magnetic fields is not susceptible to the Joule heating, which results in the superior thermal stability of the structural asymmetry approach.

Among these two solutions, structural asymmetry was shown to provide significant practical advantages, including freedom over the material choices, better thermal stability and complete magnetization switching. It should be recognized that several other approaches for field-free deterministic SOT switching have been proposed and realized, including interlayer exchange coupling (*48*), a gradient of spin current (*121*), and tilted magnetic anisotropy (*86*), among others (*77*). However, some of these approaches have severe limitations: creating a gradient of spin current requires additional piezoelectric layers, and tilted magnetic anisotropy requires very complicated device fabrication processes which are not scalable. Among these, interlayer exchange coupling can be a potentially practical solution. This approach is based on exchange coupling an additional in-plane ferromagnet in the stack to the perpendicularly magnetized free layer. However, the use of in-plane ferromagnets is a negative factor for device scaling, as it requires shape anisotropy. By comparing the pros and cons of each of these approaches, we can see that the structural asymmetry solution presented in Chapter 4 is among the most promising deterministic field-free SOT switching methods for practical applications.

Lastly, in Chapter 5, some of the other interesting aspects of the IrMn-CoFeB-MgO material system were discussed. This material system is based on IrMn, which is an antiferromagnet with a high spin-orbit coupling. Consequently, it hosts several interesting phenomena, including the presence of the Dzyaloshinskii-Moriya interaction, the voltage-control of magnetic anisotropy effect, and the stabilization of magnetic skyrmions. We studied each of these effects in Chapter 5: we showed that the sizable DMI and the exchange bias in this system can be used for stabilizing magnetic skyrmions at zero external field, furthermore, we showed that the VCMA effect could be utilized for skyrmion creation/annihilation with voltage pulses, and the SOTs from IrMn can

be used for driving the skyrmion motion. All these results show that the IrMn-CoFeB-MgO

platform is very promising for studying skyrmions and exploring their applications in spintronic

devices.

A.1 DZYALOSHINSKII-MORIYA INTERACTION

Dzyaloshinskii-Moriya interaction (DMI) is the anti-symmetric contribution to the magnetic exchange interaction between neighboring spins (*122, 123*), which its microscopic Hamiltonian can be expressed as $\mathcal{H}_{DMI} = -\boldsymbol{D}_{ij} \cdot (\boldsymbol{S}_i \times \boldsymbol{S}_j)$. Here, $\boldsymbol{D}_{ij}$ is the DMI vector whose direction depends on the DMI type and structure's symmetries, and $\boldsymbol{S}_{i,j}$ are neighboring spins. DMI promotes a non-collinear spin texture, whereas Heisenberg exchange interaction promotes a collinear one ($\mathcal{H} = -J(\boldsymbol{S}_i \cdot \boldsymbol{S}_j)$).
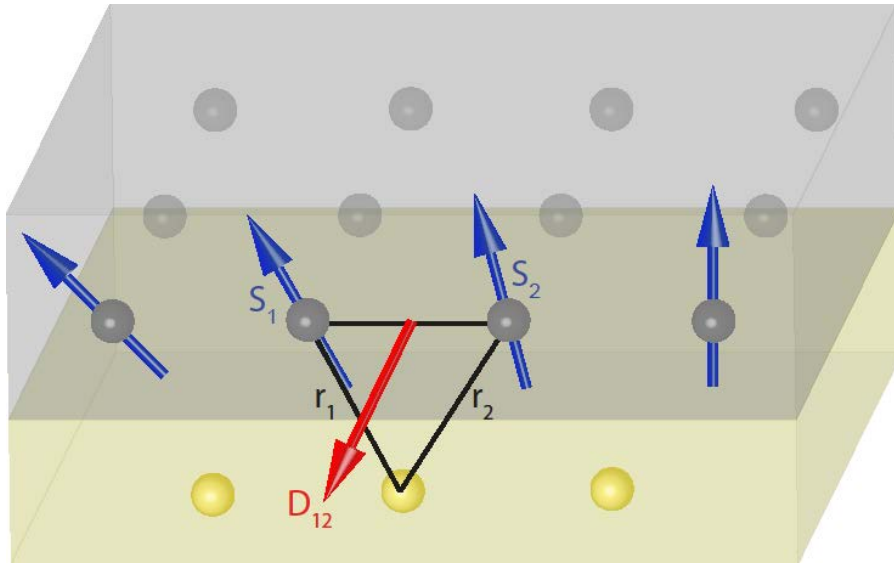
Figure A.1. Interfacial Dzyaloshinskii-Moriya interaction (DMI). The anti-symmetric exchange interaction between two neighboring spins $\boldsymbol{S}_{1,2}$ in a ferromagnet (gray) is mediated by a high spin-orbit coupling site (yellow). This configuration shows the interfacial DMI, where the direction of vector $\boldsymbol{D}$ is given by $\boldsymbol{r}_1 \times \boldsymbol{r}_2$. DMI favors a non-collinear spin texture.

DMI arises as a combination of spin-orbit coupling and a lack of inversion symmetry and has both bulk and interfacial types. In heterostructures, the inversion symmetry is broken at the interface

of dissimilar materials and gives rise to the interfacial DMI. In this case, two neighboring spins in a magnetic material are spin-orbit coupled to a third non-magnetic atom in an adjacent layer (see Figure A.1). Fert and Levy derived the interfacial DMI vector as (*124*):

$$\boldsymbol{D}_{ij}^{int} = D_{ij}(\boldsymbol{r_i} \times \boldsymbol{r_j}), \tag{A.1}$$

where D_{ij}^{int} shows the magnitude of the DMI vector, and $\boldsymbol{r_{i,j}}$ are vectors connecting the magnetic atoms to the non-magnetic atom. The interfacial DMI vector is parallel to the interface and causes spin texture rotation around it. The chirality of the resulting non-collinear spin texture depends on the DMI sign, which is determined by the material properties. For example, Pt/Co has an opposite DMI sign compared with Ir/Co (*101, 125*).

In the case of bulk DMI, the inversion symmetry is broken in non-centrosymmetric crystal structures, such as B20 compounds (*126*). The bulk DMI vector is given by (*127*):

$$\boldsymbol{D}_{ij}^{bulk} = D_{ij}^{bulk}(\boldsymbol{r_i} - \boldsymbol{r_j}), \tag{A.2}$$

where D_{ij}^{bulk} represents the magnitude of the bulk DMI vector.

A.2 Voltage-Control of Magnetic Anisotropy

The fundamental principle behind the voltage-control of magnetic anisotropy (VCMA) effect is spin-orbit coupling. Upon the application of a voltage, charge accumulation/depletion at the ferromagnet-insulator (such as CoFeB/MgO) interface modifies the electron occupancy of the different ferromagnet's d orbitals. Each of these orbitals possess different magnetic anisotropies due to spin-orbit coupling, hence, the applied voltage modulates the total magnetic anisotropy (*128*). In the presence of SOC, the magnetic orbital momentum is given by (*129*):

$$\boldsymbol{m}_{orb} = \mu_B \sum_{i,j} \frac{\langle \phi_i | \boldsymbol{L} | \phi_j \rangle \langle \phi_i | \boldsymbol{H}_{SOC} | \phi_j \rangle}{E_i - E_j}, \qquad (A.3)$$

where μ_B is the Bohr's magnetron, ϕ_i is the wavefunction corresponding to an occupied orbital, ϕ_j to an un-occupied orbital, $E_{i,j}$ is their corresponding energies, $\boldsymbol{L}$ is the angular momentum operator, and $\boldsymbol{H}_{SOC}$ is the spin-orbit coupling Hamiltonian. Coupling between occupied and un-occupied orbitals very close to the Fermi level E_F will have the dominant contribution to the orbital momentum. The uniaxial anisotropy energy can then be approximated as (129):

$$\Delta E_{ani} \propto \left(m_{orb}^{\perp} - m_{orb}^{\parallel} \right), \qquad (A.4)$$

where $m_{orb}^{\perp}$ and $m_{orb}^{\parallel}$ are the orbital magnetic moments in perpendicular and in-plane directions. Based on these equations, we can explain the main VCMA mechanism in ferromagnet/oxide bilayers: the electric field at the ferromagnet/oxide interface can modulate the orbitals, resulting in an increase or decrease of the orbital magnetic moments in different directions. Hence, $m_{orb}^{\perp}$ and $m_{orb}^{\parallel}$ are modulated with the electric field, and as a consequence, the total magnetic anisotropy of the sample can be modulated with the electric field.
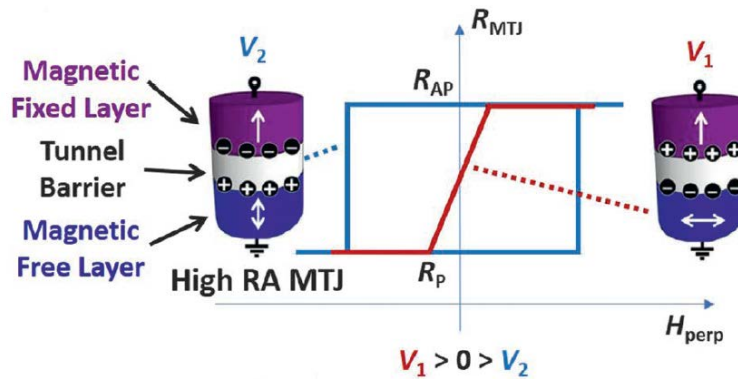
Figure A.2. Voltage-controlled magnetic anisotropy (VCMA) effect. The magnetic anisotropy of the magnetic free layer is modulated by applying a voltage over the magnetic tunnel junction (MTJ) stack. Here, the tunnel barrier has a high resistance × area (RA), so it does not allow conduction much.

VCMA effect can be observed in magnetic tunnel junctions, where a free magnetic layer and an oxide are interfaced. In such structures, the application of a positive or negative voltage can decrease or increase the magnetic anisotropy (see Figure A.2). We should note that in additional to this mechanism, it has also been proposed that the Rashba splitting of the band structure can have a contribution to the VCMA effect (*131*). Large VCMA effects have been observed at Fe-oxide interfaces (*132-134*), and consequently at the CoFeB-MgO interface, as discussed in Chapter 5.

A.3 MAGNETIC SKYRMIONS

Magnetic skyrmions are particle-like topological spin textures that hold promise as information carriers in magnetic devices (*104*). The chiral spin texture of skyrmions originates from the Dzyaloshinskii-Moriya interaction, where interfacial and bulk DMIs give rise to Néel and Bloch skyrmions, respectively (see Figure A.3).
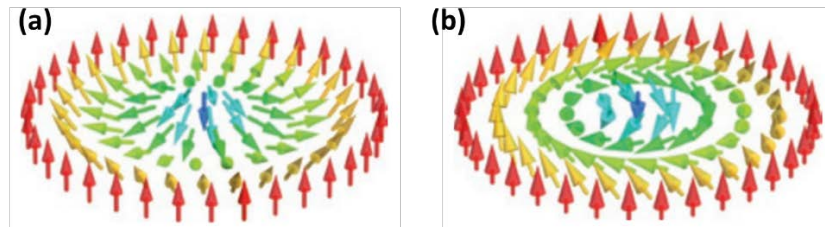
Figure A.3. (a) A Néel magnetic skyrmion. (b) A Bloch magnetic skyrmion. Picture taken from Ref. (*104*).

In thin film heterostructures, skyrmions are created with a combination of the perpendicular magnetic anisotropy, Heisenberg exchange, dipolar energy, and interfacial DMI (*111*). Starting from a uniform ferromagnetic state, the DMI tilts neighboring spins by a rotation around the DMI

vector (following Eq. A.1). A critical DMI magnitude D_c is necessary for skyrmion stabilization (*115*):

$$D_c \propto \sqrt{Jk}, \quad\quad\quad (A.5)$$

where J and k are the exchange stiffness and effective uniaxial magnetic anisotropy constant, respectively. The skyrmion size is roughly determined by the ratio between the magnitudes of DMI D and exchange coupling J (*104*), where a larger D/J ratio favors faster rotation of the spin texture, and hence, a smaller skyrmion size.

References

1. The Nobel Prize in Physics 1956 https://www.nobelprize.org/prizes/physics/1956/summary/.

2. The Nobel Prize in Physics 2000, for integrated circuits https://www.nobelprize.org/prizes/physics/2000/summary/.

3. G. E. Moore. (McGraw-Hill New York, NY, USA:, 1965).

4. K. J. Kuhn, Considerations for ultimate CMOS scaling. *IEEE transactions on Electron Devices* **59**, 1813-1828 (2012).

5. S. Salahuddin, K. Ni, S. Datta, The era of hyper-scaling in electronics. *Nature Electronics* **1**, 442-450 (2018).

6. P. A. M. Dirac, The quantum theory of the electron. *Proceedings of the Royal Society of London. Series A, Containing Papers of a Mathematical and Physical Character* **117**, 610-624 (1928).

7. I. Žutić, J. Fabian, S. Das Sarma, Spintronics: Fundamentals and applications. *Reviews of Modern Physics* **76**, 323-410 (2004).

8. L. D. P. L. P. L. E. M. Landau, Statistical physics Part 2, Part 2. Oxford; New York [etc.]: Pergamon Press, 1981.

9. T. L. Gilbert, A phenomenological theory of damping in ferromagnetic materials. *IEEE transactions on magnetics* **40**, 3443-3449 (2004).

10. L. Berger, Emission of spin waves by a magnetic multilayer traversed by a current. *Physical Review B* **54**, 9353-9358 (1996).

11.   J. C. Slonczewski, Current-driven excitation of magnetic multilayers. *Journal of Magnetism and Magnetic Materials* **159**, L1-L7 (1996).

12.   E. B. Myers, D. C. Ralph, J. A. Katine, R. N. Louie, R. A. Buhrman, Current-Induced Switching of Domains in Magnetic Multilayer Devices. *Science* **285**, 867 (1999).

13.   M. Tsoi, A. G. M. Jansen, J. Bass, W. C. Chiang, M. Seck, V. Tsoi, P. Wyder, Excitation of a Magnetic Multilayer by an Electric Current. *Physical Review Letters* **80**, 4281-4284 (1998).

14.   A. Brataas, A. D. Kent, H. Ohno, Current-induced torques in magnetic materials. *Nature Materials* **11**, 372-381 (2012).

15.   M. Julliere, Tunneling between ferromagnetic films. *Physics Letters A* **54**, 225-226 (1975).

16.   T. Miyazaki, N. Tezuka, Giant magnetic tunneling effect in Fe/Al2O3/Fe junction. *Journal of Magnetism and Magnetic Materials* **139**, L231-L234 (1995).

17.   J. S. Moodera, L. R. Kinder, T. M. Wong, R. Meservey, Large Magnetoresistance at Room Temperature in Ferromagnetic Thin Film Tunnel Junctions. *Physical Review Letters* **74**, 3273-3276 (1995).

18.   G. Hu, J. J. Nowak, M. G. Gottwald, J. Z. Sun, D. Houssameddine, J. Bak, S. L. Brown, P. Hashemi, Q. He, J. Kim, C. Kothandaraman, G. Lauer, H. K. Lee, T. Suwannasiri, P. L. Trouilloud, D. C. Worledge, Reliable Five-Nanosecond Writing of Spin-Transfer Torque Magnetic Random-Access Memory. *IEEE Magnetics Letters* **10**, 1-4 (2019).

19.   R. Winkler, S. Papadakis, E. De Poortere, M. Shayegan, *Spin-Orbit Coupling in Two-Dimensional Electron and Hole Systems*. (Springer, 2003), vol. 41.

20.   A. Soumyanarayanan, N. Reyren, A. Fert, C. Panagopoulos, Emergent phenomena induced by spin–orbit coupling at surfaces and interfaces. *Nature* **539**, 509-517 (2016).

117

21.   A. Manchon, J. Železný, I. M. Miron, T. Jungwirth, J. Sinova, A. Thiaville, K. Garello, P. Gambardella, Current-induced spin-orbit torques in ferromagnetic and antiferromagnetic systems. *Reviews of Modern Physics* **91**, 035004 (2019).

22.   M. I. Dyakonov, V. I. Perel, Current-induced spin orientation of electrons in semiconductors. *Physics Letters A* **35**, 459-460 (1971).

23.   J. E. Hirsch, Spin Hall Effect. *Physical Review Letters* **83**, 1834-1837 (1999).

24.   Y. K. Kato, R. C. Myers, A. C. Gossard, D. D. Awschalom, Observation of the Spin Hall Effect in Semiconductors. *Science* **306**, 1910 (2004).

25.   J. Sinova, S. O. Valenzuela, J. Wunderlich, C. H. Back, T. Jungwirth, Spin Hall effects. *Reviews of Modern Physics* **87**, 1213-1260 (2015).

26.   S. Takahashi, S. Maekawa, Spin current, spin accumulation and spin Hall effect. *Science and Technology of Advanced Materials*, (2008).

27.   H. Wu, P. Zhang, P. Deng, Q. Lan, Q. Pan, S. A. Razavi, X. Che, L. Huang, B. Dai, K. Wong, X. Han, K. L. Wang, Room-Temperature Spin-Orbit Torque from Topological Surface States. *Physical Review Letters* **123**, 207205 (2019).

28.   Y. A. Bychkov, É. I. Rashba, Properties of a 2D electron gas with lifted spectral degeneracy. *JETP lett* **39**, 78 (1984).

29.   V. M. Edelstein, Spin polarization of conduction electrons induced by electric current in two-dimensional asymmetric electron systems. *Solid State Communications* **73**, 233-235 (1990).

30.   V. P. Amin, M. D. Stiles, Spin transport at interfaces with spin-orbit coupling: Formalism. *Physical Review B* **94**, 104419 (2016).

31. V. P. Amin, M. D. Stiles, Spin transport at interfaces with spin-orbit coupling: Phenomenology. *Physical Review B* **94**, 104420 (2016).

32. B. A. Bernevig, T. L. Hughes, S.-C. Zhang, Quantum Spin Hall Effect and Topological Phase Transition in HgTe Quantum Wells. *Science* **314**, 1757 (2006).

33. Y. Fan, P. Upadhyaya, X. Kou, M. Lang, S. Takei, Z. Wang, J. Tang, L. He, L.-T. Chang, M. Montazeri, G. Yu, W. Jiang, T. Nie, R. N. Schwartz, Y. Tserkovnyak, K. L. Wang, Magnetization switching through giant spin–orbit torque in a magnetically doped topological insulator heterostructure. *Nature Materials* **13**, 699 (2014).

34. A. R. Mellnik, J. S. Lee, A. Richardella, J. L. Grab, P. J. Mintun, M. H. Fischer, A. Vaezi, A. Manchon, E. A. Kim, N. Samarth, D. C. Ralph, Spin-transfer torque generated by a topological insulator. *Nature* **511**, 449 (2014).

35. H. Wu, Y. Xu, P. Deng, Q. Pan, S. A. Razavi, K. Wong, L. Huang, B. Dai, Q. Shao, G. Yu, X. Han, J.-C. Rojas-Sánchez, S. Mangin, K. L. Wang, Spin-Orbit Torque Switching of a Nearly Compensated Ferrimagnet by Topological Surface States. *Advanced Materials* **0**, 1901681 (2019).

36. S. Mangin, D. Ravelosona, J. A. Katine, M. J. Carey, B. D. Terris, E. E. Fullerton, Current-induced magnetization reversal in nanopillars with perpendicular anisotropy. *Nature Materials* **5**, 210-215 (2006).

37. G. Yu, P. Upadhyaya, Y. Fan, J. G. Alzate, W. Jiang, K. L. Wong, S. Takei, S. A. Bender, L.-T. Chang, Y. Jiang, M. Lang, J. Tang, Y. Wang, Y. Tserkovnyak, P. K. Amiri, K. L. Wang, Switching of perpendicular magnetization by spin–orbit torques in the absence of external magnetic fields. *Nature Nanotechnology* **9**, 548 (2014).

38. L. Liu, O. J. Lee, T. J. Gudmundsen, D. C. Ralph, R. A. Buhrman, Current-Induced Switching of Perpendicularly Magnetized Magnetic Layers Using Spin Torque from the Spin Hall Effect. *Physical Review Letters* **109**, 096602 (2012).

39. L. Liu, C.-F. Pai, Y. Li, H. Tseng, D. Ralph, R. Buhrman, Spin-torque switching with the giant spin Hall effect of tantalum. *Science* **336**, 555-558 (2012).

40. I. M. Miron, K. Garello, G. Gaudin, P.-J. Zermatten, M. V. Costache, S. Auffret, S. Bandiera, B. Rodmacq, A. Schuhl, P. Gambardella, Perpendicular switching of a single ferromagnetic layer induced by in-plane current injection. *Nature* **476**, 189 (2011).

41. K. Garello, I. M. Miron, C. O. Avci, F. Freimuth, Y. Mokrousov, S. Blügel, S. Auffret, O. Boulle, G. Gaudin, P. Gambardella, Symmetry and magnitude of spin–orbit torques in ferromagnetic heterostructures. *Nature Nanotechnology* **8**, 587-593 (2013).

42. K. M. D. Hals, A. Brataas, Phenomenology of current-induced spin-orbit torques. *Physical Review B* **88**, 085423 (2013).

43. P. Upadhyaya, UCLA PhD thesis, Spin-orbitronics: Electrical control of magnets via spin-orbit interaction. (2015).

44. J. Nogués, I. K. Schuller, Exchange bias. *Journal of Magnetism and Magnetic Materials* **192**, 203-232 (1999).

45. S. A. Razavi, D. Wu, G. Yu, Y.-C. Lau, K. L. Wong, W. Zhu, C. He, Z. Zhang, J. M. D. Coey, P. Stamenov, P. Khalili Amiri, K. L. Wang, Joule Heating Effect on Field-Free Magnetization Switching by Spin-Orbit Torque in Exchange-Biased Systems. *Physical Review Applied* **7**, 024023 (2017).

46.   S. Fukami, C. Zhang, S. DuttaGupta, A. Kurenkov, H. Ohno, Magnetization switching by spin–orbit torque in an antiferromagnet–ferromagnet bilayer system. *Nature Materials* **15**, 535 (2016).

47.   A. van den Brink, G. Vermijs, A. Solignac, J. Koo, J. T. Kohlhepp, H. J. M. Swagten, B. Koopmans, Field-free magnetization reversal by spin-Hall effect and exchange bias. *Nature Communications* **7**, 10854 (2016).

48.   Y.-C. Lau, D. Betto, K. Rode, J. M. D. Coey, P. Stamenov, Spin–orbit torque switching without an external field using interlayer exchange coupling. *Nature Nanotechnology* **11**, 758 (2016).

49.   Y.-W. Oh, S.-h. Chris Baek, Y. M. Kim, H. Y. Lee, K.-D. Lee, C.-G. Yang, E.-S. Park, K.-S. Lee, K.-W. Kim, G. Go, J.-R. Jeong, B.-C. Min, H.-W. Lee, K.-J. Lee, B.-G. Park, Field-free switching of perpendicular magnetization through spin–orbit torque in antiferromagnet/ferromagnet/oxide structures. *Nature Nanotechnology* **11**, 878 (2016).

50.   J. Kim, J. Sinha, M. Hayashi, M. Yamanouchi, S. Fukami, T. Suzuki, S. Mitani, H. Ohno, Layer thickness dependence of the current-induced effective field vector in Ta|CoFeB|MgO. *Nature Materials* **12**, 240 (2012).

51.   K. Garello, I. M. Miron, C. O. Avci, F. Freimuth, Y. Mokrousov, S. Blügel, S. Auffret, O. Boulle, G. Gaudin, P. Gambardella, Symmetry and magnitude of spin–orbit torques in ferromagnetic heterostructures. *Nature Nanotechnology* **8**, 587 (2013).

52.   M. Hayashi, J. Kim, M. Yamanouchi, H. Ohno, Quantitative characterization of the spin-orbit torque using harmonic Hall voltage measurements. *Physical Review B* **89**, 144425 (2014).

53. M. Yang, K. Cai, H. Ju, K. W. Edmonds, G. Yang, S. Liu, B. Li, B. Zhang, Y. Sheng, S. Wang, Y. Ji, K. Wanga, Spin-orbit torque in Pt/CoNiCo/Pt symmetric devices. *Scientific Reports* **6**, 20778 (2016).

54. S. Emori, U. Bauer, S. Woo, G. S. D. Beach, Large voltage-induced modification of spin-orbit torques in Pt/Co/GdOx. *Applied Physics Letters* **105**, 222401 (2014).

55. D. Wu, G. Yu, C. T. Chen, S. A. Razavi, Q. Shao, X. Li, B. Zhao, K. L. Wong, C. He, Z. Zhang, P. K. Amiri, K. L. Wang, Spin-orbit torques in perpendicularly magnetized Ir22Mn78/Co20Fe60B20/MgO multilayer. *Applied Physics Letters* **109**, 222401 (2016).

56. G. Yu, P. Upadhyaya, K. L. Wong, W. Jiang, J. G. Alzate, J. Tang, P. K. Amiri, K. L. Wang, Magnetization switching through spin-Hall-effect-induced chiral domain wall propagation. *Physical Review B* **89**, 104421 (2014).

57. J.-C. Rojas-Sánchez, N. Reyren, P. Laczkowski, W. Savero, J.-P. Attané, C. Deranlot, M. Jamet, J.-M. George, L. Vila, H. Jaffrès, Spin Pumping and Inverse Spin Hall Effect in Platinum: The Essential Role of Spin-Memory Loss at Metallic Interfaces. *Physical Review Letters* **112**, 106602 (2014).

58. L. Liu, O. Lee, T. Gudmundsen, D. Ralph, R. Buhrman, Current-induced switching of perpendicularly magnetized magnetic layers using spin torque from the spin Hall effect. *Physical review letters* **109**, 096602 (2012).

59. J. Nogués, I. K. Schuller, Exchange bias. *Journal of Magnetism and Magnetic Materials* **192**, 203 (1999).

60. C. Binek, Training of the exchange-bias effect: A simple analytic approach. *Physical Review B* **70**, 014421 (2004).

61.   M. Ali, C. H. Marrows, M. Al-Jawad, B. J. Hickey, A. Misra, U. Nowak, K. D. Usadel, Antiferromagnetic layer thickness dependence of the IrMn/Co exchange-bias system. *Physical Review B* **68**, 214420 (2003).

62.   A. v. d. Brink, G. Vermijs, A. Solignac, J. Koo, J. T. Kohlhepp, H. J. M. Swagten, B. Koopmans, Field-free magnetization reversal by spin-Hall effect and exchange bias. *Nature Communications* **7**, 10854 (2016).

63.   H. Xi, R. M. White, Theory of the blocking temperature in polycrystalline exchange biased bilayers based on a thermal fluctuation model. *Journal of Applied Physics* **94**, 5850 (2003).

64.   S. Maat, K. Takano, S. S. P. Parkin, E. E. Fullerton, Perpendicular Exchange Bias of Co/Pt Multilayers. *Physical Review Letters* **87**, 087202 (2001).

65.   A. Hochstrat, C. Binek, W. Kleemann, Training of the exchange-bias effect in NiO-Fe heterostructures. *Physical Review B* **66**, 092409 (2002).

66.   K. Zhang, T. Zhao, H. Fujiwara, Training effect of exchange biased iron–oxide/ferromagnet systems. *Journal of Applied Physics* **89**, 6910 (2001).

67.   P. Miltényi, M. Gierlings, J. Keller, B. Beschoten, G. Güntherodt, U. Nowak, K. D. Usadel, Diluted Antiferromagnets in Exchange Bias: Proof of the Domain State Model. *Physical Review Letters* **84**, 4224 (2000).

68.   T. Gredig, I. N. Krivorotov, E. D. Dahlberg, Magnetization reversal in exchange biased Co/CoO probed with anisotropic magnetoresistance. *Journal of Applied Physics* **91**, 7760 (2002).

69. F. Radu, M. Etzkorn, R. Siebrecht, T. Schmitte, K. Westerholt, H. Zabel, Interfacial domain formation during magnetization reversal in exchange-biased CoO/Co bilayers. *Physical Review B* **67**, 134409 (2003).

70. T. Hauet, J. A. Borchers, P. Mangin, Y. Henry, S. Mangin, Training Effect in an Exchange Bias System: The Role of Interfacial Domain Walls. *Physical Review Letters* **96**, 067207 (2006).

71. S. Brems, K. Temst, C. V. Haesendonck, Origin of the Training Effect and Asymmetry of the Magnetization in Polycrystalline Exchange Bias Systems. *Physical Review Letters* **99**, 067201 (2007).

72. S. Yuasa, T. Nagahama, A. Fukushima, Y. Suzuki, K. Ando, Giant room-temperature magnetoresistance in single-crystal Fe/MgO/Fe magnetic tunnel junctions. *Nature Materials* **3**, 868-871 (2004).

73. S. S. P. Parkin, C. Kaiser, A. Panchula, P. M. Rice, B. Hughes, M. Samant, S.-H. Yang, Giant tunnelling magnetoresistance at room temperature with MgO (100) tunnel barriers. *Nature Materials* **3**, 862-867 (2004).

74. D. Wu, G. Yu, C.-T. Chen, S. A. Razavi, Q. Shao, X. Li, B. Zhao, K. L. Wong, C. He, Z. Zhang, P. K. Amiri, K. L. Wang, Spin-orbit torques in perpendicularly magnetized Ir22Mn78/Co20Fe60B20/MgO multilayer. *Applied Physics Letters* **109**, 222401 (2016).

75. W. Zhang, W. Han, S.-H. Yang, Y. Sun, Y. Zhang, B. Yan, S. S. P. Parkin, Giant facet-dependent spin-orbit torque and spin Hall conductivity in the triangular antiferromagnet IrMn<sub>3</sub>. *Science Advances* **2**, e1600759 (2016).

76. K. Garello, C. O. Avci, I. M. Miron, M. Baumgartner, A. Ghosh, S. Auffret, O. Boulle, G. Gaudin, P. Gambardella, Ultrafast magnetization switching by spin-orbit torques. *Applied Physics Letters* **105**, 212402 (2014).

77. R. Ramaswamy, J. M. Lee, K. Cai, H. Yang, Recent advances in spin-orbit torques: Moving towards device applications. *Applied Physics Reviews* **5**, 031107 (2018).

78. D. MacNeill, G. M. Stiehl, M. H. D. Guimaraes, R. A. Buhrman, J. Park, D. C. Ralph, Control of spin–orbit torques through crystal symmetry in WTe2/ferromagnet bilayers. *Nature Physics* **13**, 300-305 (2017).

79. G. Yu, L.-T. Chang, M. Akyol, P. Upadhyaya, C. He, X. Li, K. L. Wong, P. K. Amiri, K. L. Wang, Current-driven perpendicular magnetization switching in Ta/CoFeB/[TaOx or MgO/TaOx] films with lateral structural asymmetry. *Applied Physics Letters* **105**, 102411 (2014).

80. A. Razavi, H. Wu, Q. Shao, C. Fang, B. Dai, K. Wong, X. Han, G. Yu, K. L. Wang, Deterministic Spin–Orbit Torque Switching by a Light-Metal Insertion. *Nano Letters*, (2020).

81. A. Manchon, H. C. Koo, J. Nitta, S. M. Frolov, R. A. Duine, New perspectives for Rashba spin–orbit coupling. *Nature Materials* **14**, 871 (2015).

82. M. Nagano, A. Kodama, T. Shishidou, T. Oguchi, A first-principles study on the Rashba effect in surface systems. *Journal of Physics: Condensed Matter* **21**, 064239 (2009).

83. S. Ikeda, K. Miura, H. Yamamoto, K. Mizunuma, H. D. Gan, M. Endo, S. Kanai, J. Hayakawa, F. Matsukura, H. Ohno, A perpendicular-anisotropy CoFeB–MgO magnetic tunnel junction. *Nature Materials* **9**, 721 (2010).

84. C.-F. Pai, M. Mann, A. J. Tan, G. S. D. Beach, Determination of spin torque efficiencies in heterostructures with perpendicular magnetic anisotropy. *Physical Review B* **93**, 144409 (2016).

85. V. M. P, K. R. Ganesh, P. S. A. Kumar, Spin Hall effect mediated current-induced deterministic switching in all-metallic perpendicularly magnetized Pt/Co/Pt trilayers. *Physical Review B* **96**, 104412 (2017).

86. L. You, O. Lee, D. Bhowmik, D. Labanowski, J. Hong, J. Bokor, S. Salahuddin, Switching of perpendicularly polarized nanomagnets with spin orbit torque without an external magnetic field by engineering a tilted anisotropy. *Proceedings of the National Academy of Sciences* **112**, 10310 (2015).

87. A. Razavi, H. Wu, B. Dai, H. He, D. Wu, K. Wong, G. Yu, K. L. Wang, Spin–orbit torques in structures with asymmetric dusting layers. *Applied Physics Letters* **117**, 182403 (2020).

88. M. Dc, R. Grassi, J.-Y. Chen, M. Jamali, D. Reifsnyder Hickey, D. Zhang, Z. Zhao, H. Li, P. Quarterman, Y. Lv, M. Li, A. Manchon, K. A. Mkhoyan, T. Low, J.-P. Wang, Room-temperature high spin–orbit torque due to quantum confinement in sputtered BixSe(1–x) films. *Nature Materials* **17**, 800-807 (2018).

89. J. Han, A. Richardella, S. A. Siddiqui, J. Finley, N. Samarth, L. Liu, Room-Temperature Spin-Orbit Torque Switching Induced by a Topological Insulator. *Physical Review Letters* **119**, 077702 (2017).

90. N. H. D. Khang, Y. Ueda, P. N. Hai, A conductive topological insulator with large spin Hall effect for ultralow power spin–orbit torque switching. *Nature Materials* **17**, 808-813 (2018).

91. Q. Shao, H. Wu, Q. Pan, P. Zhang, L. Pan, K. Wong, X. Che, K. L. Wang, in *2018 IEEE International Electron Devices Meeting (IEDM)*. (2018), pp. 36.33.31-36.33.34.

92. H. Wu, Y. Xu, P. Deng, Q. Pan, S. A. Razavi, K. Wong, L. Huang, B. Dai, Q. Shao, G. Yu, X. Han, J.-C. Rojas-Sánchez, S. Mangin, K. L. Wang, Spin-Orbit Torque Switching of a Nearly Compensated Ferrimagnet by Topological Surface States. *Advanced Materials* **31**, 1901681 (2019).

93. S. Tacchi, R. E. Troncoso, M. Ahlberg, G. Gubbiotti, M. Madami, J. Åkerman, P. Landeros, Interfacial Dzyaloshinskii-Moriya Interaction in $\mathrm{Pt}/\mathrm{CoFeB}$ Films: Effect of the Heavy-Metal Thickness. *Physical Review Letters* **118**, 147201 (2017).

94. H. T. Nembach, J. M. Shaw, M. Weiler, E. Jué, T. J. Silva, Linear relation between Heisenberg exchange and interfacial Dzyaloshinskii–Moriya interaction in metal films. *Nature Physics* **11**, 825-829 (2015).

95. K. Di, V. L. Zhang, H. S. Lim, S. C. Ng, M. H. Kuok, J. Yu, J. Yoon, X. Qiu, H. Yang, Direct Observation of the Dzyaloshinskii-Moriya Interaction in a Pt/Co/Ni Film. *Physical Review Letters* **114**, 047201 (2015).

96. J. Cho, N.-H. Kim, S. Lee, J.-S. Kim, R. Lavrijsen, A. Solignac, Y. Yin, D.-S. Han, N. J. J. van Hoof, H. J. M. Swagten, B. Koopmans, C.-Y. You, Thickness dependence of the interfacial Dzyaloshinskii–Moriya interaction in inversion symmetry broken systems. *Nature Communications* **6**, 7635 (2015).

97. X. Ma, G. Yu, S. A. Razavi, S. S. Sasaki, X. Li, K. Hao, S. H. Tolbert, K. L. Wang, X. Li, Dzyaloshinskii-Moriya Interaction across an Antiferromagnet-Ferromagnet Interface. *Physical Review Letters* **119**, 027202 (2017).

98. X. Ma, G. Yu, S. A. Razavi, L. Chang, L. Deng, Z. Chu, C. He, K. L. Wang, X. Li, Correlation between the Dzyaloshinskii-Moriya interaction and spin-mixing conductance at an antiferromagnet/ferromagnet interface. *Physical Review B* **98**, 104428 (2018).

99. M. Johnson, P. Bloemen, F. Den Broeder, J. De Vries, Magnetic anisotropy in metallic multilayers. *Reports on Progress in Physics* **59**, 1409 (1996).

100. J.-g. Hu, G.-j. Jin, Y.-q. Ma, Thickness dependence of exchange bias and coercivity in a ferromagnetic layer coupled with an antiferromagnetic layer. *Journal of Applied Physics* **94**, 2529-2533 (2003).

101. H. Yang, A. Thiaville, S. Rohart, A. Fert, M. Chshiev, Anatomy of Dzyaloshinskii-Moriya Interaction at Co/Pt Interfaces. *Physical Review Letters* **115**, 267210 (2015).

102. C. He, S. A. Razavi, G. Yu, X. Ma, H. Wu, Q. Shao, K. L. Wong, S. Shen, Y. Zhao, Y. Pei, Q. Chen, X. Li, S. Wang, K. L. Wang, Study of the perpendicular magnetic anisotropy, spin–orbit torque, and Dzyaloshinskii–Moriya interaction in the heavy metal/CoFeB bilayers with Ir22Mn78 insertion. *Applied Physics Letters* **116**, 242407 (2020).

103. X. Ma, G. Yu, C. Tang, X. Li, C. He, J. Shi, K. L. Wang, X. Li, Interfacial Dzyaloshinskii-Moriya Interaction: Effect of $5d$ Band Filling and Correlation with Spin Mixing Conductance. *Physical Review Letters* **120**, 157204 (2018).

104. A. Fert, V. Cros, J. Sampaio, Skyrmions on the track. *Nature Nanotechnology* **8**, 152 (2013).

105. D. Bhattacharya, J. Atulasimha, Skyrmion-Mediated Voltage-Controlled Switching of Ferromagnets for Reliable and Energy-Efficient Two-Terminal Memory. *ACS Applied Materials & Interfaces* **10**, 17455-17462 (2018).

106. S. Mühlbauer, B. Binz, F. Jonietz, C. Pfleiderer, A. Rosch, A. Neubauer, R. Georgii, P. Böni, Skyrmion Lattice in a Chiral Magnet. *Science* **323**, 915 (2009).

107. X. Z. Yu, Y. Onose, N. Kanazawa, J. H. Park, J. H. Han, Y. Matsui, N. Nagaosa, Y. Tokura, Real-space observation of a two-dimensional skyrmion crystal. *Nature* **465**, 901-904 (2010).

108. X. Z. Yu, N. Kanazawa, Y. Onose, K. Kimoto, W. Z. Zhang, S. Ishiwata, Y. Matsui, Y. Tokura, Near room-temperature formation of a skyrmion crystal in thin-films of the helimagnet FeGe. *Nature Materials* **10**, 106-109 (2011).

109. S. Heinze, K. von Bergmann, M. Menzel, J. Brede, A. Kubetzka, R. Wiesendanger, G. Bihlmayer, S. Blügel, Spontaneous atomic-scale magnetic skyrmion lattice in two dimensions. *Nature Physics* **7**, 713-718 (2011).

110. N. Romming, C. Hanneken, M. Menzel, J. E. Bickel, B. Wolter, K. von Bergmann, A. Kubetzka, R. Wiesendanger, Writing and Deleting Single Magnetic Skyrmions. *Science* **341**, 636 (2013).

111. W. Jiang, P. Upadhyaya, W. Zhang, G. Yu, M. B. Jungfleisch, F. Y. Fradin, J. E. Pearson, Y. Tserkovnyak, K. L. Wang, O. Heinonen, S. G. E. te Velthuis, A. Hoffmann, Blowing magnetic skyrmion bubbles. *Science* **349**, 283-286 (2015).

112. S. Woo, K. Litzius, B. Krüger, M.-Y. Im, L. Caretta, K. Richter, M. Mann, A. Krone, R. M. Reeve, M. Weigand, P. Agrawal, I. Lemesh, M.-A. Mawass, P. Fischer, M. Kläui, G. S. D. Beach, Observation of room-temperature magnetic skyrmions and their current-driven dynamics in ultrathin metallic ferromagnets. *Nature Materials* **15**, 501-506 (2016).

113. O. Boulle, J. Vogel, H. Yang, S. Pizzini, D. de Souza Chaves, A. Locatelli, T. O. Menteş, A. Sala, L. D. Buda-Prejbeanu, O. Klein, M. Belmeguenai, Y. Roussigné, A. Stashkevich, S. M. Chérif, L. Aballe, M. Foerster, M. Chshiev, S. Auffret, I. M. Miron, G. Gaudin, Room-temperature chiral magnetic skyrmions in ultrathin magnetic nanostructures. *Nature Nanotechnology* **11**, 449-454 (2016).

114. G. Yu, A. Jenkins, X. Ma, S. A. Razavi, C. He, G. Yin, Q. Shao, Q. l. He, H. Wu, W. Li, W. Jiang, X. Han, X. Li, A. C. Bleszynski Jayich, P. K. Amiri, K. L. Wang, Room-Temperature Skyrmions in an Antiferromagnet-Based Heterostructure. *Nano Letters* **18**, 980-986 (2018).

115. S. Rohart, A. Thiaville, Skyrmion confinement in ultrathin film nanostructures in the presence of Dzyaloshinskii-Moriya interaction. *Physical Review B* **88**, 184422 (2013).

116. D. Bhattacharya, S. A. Razavi, H. Wu, B. Dai, K. L. Wang, J. Atulasimha, Creation and annihilation of non-volatile fixed magnetic skyrmions using voltage control of magnetic anisotropy. *Nature Electronics*, (2020).

117. X. Li, UCLA, (2018).

118. W. Jiang, X. Zhang, G. Yu, W. Zhang, X. Wang, M. Benjamin Jungfleisch, John E. Pearson, X. Cheng, O. Heinonen, K. L. Wang, Y. Zhou, A. Hoffmann, Suzanne G. E. te Velthuis, Direct observation of the skyrmion Hall effect. *Nature Physics* **13**, 162 (2016).

119. T. Srivastava, M. Schott, R. Juge, V. Křižáková, M. Belmeguenai, Y. Roussigné, A. Bernand-Mantel, L. Ranno, S. Pizzini, S.-M. Chérif, A. Stashkevich, S. Auffret, O. Boulle, G. Gaudin, M. Chshiev, C. Baraduc, H. Béa, Large-Voltage Tuning of Dzyaloshinskii–Moriya Interactions: A Route toward Dynamic Control of Skyrmion Chirality. *Nano Letters* **18**, 4871-4877 (2018).

120. D. Bhattacharya, S. A. Razavi, H. Wu, B. Dai, K. L. Wang, J. Atulasimha, Experimental creation and annihilation of nonvolatile magnetic skyrmions using voltage control of magnetic anisotropy without an external magnetic field. *arXiv* **1904.00701**, (2019).

121. K. Cai, M. Yang, H. Ju, S. Wang, Y. Ji, B. Li, K. W. Edmonds, Y. Sheng, B. Zhang, N. Zhang, S. Liu, H. Zheng, K. Wang, Electric field control of deterministic current-induced magnetization switching in a hybrid ferromagnetic/ferroelectric structure. *Nature Materials* **16**, 712 (2017).

122. I. Dzyaloshinsky, A thermodynamic theory of "weak" ferromagnetism of antiferromagnetics. *Journal of Physics and Chemistry of Solids* **4**, 241-255 (1958).

123. T. Moriya, Anisotropic Superexchange Interaction and Weak Ferromagnetism. *Physical Review* **120**, 91-98 (1960).

124. A. Fert, P. M. Levy, Role of Anisotropic Exchange Interactions in Determining the Properties of Spin-Glasses. *Physical Review Letters* **44**, 1538-1541 (1980).

125. G. Chen, T. Ma, A. T. N'Diaye, H. Kwon, C. Won, Y. Wu, A. K. Schmid, Tailoring the chirality of magnetic domain walls by interface engineering. *Nature Communications* **4**, 2671 (2013).

126. N. Nagaosa, Y. Tokura, Topological properties and dynamics of magnetic skyrmions. *Nature nanotechnology* **8**, 899-911 (2013).

127. K.-W. Kim, K.-W. Moon, N. Kerber, J. Nothhelfer, K. Everschor-Sitte, Asymmetric skyrmion Hall effect in systems with a hybrid Dzyaloshinskii-Moriya interaction. *Physical Review B* **97**, 224427 (2018).

128. C.-G. Duan, J. P. Velev, R. F. Sabirianov, Z. Zhu, J. Chu, S. S. Jaswal, E. Y. Tsymbal, Surface Magnetoelectric Effect in Ferromagnetic Metal Films. *Physical Review Letters* **101**, 137201 (2008).

129. J. Alzate, Voltage-Controlled Magnetic Dynamics in Nanoscale Magnetic Tunnel Junctions. *UCLA PhD Thesis*, (2014).

130. X. Li, A. Lee, S. A. Razavi, H. Wu, K. L. Wang, Voltage-controlled magnetoelectric memory and logic devices. *MRS Bulletin* **43**, 970-977 (2018).

131. S. E. Barnes, J. i. Ieda, S. Maekawa, Rashba spin-orbit anisotropy and the electric field control of magnetism. *Scientific reports* **4**, 1-5 (2014).

132. Y. Shiota, T. Nozaki, F. Bonell, S. Murakami, T. Shinjo, Y. Suzuki, Induction of coherent magnetization switching in a few atomic layers of FeCo using voltage pulses. *Nature Materials* **11**, 39-43 (2012).

133. T. Maruyama, Y. Shiota, T. Nozaki, K. Ohta, N. Toda, M. Mizuguchi, A. A. Tulapurkar, T. Shinjo, M. Shiraishi, S. Mizukami, Y. Ando, Y. Suzuki, Large voltage-induced magnetic anisotropy change in a few atomic layers of iron. *Nature Nanotechnology* **4**, 158 (2009).

134. P. K. Amiri, K. L. Wang, Voltage-Controlled Magnetic Anisotropy in Spintronic Devices. *SPIN* **02**, 1240002 (2012).